Institut de Física d'Altes Energies · BIST Barcelona Institute of Science and Technology · UAB Universitat Autònoma de Barcelona

Doctoral Thesis

Archival search of very high energy transient sources with the MAGIC telescopes

Elia do Souto Espiñeira

Departament de Física
Universitat Autònoma de Barcelona
Programa de doctorat en Física

Director:
Dr. Javier
Rico Castro

Tutor:
Dr. Manuel
Delfino Reznicek

A thesis submitted for the degree of
Philosophiæ Doctor

March 2024

Abstract

Transient sources are astronomical objects or events that evolve in short timescales (from milliseconds to days). The transient sky in Very High Energy (VHE) gamma-rays offers a window into the most energetic and dynamic processes in the Universe. This thesis introduces a novel algorithm for the archival search of transient VHE sources with the Major Atmospheric Gamma-ray Imaging Cherenkov (MAGIC) telescopes, a system of two Imaging Atmospheric Cherenkov Telescopes (IACTs).

After 20 years in operation, the MAGIC telescopes have accumulated vast amounts of observational data, but the day-to-day observation of transients depends on alerts from other experiments. This new method aims to leverage archival data for the search of transient events. The method is designed as an unbiased direct search for transients with no a-priori assumptions on their temporal or spectral profiles, with its main parameter being the timescale of the target source. We applied the search in four different timescales, $2\,\mathrm{s}$, $10\,\mathrm{s}$, $100\,\mathrm{s}$ and $1000\,\mathrm{s}$, and focused the analysis of the results on the case of Primordial Black Hole (PBH) evaporation.

PBHs are hypothesized to have formed in the early Universe due to density fluctuations and have a wide range of possible initial masses. PBHs with an initial mass around $10^{11} - 10^{12}\,\mathrm{kg}$ are an attractive target for IACTs, since they would be reaching the end of their lifetimes today with an intense and fast explosion of VHE particles due to Hawking radiation. A detection of VHE emission from PBHs would, in addition to confirming their existence, constitute the first proof for Hawking radiation and have a wide impact on cosmological models. Focused on the detection of PBH evaporation, this work presents an analysis of one year of observational archival data from MAGIC.

While several candidate signals emerged in our search, none had enough

statistical significance to warrant a detection claim for PBH evaporation or other transient event. Nevertheless, the non-detections yielded upper limits on the evaporation rate density of PBHs near Earth in previously unexamined parameter space. These results were used to discuss the different approaches to observing PBHs used by MAGIC and other gamma-ray experiments, and derive upper limits on the PBH density ratio in the early Universe.

Additionally, we obtained generic upper limits on the number of transient flares per year as a function of their integrated flux, for different spectral assumptions.

The development of a background estimation model as part of this thesis improves our capability to analyse vast datasets for the search of transient events. The algorithms and methodologies developed herein can be used in future searches focused on different transient events, or applied to a larger dataset. This thesis contributes to setting new upper limits in the field but also advances the analytical tools available for future transient searches in the VHE domain.

Contents

Used Terms

a.s.l above sea level.

ADC Analogue Digital Converters.

AGN Active Galactic Nuclei.

BH Black Hole.

CCD Charge-Coupled Device.

CDF Cumulative Distribution Function.

CH Counting House.

CL Confidence Level.

CMB Cosmic Microwave Background.

CoG Centre of Gravity.

CR Cosmic Ray.

DAQ Data AcQuisition system.

DC Direct Current.

Dec Declination.

DM Dark Matter.

DRS4 Domino Ring Sampler chip version 4.

EAS Extensive Air Shower.

EM ElectroMagnetic.

FoV Field of View.

FRB Fast Radio Burst.

FWER FamilyWise Error Rate.

GRB Gamma-Ray Burst.

HE High-Energy.

IACT Imaging Atmospheric Cherenkov Telescope.

LED Light Emitting Diode.

LIDAR Light Detection And Ranging.

LUT Look-Up Table.

M-I MAGIC-I.

M-II MAGIC-II.

MAGIC Major Atmospheric Gamma-ray Imaging Cherenkov.

MARS MAGIC Analysis and Reconstruction Software.

MC Monte Carlo.

MJD Modified Julian Date.

NN Next Neighbour.

NSB Night Sky Background.

PBH Primordial Black Hole.

PDF Probability Density Function.

PMT PhotoMultiplier Tube.

PSF Point Spread Function.

R.A. Right Ascension.

RF Random Forest.

RMS Root Mean Square.

RoI Region of Interest.

SEM Standard Evaporation Model.

VHE Very-High-Energy.

Zd Zenith distance.

Chapter 1

Gamma-ray astronomy

During the last few decades gamma-ray astronomy has solidified itself as a powerful discipline within modern astrophysics and particle physics. Being the branch of astronomy that studies the most energetic photons in the Universe, it provides an insight into the non-thermal processes of the cosmos, such as acceleration, propagation and radiation of relativistic particles. Gamma-rays are also a very useful probe for fundamental physics beyond the Standard Model.

The birth of gamma-ray astronomy is strongly tied to Cosmic Ray (CR) astronomy and the monumental discoveries achieved in particle physics during the 20th century. The cosmic-ray story began in the early 1900s with the discovery that electroscopes would discharge even in the absence of natural radioactivity. It was Rutherford who showed that most of the ionisation measured in the electroscopes was due to the natural radioactivity present in rocks (Rutherford 1913). However, the remaining ionisation detected inside the lead shield remained unaccounted for, which stimulated further research.

The origin of this ionising radiation would be discovered in the experiments performed in 1912 and 1913 by Victor Hess, where, onboard of a balloon, he measured increasing levels of ionisation with altitude. Those findings confirmed that the source of this ionising radiation was extraterrestrial in nature (Hess 1912). Furthermore, their data indicated that the ionising radiation was more penetrating than the gamma-rays observed in radioactive decays. It was thus assumed that these *cosmic rays* (term coined by R. Millikan) were gamma-rays with greater penetrating power those from natural decays.

In 1928, the study of CRs became easier with the invention of the Geiger-Muller detector. Using various counters, Bothe and Kohlhorster designed the coincidence technique[1] and found strong evidence that the cosmic radiation was composed of charged particles (Bothe et al. 1929), not highly penetrating photons. As of today, we know that CRs are mostly ($99\,\%$) atomic nuclei and about $1\,\%$ are electrons. Of the nuclei, about $80\,\%$ are protons, $15\,\%$ are alpha particles, and the remaining $5\,\%$ are the nuclei of heavier elements (Thoudam et al. 2016).

Bothe and Kohlhorster found that the flux of these particles could explain the observed intensity of cosmic rays at sea-level, with particle energies on the order of $10^9\,\mathrm{eV}$ to $10^{10}\,\mathrm{eV}$. The observation of showers of CR particles in cloud chamber experiments propelled the investigation of Extensive Air Shower (EAS), first discovered by Rossi in 1934 (Rossi 1934). Their size was established by Auger in 1939 (Auger et al. 1939), when he and his colleagues used separated detectors to see that the air showers could extend over areas greater than $100\,\mathrm{m}$. This provided direct evidence for the acceleration of charged particles to extremely high energies in extraterrestrial sources, since a shower of that size would need to be initiated by a particle with energy exceeding $10^{15}\,\mathrm{eV}$.

From the 1930s to the 1950s, the study of CRs lead to the discovery of the positron (Dirac 1928, Anderson 1932), the muon (Anderson et al. 1936), the pion, the charged and the neutral kaon and lambda particles. In 1953, the advancement of accelerator technology allowed for lab-created energies comparable to CRs. This development shifted the focus of high-energy physics from CRs to accelerator experiments, where energies could be precisely controlled and aimed onto specific targets. As a result, the interest in CRs was redirected to the study of their origin and their propagation in astrophysical environments.

The charged nature of CRs makes them susceptible to being deviated by magnetic fields in their path. Consequently, their origin can not be studied by their observations alone. However, the interaction of CRs with the ambient gas of the source, low frequency radiation and magnetic fields produce very high energy gamma-rays that can be traced back to their origin. This was originally the selling point of the study of gamma-rays, the discovery of the sources of CRs responsible for the tremendous energies observed.

[1] To reduce spurious counts due to contamination within the counter, two counters are placed one above the other. Simultaneous counts indicate that a charged particle of sufficient penetrating power has passed through the two.

Nowadays, the study of gamma-ray astronomy has expanded beyond that and has become a discipline in its own right. As the most energetic photons, gamma-rays provide a unique window into non-thermal relativistic processes and allow us to investigate astrophysical sources that exhibit extreme conditions and particle acceleration mechanisms. Apart from aiding in the completion of knowledge in the multi-wavelength study of sources, gamma-ray observation can provide insights into cosmology and fundamental physics.

Since the first detection of a Gamma-Ray Burst (GRB) by the Vela satellites in 1967 (Klebesadel et al. 1973), a total of 272 sources have been detected by gamma-ray observation experiments (see fig. 1.1). This combined ef-

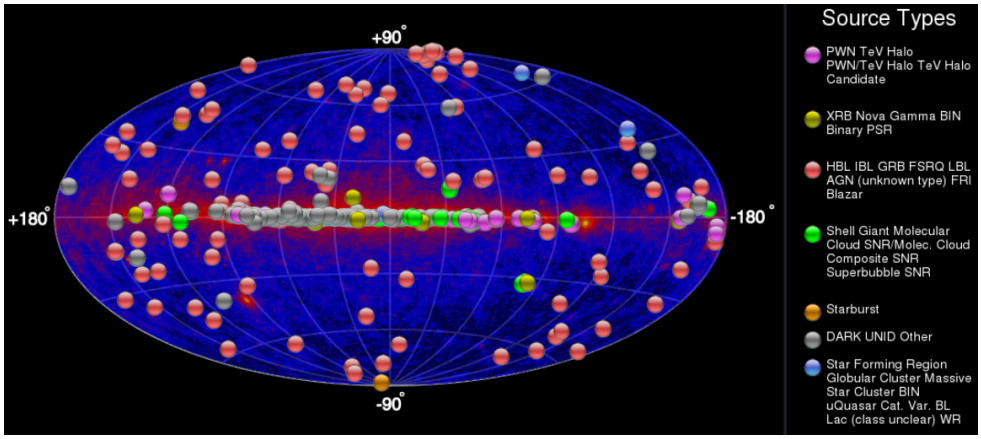

Figure 1.1: All gamma-ray sources are shown as coloured dots on a skymap. The background of the skymap displays the gamma-ray flux measured by the LAT detector onboard the Fermi satellite, with low to high flux represented by a colour gradient from blue to red. The different types of sources are indicated in the legend. Image from TeVCat (Wakely et al. 2008).

fort is carried out by three main types of detectors: in-orbit satellites, which can directly detect gamma-rays above the Earth's atmosphere; Imaging Atmospheric Cherenkov Telescopes (IACTs), ground-based detectors which detect Cherenkov radiation from EAS; and Water Cherenkov Arrays, ground-based detectors which observe the Cherenkov radiation generated in water by high energy particles. Due to the enormous energy range and the different techniques for detection, gamma-ray astronomy is divided in energy bands: "low energy" (LE, below 30 MeV), "high energy" (HE, 30 MeV to 50 GeV), "very high energy" (VHE, 30 GeV to 30 TeV), "ultra high energy" (UHE, 30 TeV to 3×10^4 TeV) and "extremely high energy" (EHE, above 3×10^4 TeV). The work showed in this thesis focuses on the VHE band and the MAGIC IACTs.

1.1 Transient Sources

The field of VHE astrophysics has been historically driven by the study of transient sources. Transient sources are astrophysical phenomena that exhibit sudden and significant changes in their emission properties over timescales ranging from milliseconds to years. Their observation can shed light on subjects such as fundamental physics, particle acceleration mechanisms, energy dissipation processes, and the formation and evolution of celestial objects.

Transient sources cover a wide range of astrophysical phenomena, including GRBs, Fast Radio Bursts (FRBs), supernovae, Active Galactic Nuclei (AGN), cataclysmic variables, tidal disruption events and the not yet detected Primordial Black Hole (PBH) evaporation bursts. Each of these sources is distinct and their properties and mechanisms driving their transient behaviour are very varied, which means that their study can provide valuable information about many different underlying physical processes and environments. However, their detection and study poses significant challenges due to their ephemeral nature and the limited availability of observational data, specially in the case of shorter events.

Nowadays, a network of multi-messenger experiments (Ayala Solares et al. 2020), with rapid detection methods and advanced data analysis techniques is in place to maximize the detection and understanding of these sources. IACTs, as in the case of the MAGIC telescopes, rely on the alerts of detection of such sources by other experiments or observatories, usually in different wavelengths or messengers. This can cause a transient event to be missed if there is lag in the communication between experiments or if the event is very short. Furthermore, the attenuation of gamma-rays due to extragalactic background light can result in the non-detection of a source even when an alert was followed fast enough, leading to the loss of hours of observation.

The main goal of the work detailed in this thesis is the search for gamma-ray signals from transient sources in IACT data. A new software package has been designed specifically for the analysis of archival data from the MAGIC telescopes, but the shared observation strategies in all IACTs make it susceptible to porting to other experiments. The flexibility of the new analysis tool makes it useful for the search of a variety of transient sources. In this thesis we have focused our analysis in the search of signals from evaporating PBHs.

1.1.1 Primordial Black Holes

The existence of Black Holes (BHs) formed in the early Universe (primordial) due to density fluctuations was first theorised by Zeldovich and Novikov in 1966 (Zel'dovich et al. 1966) and, independently, by Hawking in 1971 (Hawking 1971). Since then, PBHs have been a source of intense interest despite the fact that there is still no evidence for them.

Following the Big Bang, the Universe existed in a highly compressed state. This elevated density provided opportunities for various scenarios and mechanisms leading to the formation of PBHs (Carr et al. 2020). Regardless of the specific formation mechanism, each scenario establishes a link between the mass of the PBH and the horizon mass at the time of its formation (Hawking 1971),

$$M \approx \frac{c^3 t}{G} \approx 10^{12} \left(\frac{t}{10^{-23}\mathrm{s}} \right) \mathrm{kg}\,, \tag{1.1}$$

where t is the time after the Big Bang, c is the speed of light and G is the gravitational constant. This results in an enormous possible mass range, spanning from the Planck mass of $10^{-8}\,\mathrm{kg}$ of those BHs formed at the Planck time $10^{-43}\,\mathrm{s}$ to $10^5 \mathrm{M}_\odot$, the lower bound of supermassive black holes for those formed $1\,\mathrm{s}$ after the Big Bang.

Due to their powerful gravitational fields, BHs were historically believed to be incapable of emitting radiation. The idea that PBHs might be exceptionally small prompted an exploration into the quantum characteristics of BHs. This exploration, pioneered by Hawking (Hawking 1974), fundamentally altered our perspective, revealing that BHs indeed radiate particles with spin s at a rate of

$$\frac{d^2 N}{dE dt} = \frac{\Gamma / 2\pi\hbar}{e^x - (-1)^{2s}} n_{\mathrm{dof}}\,, \tag{1.2}$$

with $\hbar$ the reduced Planck constant, n_{dof} the degrees of freedom of the emitted particle and Γ the absorption coefficient describing the fraction of particles absorbed by the BH. For a nonrotating, uncharged BH (Hawking 1975), the dimensionless value x is defined by

$$x \equiv \frac{8\pi G M_{\mathrm{BH}} E}{\hbar c^3} = \frac{E}{k T_{BH}}\,, \tag{1.3}$$

where k is the Boltzmann constant, E is the energy of the radiated particle, M_{BH}

is the mass of the BH and $T_{\rm BH}$ is the temperature of the BH,

$$kT_{\rm BH} = 1.058 \left(\frac{10^{10}{\rm kg}}{M_{\rm BH}}\right) \ {\rm GeV}\,. \tag{1.4}$$

The absorption coefficient Γ for an emitted particle of rest mass m at $E \gg mc^2$ has the form (Ukwatta et al. 2016)

$$\Gamma(M_{\rm BH}, E, s) = 27 \left(\frac{x}{8\pi}\right)^2 \gamma_s(x)\,, \tag{1.5}$$

such that for large x, the incomplete gamma function is $\gamma_s(x) \to 1$.

The radiation of particles cause the BH to lose mass with time, which can be written as function of the energy and temporal spectra of the emitted particles (Page 1976),

$$\frac{dM_{BH}}{dt} = -\frac{1}{c^2}\sum_i \int_0^\infty dE \frac{d^2N_i}{dEdt} E \equiv -\frac{\alpha(M_{\rm BH})}{M_{\rm BH}^2}\,, \tag{1.6}$$

summing over all the i fundamental particle species. The function $\alpha(M_{\rm BH})$ accounts for the degrees of freedom of each emitted particle that contributes to energy loss.

As the BH radiates particles and its temperature rises, α increases smoothly at the rest-mass threshold for each new massive particle available. In fig. 1.2, α is shown for the confirmed Standard Model particles, with each line containing the sum of the asymptotic contributions of each degree of freedom available.

Near the end of the lifetime of the PBH, its temperature times the Boltzman constant surpasses the rest masses of all recognized fundamental particles, and α converges to an asymptotic value, $\alpha_{\rm SM} = 8 \times 10^{17} {\rm kg}^3 {\rm s}^{-1}$. This is true for BHs with $kT_{\rm BH} \geq 50\,{\rm GeV}$ (Ukwatta et al. 2016). Working in this regime, if we integrate eq. (1.6) from time $t = \tau$ until $t = 0$, we find that the time it takes for the BH to lose all its mass is

$$\tau = \frac{M_{\rm PBH}^3}{3\alpha_{\rm SM}}\,. \tag{1.7}$$

This *remaining lifetime* τ allows us to calculate what PBHs would be evaporating

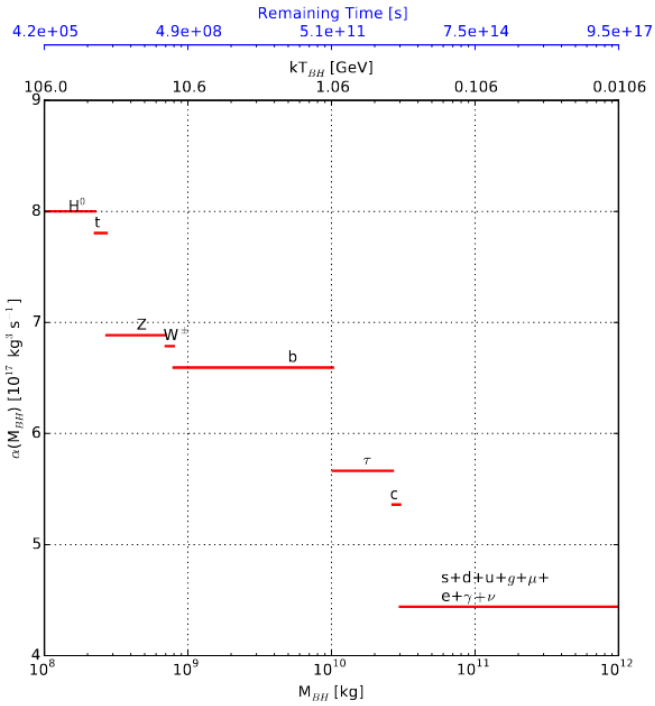

Figure 1.2: The function $\alpha(M_{\mathrm{BH}})$ for the Standard Model particles. The mass, temperature and remaining lifetime of the BH are used as the different horizontal axis. Image from Ukwatta et al. (2016).

at present time.

Assuming a density parameter $\Omega_m = 0.06$ and that the PBHs take a negligible time to form compared to the age of the Universe, PBHs with initial masses of $\sim 5 \times 10^{14}\,\mathrm{g}$ (MacGibbon 1991) should have evaporated during the time of the observations used in this project (years 2013 and 2014). Combining eq. (1.4) and eq. (1.7) we have the relation between remaining lifetime and BH temperature,

$$\tau = 4.8 \times 10^{11} \left(\frac{kT_{\mathrm{BH}}}{\mathrm{GeV}} \right)^{-3} \mathrm{s}\,. \tag{1.8}$$

The relations listed above show that the emission rate of the PBH accelerates with M_{BH}^{-2}, leading to an enormous release of fundamental particles when the BH completes its evaporation.

For the search of evaporation signals with MAGIC and other IACTs, we are interested in the total photon emission rate from the PBH above $50\,\mathrm{GeV}$.

Directly emitted gamma-rays constitute an important component for the photon spectrum of the PBH, peaking at a few times kT_{BH}, and are crucial at the highest photon energies.

In the Standard Evaporation Model (SEM) (MacGibbon et al. 1990, MacGibbon 1991 and Halzen et al. 1991), asymptotically free quarks, gluons and gauge bosons are emitted. Particularly, quarks and gluons undergo fragmentation and hadronization to intermediate states that dominate the photon spectrum at energies below T_{BH}. Photons from the decays of the gauge bosons and other Hawking-radiated fundamental particles, such as tau leptons, provide a small contribution compared to the fragmentation component, and are usually not included in the gamma-ray spectrum used for the search of PBHs.

1.1.1.1 Gamma-ray emission from a PBH burst

In this work, we followed the most recent theoretical analysis and parametrizations for the instantaneous PBH photon spectrum (Ukwatta et al. 2016) to obtain the number of gamma-rays that could be detected by the MAGIC telescopes if a PBH were to evaporate in the local ($\mathcal{O}(\mathrm{pc})$) vicinity of the Earth.

The spectrum used comprises the contributions from the photons directly emitted through Hawking radiation and those arising from the decay, fragmentation, and hadronization of other species initially Hawking-radiated. It can be thus expressed as a sum of the fragmentation contribution and the direct contribution,

$$\frac{d^2N}{dEdt} = \left(\frac{d^2N}{dEdt}\right)_{\mathrm{direct}} + \left(\frac{d^2N}{dEdt}\right)_{\mathrm{frag.}} . \tag{1.9}$$

Assuming that the total fragmentation can be approximated by the pion production, the gamma-ray contribution at energies $E \gtrsim 1\ \mathrm{GeV}$ can be derived as a function of x from eq. (1.3). The fragmentation contribution is

$$\begin{aligned}\left(\frac{d^2N}{dEdt}\right)_{\mathrm{frag.}} &= Ax^{-3/2}[1-\Theta_S(x-0.3)] \\ &\quad + B\frac{e^{-x}}{x(x+1)}\Theta_S(x-0.3)\,,\end{aligned} \tag{1.10}$$

where

$$A = 6.339 \times 10^{23}\mathrm{GeV}^{-1}\mathrm{s}^{-1}\,, \quad B = 1.1367 \times 10^{24}\mathrm{GeV}^{-1}\mathrm{s}^{-1} \tag{1.11}$$

and

$$\Theta_S(u) = 0.5(1 + \tanh(10u))\,. \tag{1.12}$$

The photons that are directly radiated from the PBH follow an instantaneous energy spectrum that can be parametrized as

$$\left(\frac{d^2N}{dEdt}\right)_{\mathrm{direct}} = \frac{1.13 \times 10^{19}\mathrm{GeV}^{-1}\mathrm{s}^{-1}}{\exp(x) - 1} F(x)\,, \tag{1.13}$$

where

$$F(x) = 1.0 \quad \text{for } x \leq 2 \tag{1.14}$$

and

$$\begin{aligned} F(x) = \exp\{&[-0.0962 - 1.982(\ln x - 1.908)] \\ &\times [1 + \tanh(20(\ln x - 1.908))]\} \quad \text{for } x > 2\,. \end{aligned} \tag{1.15}$$

Using these equations, we can calculate the photon energy spectrum over the remaining lifetime of a PBH for different initial masses or temperatures as

$$\frac{dN}{dE}(\tau) = \int_0^\tau dt \frac{d^2N}{dEdt}\,, \tag{1.16}$$

which is shown in the top plot of fig. 1.3 for $\tau = 2\,\mathrm{s}$, $10\,\mathrm{s}$, $100\,\mathrm{s}$ and $1000\,\mathrm{s}$.

We can also calculate the theoretical emission light curve of a PBH in the last few seconds before evaporation integrating over the energy range relevant to the MAGIC telescopes (see fig. 1.4). The shape of this light curve is useful in the scenario of a maximum likelihood analysis of the data and to calculate the dead-time fraction of the detector, as we will see in chapter 7, where we calculate the upper limits on the local PBH evaporation burst density.

The expressions shown in eq. (1.10) and eq. (1.13) are not, however, the only parametrizations of the PBH photon emission spectrum that exist in the literature. Another popular way of parametrising the time-integrated photon spectrum of PBHs is done by Petkov et al. (2008). In this case the spectrum is

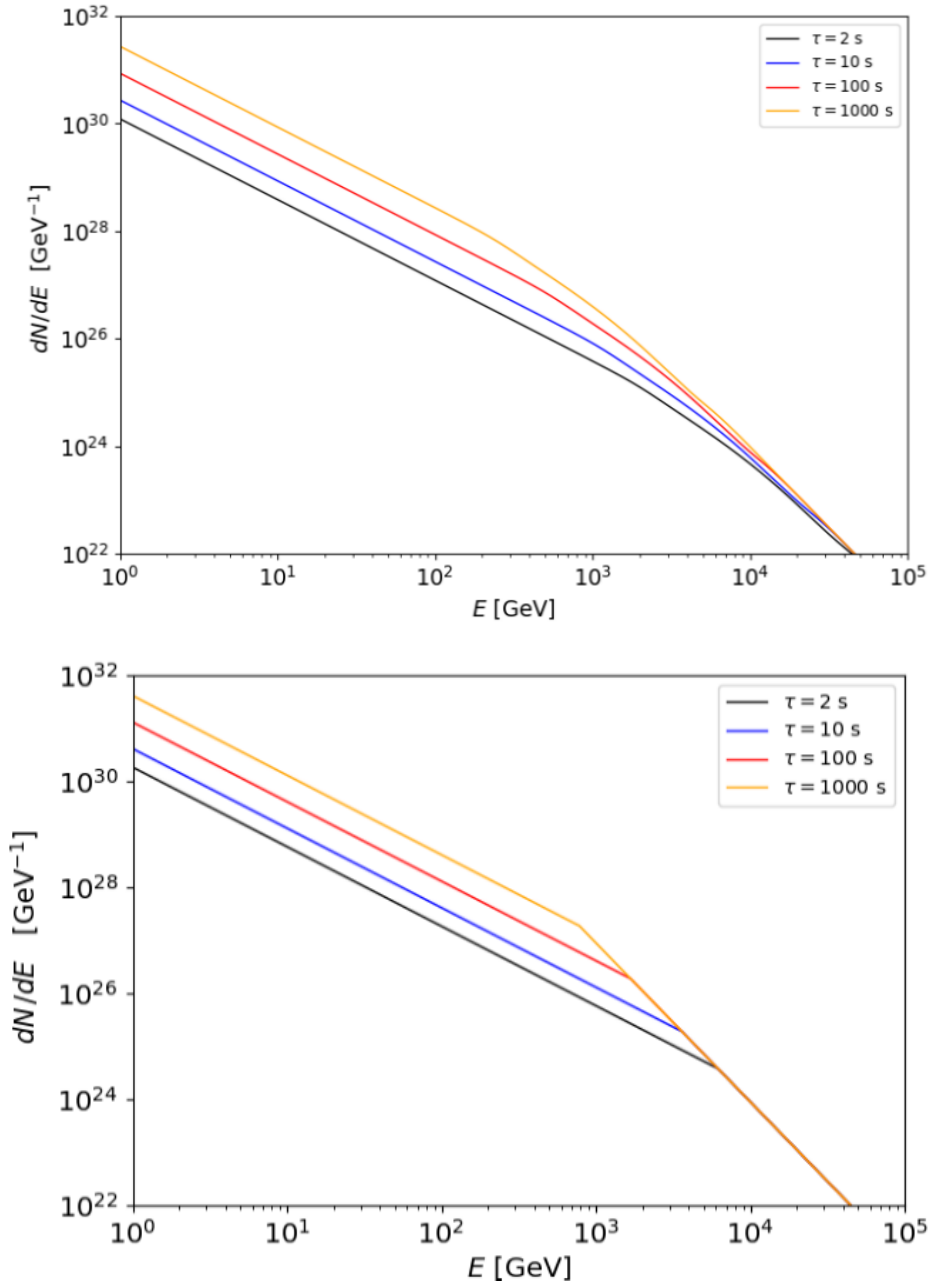

Figure 1.3: Time-integrated photon spectra of the final PBH evaporation, integrated from $t = \tau$ to $t = 0\,\mathrm{s}$ for different remaining lifetime intervals and using two different parametrizations. In the top figure, the parametrization used for the instantaneous photon spectrum was that of Ukwatta et al. (2016). In the bottom figure, the integrated spectrum is directly given by Petkov et al. (2008).

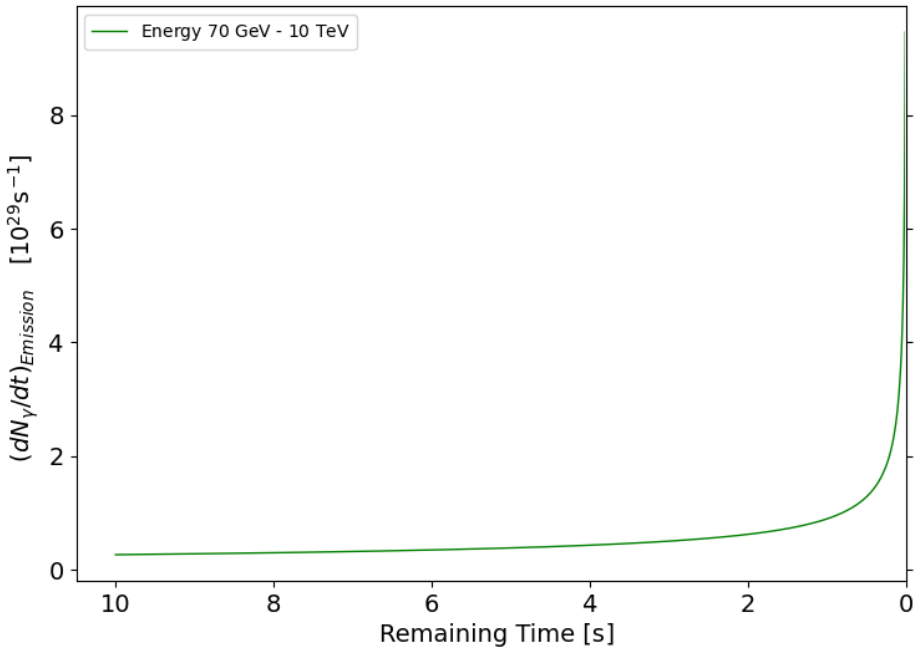

Figure 1.4: Temporal emission profile of a PBH burst, integrated from 70 GeV to 10 TeV.

obtained by fitting the simulations performed by MacGibbon et al. (1990) on the photon flux from a BH with temperature $1\,\mathrm{GeV} \leq kT_{\mathrm{BH}} \leq 100\,\mathrm{GeV}$,

$$\frac{dN}{dE} \approx 9 \times 10^{35} \begin{cases} \left(\frac{1\mathrm{GeV}}{kT_\tau}\right)^{3/2} \left(\frac{1\mathrm{GeV}}{E}\right)^{3/2} \mathrm{GeV}^{-1} & \text{for } E < kT_\tau \\ \left(\frac{1\mathrm{GeV}}{E}\right)^{3} \mathrm{GeV}^{-1} & \text{for } E \geq kT_\tau \end{cases} \tag{1.17}$$

where T_τ is the temperature of the BH at the beginning of the burst time interval.

The alternative spectrum is shown in the bottom plot of fig. 1.3 for the same remaining lifetimes as the top plot. The main difference between both parametrizations is that eq. (1.17) does not take into account the photons that are directly radiated by PBHs.

This approximation and the ones from eq. (1.13) and eq. (1.10) can be used to determine the sensitivity of MAGIC to the time-integrated signal of a PBH burst. Indeed, some experiments have used the former expression (Ackermann et al. 2018) while others have used the latter (Albert et al. 2020) in their search for PBHs. In chapter 7, we will compare the upper limits obtained from the use of both parametrizations.

The emitted radiation and spectrum of the final moments in PBH evaporation depends on the high-energy physics model considered. In this work we considered the SEM (MacGibbon et al. 1990 and MacGibbon 1991), where PBHs emit short bursts of high-energy gamma-rays in the GeV - TeV range at the end of their lifetime. This makes them a good candidate to be observed by IACTs like MAGIC.

Confirmed detection of a PBH burst - beyond proving their existence and allowing the determination of their relic density and rate-density of evaporation - would provide valuable insights into many areas of physics, including fundamental processes in the very early Universe and particle physics at energies higher than currently achievable by terrestrial accelerators. Even the non-detection of PBH burst events in dedicated searches would yield important constraints about the early Universe.

One of the most important reasons to search for PBHs is to constrain the cosmological density fluctuation spectrum in the early Universe on scales smaller than those constrained by the cosmic microwave background (Chapline 1975). The local clustering enhancement of PBH number density in our galaxy can be very large (Carr 2003). As a result, the limits from direct searches of PBHs can be much stronger than indirect limits from measurements of diffuse gamma ray extragalactic background. A particularly interesting question is whether or not PBHs were formed from the quantum fluctuations associated with many different types of inflationary scenarios (Carr et al. 2010). Detection or upper limits on the number density of PBHs can thus also inform inflationary models. In this work we used the non-detection of PBH burst signals to set upper limits on their evaporation rate density in the local vicinity of the Earth and to obtain their density ratio in the early Universe. Those results are detailed in chapter 7, section 7.3 and section 7.3.3.

Chapter 2

Gamma-ray detection

The ElectroMagnetic (EM) spectrum covers more than 20 orders of magnitude in energy, with gamma-rays in the highest range ($E_\gamma > 0.1\,\mathrm{MeV}$). Although the atmosphere on Earth is transparent to photons in the optical ($1.5\,\mathrm{eV} < E_\gamma < 3.43\,\mathrm{eV}$) and radio bands ($6.20 \times 10^{-8}\,\mathrm{eV} < E_\gamma < 1.24 \times 10^{-3}\,\mathrm{eV}$), the rest of the spectrum does not reach the ground. For lower energy photons, this is caused by the absorption or scattering by air molecules, while photons with energies $E_\gamma > 300\,\mathrm{MeV}$ suffer pair production in the vicinity of the atmospheric nuclei. A diagram depicting the EM spectrum and the transparency of the atmosphere is shown in fig. 2.1.

The direct detection of gamma-rays is performed via space-borne instruments, since these photons do not reach the ground. These satellites carry pair-conversion detectors that work in the High-Energy (HE) regime. Due to the steep decrease on flux for photons of energies $E_\gamma \gtrsim 300\,\mathrm{GeV}$, the small collection area ($\sim \mathrm{m}^2$) of these satellites is insufficient for acquiring enough statistics to provide scientific results.

In the Very-High-Energy (VHE) regime ($100\,\mathrm{GeV} \lesssim E_\gamma \lesssim 100\,\mathrm{TeV}$), the IACTs, with larger collection areas ($\sim 10^5\,\mathrm{m}^2$) can perform indirect detection of gamma-rays. A VHE particle, impinging the atmosphere, interacts with the air nuclei producing a cascade of other particles called EAS. The IACTs then detect the Cherenkov radiation produced by those EAS.

In this chapter we will go over the physical principles behind the formation of EASs and the imaging atmospheric Cherenkov technique. We will also

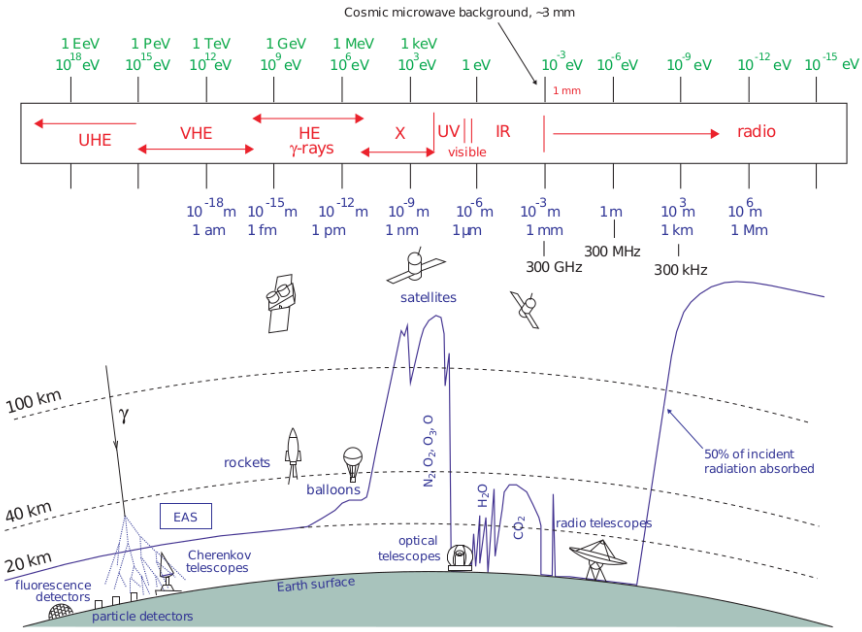

Figure 2.1: (**Top**) EM spectrum and its bands. (**Bottom**) Photon transmission in the atmosphere and the different type of detectors. Figure from Wagner (2006).

give an overview of the hardware and software of the IACT used for the development of this work: the Major Atmospheric Gamma-ray Imaging Cherenkov (MAGIC) telescopes.

2.1 Extended air showers

This section is a summary of Rossi et al. (1941) and Grieder (2010), adapting some of the notation used by the authors and providing the current measurements (Workman et al. 2022a) of some key parameters.

When a high energy particle (primary particle) enters the Earth's atmosphere and interacts with a nuclei, it creates new particles (secondary particles). These particles can interact with other atmospheric nuclei on their way down, thus creating more particles (see fig. 2.2). This process continues as long as the energy of the created particles is higher than the so-called critical energy, E_c, when ionization losses dominate over bremsstrahlung. The product of this cascading effect is commonly referred to as EAS. EAS are divided into two categories depending on the nature of the primary particle: hadronic showers and

EM showers. The former are initiated by protons or heavier nuclei, whereas the latter are initiated by photons or leptonic particles like electrons.

The detection of VHE gamma-rays is hindered by the large background from hadronic showers. The proportion of hadronic to EM showers is about 1000 to 1, so the characterization of their properties is essential for their distinction and later discrimination.

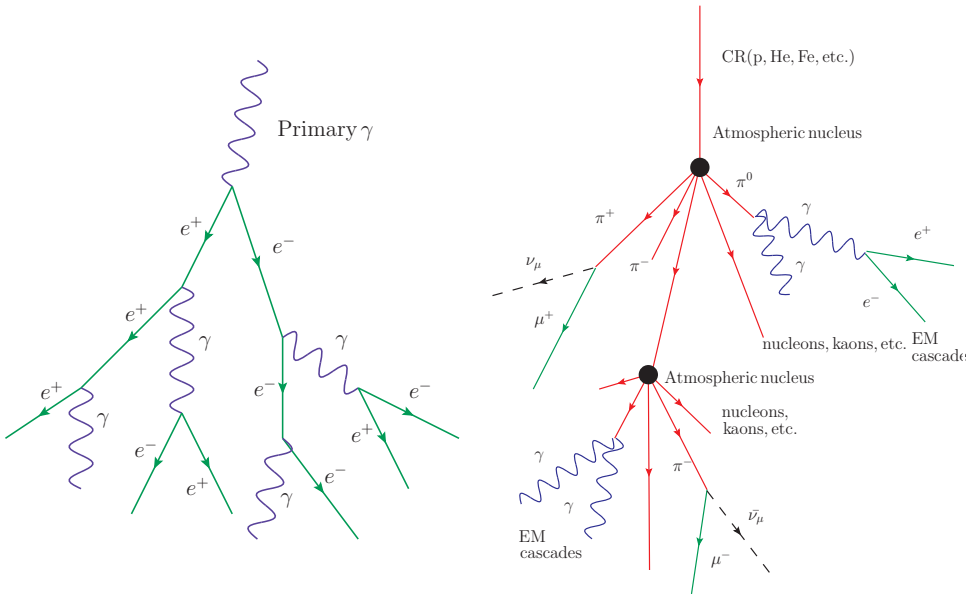

Figure 2.2: Sketch of an EM shower (**left**) and of a hadronic shower (**right**).

2.1.1 Electromagnetic showers

The main interaction processes in EM showers are pair-production and bremsstrahlung. The cross section of pair-production[1] makes it the dominant mechanism for photons of energies $E_\gamma \gtrsim 17\,\mathrm{MeV}$ in the air, while bremsstrahlung causes the energy loss of electrons over $E_\mathrm{c} = 87\,\mathrm{MeV}$ in the same medium. Bremsstrahlung photons with enough energy undergo further pair-production, thus continuing the development of the electron, positron and

[1] This process consists in the creation of a pair of particle-antiparticle by a neutral boson, but in this work we will use it exclusively to describe the case of a photon creating an electron and positron pair.

gamma-ray initiated shower[2]. The energy loss for an electron of $E \gg E_c$ in a path dX is characterized by (Gaisser et al. 2016)

$$\frac{dE(X)}{dX} = -\frac{1}{X_0}E(X)\,, \tag{2.1}$$

with X_0 the radiation length, that is, the mean distance over which the electron loses all but a fraction $\frac{1}{e}$ of its energy. $X_0 = 37\,\mathrm{g/cm^2}$ (Workman et al. 2022a) for electrons (positrons) in the air. Pair production can occur when the incident photon has a minimum energy of $E_\gamma = 2m_e c^2 \approx 1.022\,\mathrm{MeV}$ and is in the presence of a nucleus for momentum conservation.

The process is related to bremsstrahlung in the high energy limit such that its cross section can be written as

$$\sigma_{\mathrm{pair}} \sim \frac{7}{9}\frac{A}{N_\mathrm{A} X_0}\,, \tag{2.2}$$

where A is the averaged mass number of the air and N_A the Avogadro number. The mean free path, λ_{pair} is then

$$\lambda_{\mathrm{pair}} = \frac{1}{n\sigma} = \frac{A}{N_\mathrm{A}}\frac{9}{7}\frac{N_\mathrm{A} X_0}{A} = \frac{9}{7}X_0\,. \tag{2.3}$$

The concepts of radiation length and mean free path are useful in the construction of a simple model for the development of EM cascades, the Heitler model (Heitler 1936). This simple geometric model works under various assumptions:

- $\lambda_{\mathrm{pair}} = X_0\,.$
- After traversing a distance of X_0 an electron will radiate a photon. In the case of a photon, it will create an electron/positron pair.
- The daughter particles share equal parts of the parent particle energy.
- The cascade reaches a maximum when the energy of the individual daughter particles is equal to the critical energy E_c.

While the model tends to overestimate the quantity of elec-

[2]Gamma-ray induced showers might also contain muons, since the cross section for $\gamma \to \mu^+\mu^-$ is small but not zero for TeV photons (Braibant et al. 2012).

trons/positrons and underestimate the depth of the shower maximum (Matthews 2005), it accurately accounts for the two principal attributes of electromagnetic cascades:

- The number of daughter particles in the cascade is directly proportional to the energy of the primary particle E_0.
- The depth of the shower maximum, $X_{\max}$ is proportional to $\ln(E_0/E_c)$.

This process is also applicable to cascades initiated by electrons rather than photons. These cascades start and reach their maximum at a slightly higher altitude due to the smaller radiation depth of bremsstrahlung.

The first interaction point of a gamma-ray induced shower has a very small dependence with the energy of the primary particle (Hubbell et al. 1980), whereas the longitudinal development of the shower is dependent on that energy. Higher energy particles create deeper showers with lower heights of the shower maximum ($H_{\max}$).

The lateral distribution of EM showers is governed by the opening angles of pair production and bremsstrahlung and by the Coulomb scattering of its electrons. The opening angles of the aforementioned processes are small due to the high energy of the primary, so the lateral spread is mainly determined by Coulomb scattering. For an incident $1\,\mathrm{TeV}$ vertical gamma-ray, the radius of the shower is $R \sim 80\,\mathrm{m}$ at sea level and $R \sim 200\,\mathrm{m}$ at the position of the shower maximum (Leo 1994).

2.1.2 Hadronic showers

When the primary particle of the EAS is a cosmic nuclei, the development of the cascade is driven by strong force interactions. Usually, the primary particle is a proton and the majority of these interactions produce positive, negative and neutral pions in the same proportion. A smaller portion of the created particles are kaons and light baryons like protons and neutrons.

Neutral pions decay immediately into photons (Workman et al. 2022b), which, in turn, create EM showers. These are called sub-showers and are indistinguishable from gamma-ray originated showers. The charged pions have a much longer lifetime and continue as part of the cascade, interacting with other particles until their energy reaches $E_c = 20\,\mathrm{GeV}$. Below that critical energy the charged pions decay in the following way (Engel et al. 2011, Letessier-Selvon et

al. 2011):

$$\pi^+ \rightarrow \mu^+ + \nu_\mu \,,$$
$$\pi^- \rightarrow \mu^- + \bar{\nu}_\mu \,.$$

The cascade stops developing when the energy of the particles falls below the one pion threshold of $\sim 280\,\mathrm{MeV}$. Hadronic showers have much more complex and varied processes than EM showers (see fig. 2.2), making their longitudinal and transversal profiles more complicated and less symmetric, which is useful for their identification. Their longitudinal development and first interaction point depend heavily on the mass of the primary particle, thus creating large fluctuations (see fig. 2.3), and they usually develop deeper in the atmosphere than EM showers. Moreover, the transverse momentum of hadronic interactions ($p_\mathrm{T} \sim 400\mathrm{MeV}$, Gaisser et al. 2016) is larger than the resulting momentum from Coulomb scattering, resulting in a lateral spread of the order of $\sim \mathrm{km}$ in hadronic showers.

2.2 Cherenkov light

A charged particle traversing a dielectric medium of refractive index n with velocity $v = \beta c$ polarizes the molecules in its way. If the speed of the particle is $v < c/n$, the polarization is symmetrical around the particle, and the EM waves created by the molecules transitioning to their original state cancel each other out. On the other hand, if $v > c/n$, the particle travels faster than the EM radiation that causes the polarization, thus creating a linear symmetry where the interference of the waves created in the depolarization is constructive (see fig. 2.4).

According to the Huygens-Fresnel principle, the waves interfere constructively only along a cone with opening angle θ_c (the Cherenkov angle) with respect to the direction of the charged particle following

$$\cos\theta_\mathrm{c} = \frac{c/n}{v} = \frac{1}{\beta n} \,. \tag{2.4}$$

This effect is called Cherenkov radiation and was first discovered in 1934 by Pavel Cherenkov (Cerenkov 1937).

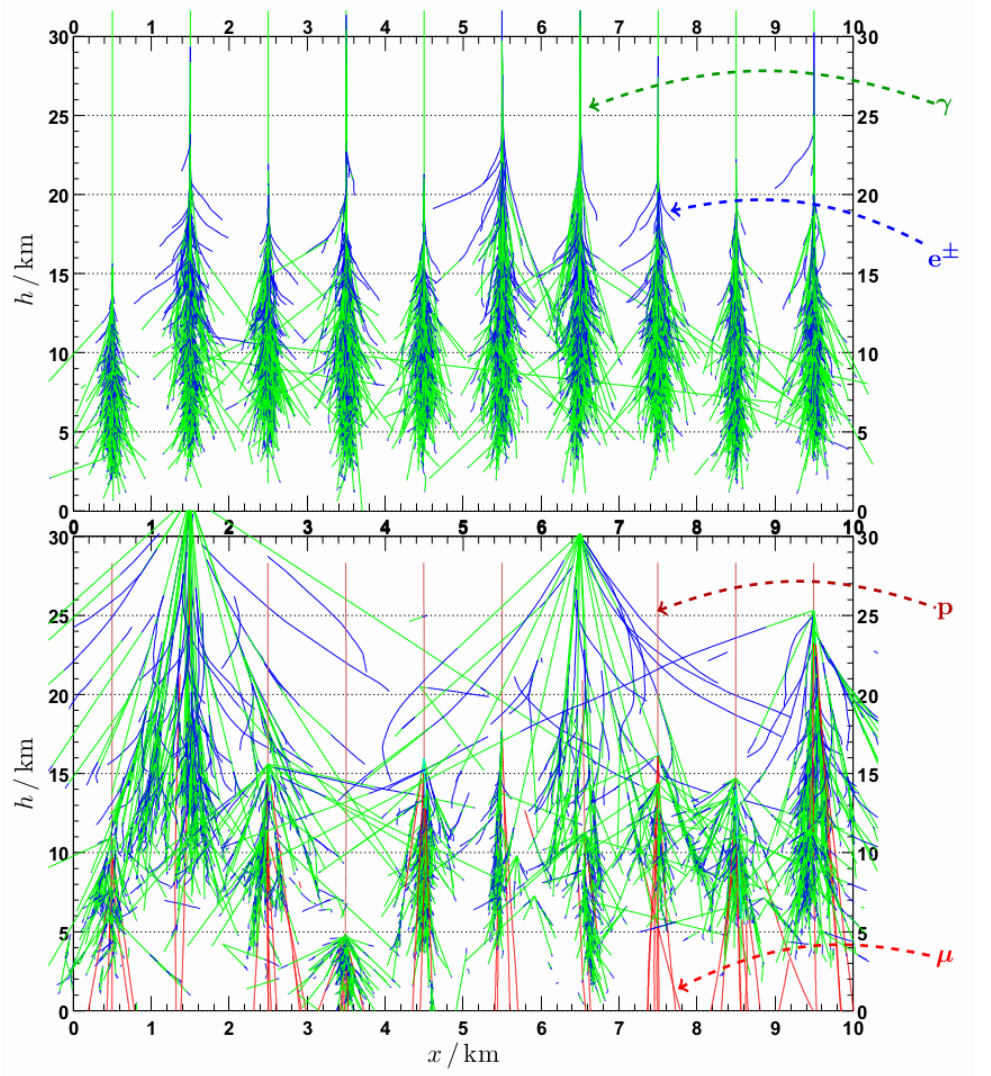

Figure 2.3: Shower development from gamma-ray and proton primaries from Monte Carlo (MC) simulations. The plots showcase the intrinsic variability of EAS with 10 vertical shower simulations triggered by gamma-rays in the upper panel and protons in the bottom panel. The energy of the primary particle in each case is 300 GeV. Figure modified from Naurois et al. (2015).

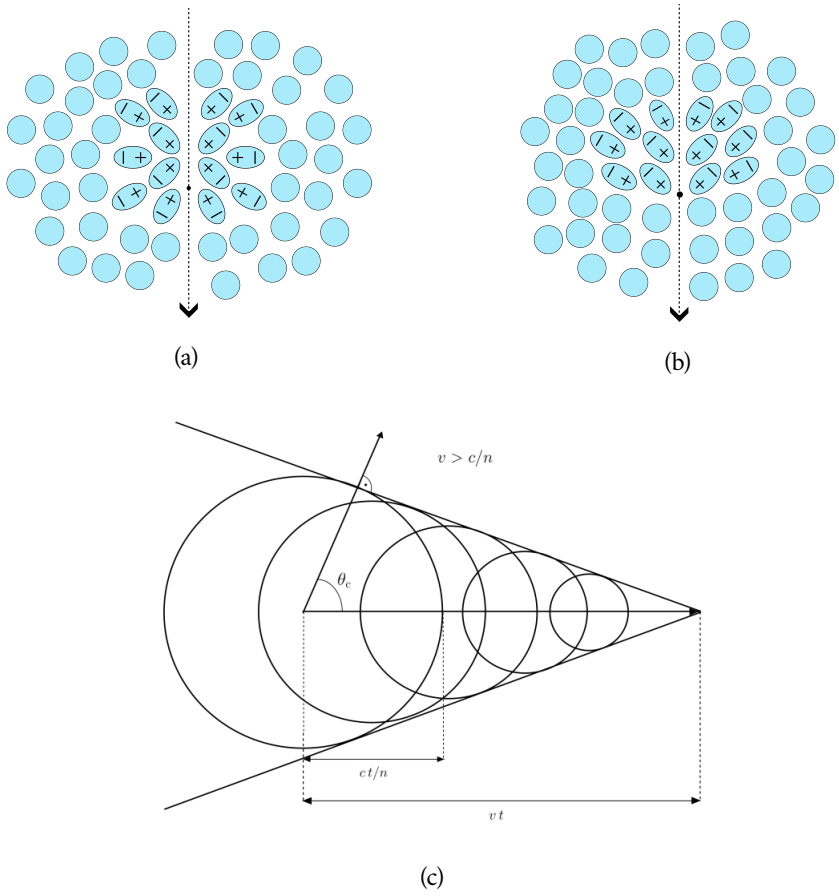

Figure 2.4: **a)** Polarization of a dielectric medium when crossed by a charged particle with $v < c/n$. **b)** Polarization of a dielectric medium when crossed by a charged particle with speed $v > c/n$. **c)** Construction of the Cherenkov wave front using the Huygens–Fresnel principle.

From eq. (2.4) we can see that the emission of Cherenkov light depends on the refractive index of the atmosphere. This index, in turn, depends on the properties of the atmosphere, so, for temperature $T = 20\,^{\circ}\mathrm{C}$ and pressure $P = 1\,\mathrm{atm}$, the energy threshold for Cherenkov emission is $E_{\mathrm{thr}} \approx 21\,\mathrm{MeV}$ for electrons, $E_{\mathrm{thr}} \approx 4.4\,\mathrm{MeV}$ for muons and $E_{\mathrm{thr}} \approx 39\,\mathrm{GeV}$ for protons. These thresholds increase rapidly with the altitude as the refractive index diminishes.

The number of Cherenkov photons emitted depends on the wavelength of the particle and can be derived from the Frank and Tamm formula for the

energy loss (Frank et al. 1937)

$$\left(\frac{d^2E(\omega)}{dld\omega}\right) = \frac{(ze)^2}{c^2}\omega\left(1 - \frac{1}{\beta^2 n^2(\omega)}\right), \tag{2.5}$$

where ω is the frequency of the radiated photons and l is the path length of the traversing particle, as

$$\left(\frac{d^2N(\lambda)}{dld\lambda}\right) = \frac{2\pi\alpha}{\lambda^2}\left(1 - \frac{1}{\beta^2 n^2(\lambda)}\right) \approx 379\sin^2\theta_c(\lambda)\mathrm{eV}^1\mathrm{cm}^{-1}, \tag{2.6}$$

where $\alpha \approx 1/137$ is the fine structure constant and $\lambda = \frac{2\pi c}{\omega}$ is the wavelength of the radiating particle. From this equation we can see that the number of Cherenkov photons is proportional to $1/\lambda^2$ and that the spectrum from this light will peak at lower frequencies.

2.2.1 Shower light development

This is an overview of how different factors such as the atmosphere, the primary particle and the relative position of the observer with respect to the shower affect the Cherenkov photons detected by IACTs. For a detailed description, the reader is referred to Ishio (2020).

The Cherenkov light cone emitted by particles at a given height h illuminates a ring on the ground with radius R_c, denominated the Cherenkov radius. R_c depends on the observational height h_{obs} above sea level (a.s.l), and the Cherenkov angle,

$$R_c = (h - h_{obs})\tan\theta_c . \tag{2.7}$$

Due to hydrostatic pressure, the density of the atmosphere and, consequently, the refractive index, increases towards lower altitudes. As a consequence of the varying refractive index, the overlapping rings of Cherenkov light from different altitudes predominantly illuminate a circular area around the impact point of the shower axis on the ground, known as the light pool, with a radius ranging from $80\,\mathrm{m}$ to $130\,\mathrm{m}$. The illumination within this region is relatively uniform, while the edge of the circle is most intensely illuminated, creating a so-called hump. Due to the lateral spread of the shower caused by multiple Coulomb scattering, shower light can also be observed beyond the hump, albeit with an exponentially decreasing lateral light distribution with distance.

While gamma-ray showers conform to the aforementioned description, hadronic showers typically initiate multiple EM sub-showers and have a large transverse momentum, creating a less regular footprint, as seen in fig. 2.5, characterized by several sub-light pools and light distributed comparatively farther away from the core of the shower. Differences between gamma-ray and

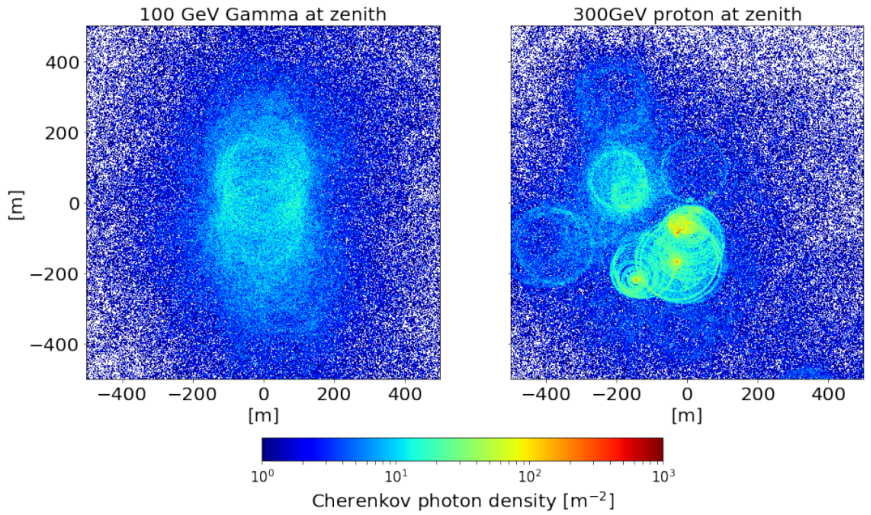

Figure 2.5: Cherenkov photon density distributions at ground level for simulated showers with incoming directions perpendicular to the telescopes. The left panel shows the distribution for MC simulated showers with a 100 GeV gamma-ray primary and the right panel shows the distribution for MC simulated showers with a 300 GeV proton primary. Figure extracted from Ishio (2020). Original credit to Chai Yating.

hadronic showers extend to the Cherenkov light they generate in more ways. As with the number of daughter particles in an EAS, the photon density of Cherenkov light is directly proportional to the energy of the primary particle. This relation is only true at higher energies for hadronic showers(Oser et al. 2001).

2.2.2 Atmospheric absorption

Cherenkov photons are emitted mostly in the UV and optical range, according to eq. (2.6), with a λ^{-4} dependence. However, the observed Cherenkov spectrum differs from the emitted one due to the different absorption processes in the atmosphere that especially affect photons with wavelengths below 300 nm (see fig. 2.6). The most relevant ones are:

- **Rayleigh scattering**: Caused by the atmospheric molecules, atoms and particles smaller than the wavelength of the incident radiation[3]. Its cross section is proportional to λ^{-4}, thus being more prominent on shorter wavelengths (UV rays).

- **Mie scattering** : Caused by particles with a size comparable to or bigger than the wavelength of the radiation, mostly man-made aerosols. This scattering is complex and depends on the particle composition of the aerosols, which can change rapidly depending on wind conditions. A model is normally used to calculate the total aerosol extinction, such as the one contained in the MODTRAN program (Bernlohr 2000).

- **Ozone molecules** : Wavelengths below $290\,\mathrm{nm}$ are absorbed by ozone.

- **H2 and CO2 molecules** : They cause the absorption of infrared photons (wavelengths larger than $800\,\mathrm{nm}$).

- **Zenith distance** : Showers created by a particle entering the atmosphere at a large Zenith distance (Zd) will have more attenuation. The particles travel a longer path and the probability of absorption increases. Thus, only EAS with a very energetic primary particle are detected at high Zd ranges.

The combination of these processes causes the observed Cherenkov spectrum to peak at around $330\,\mathrm{nm}$ independently of the energy of the incident particle. In EM showers, the electron-positron pairs all have energies above the Cherenkov threshold and emit Cherenkov radiation. Consequently, the number of Cherenkov photons produced in the shower is proportional to the total number of electrons and positrons in the shower and, therefore, proportional to the energy of the primary particle.

This relation allows us to infer the energy of the incident gamma-ray from the total Cherenkov light intensity of the created EAS. In the case of a vertically incident gamma-ray, the overlap of the conical wave fronts of each emitting particle creates a circular light pool within which the photon density is approximately constant. The radius of this area depends on the altitude of the observation and is $\simeq 120\,\mathrm{m}$ at the MAGIC site, at $2200\,\mathrm{m}$ a.s.l.

[3] Rayleigh scattering is responsible for the blue colour of the sky during daytime and the reddish tones of dusk.

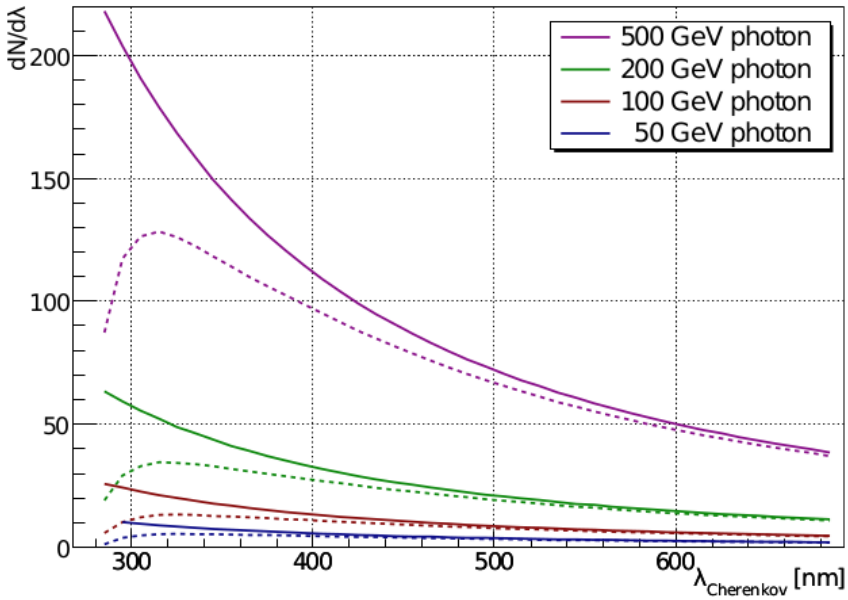

Figure 2.6: Spectra of Cherenkov light produced by EAS initiated by gamma-ray primaries of different energies. The solid lines show the Cherenkov light spectra at 10 km height and the dotted lines show the observed spectra at 2.2 km a.s.l after Rayleigh and Mie scattering. Figure extracted from Wagner (2006).

2.3 Imaging technique

In the previous sections we described the processes undergone by high energy particles arriving at Earth and their effects on the atmosphere. In this section we will describe how ground-based telescopes benefit from the results of such interactions to detect VHE emission from galactic and extragalactic sources through the *Imaging Atmospheric Cherenkov Technique*. The aim of this technique is to measure the image of the EAS and use its spatial, temporal and intensity properties to estimate its incoming direction and energy and distinguish a gamma-ray initiated shower from CR initiated ones. The intrinsic faintness of Cherenkov light [4] and the short duration of the pulse emitted in an EM shower, $\sim$2 ns, requires a telescope with a large collection area and a pixelized camera equipped with very fast detectors like PhotoMultiplier Tubes (PMTs).

[4] A shower originated by a 100 GeV gamma-ray has a light pool with approximate photon density of 10 photons/m^2.

IACTs employ large reflectors that project light onto the camera focal plane using parabolic or spherical mirrors. This mirror system ensures that rays arriving at the same angle are focused onto the same point in the plane, effectively converting incident angles into distances from the camera centre. As the Cherenkov angle varies along the trajectory of the shower, light from different parts of the shower is reflected into different positions in the camera plane, thus creating an image. In fig. 2.7 a diagram of the imaging technique shows the geometrical relations between a gamma-ray initiated EAS and the image obtained in the focal plane of the telescope.

The images obtained in the camera have different features depending on the type of EAS observed, as shown in fig. 2.8. Cherenkov light from an EM cascade usually appears as an elliptic shape, with mean width and length of $\sim 0.1^\circ$ and $\sim 0.3^\circ$. The major axis of the ellipse reflects the longitudinal development of the cascade, as seen in fig. 2.7, with the shower maximum appearing as the brightest point around the centre of the ellipse. Depending on the relative orientation of the shower's axis and the optical axis of the telescope, the orientation and symmetry of the ellipse change, even appearing as a circular shape in the centre of the camera in the case of matching axes.

As it was previously described, hadronic showers are much more asymmetric and wide than their EM counterparts, resulting in irregular shapes in the camera, as large as $\sim 1^\circ$, which makes it easier to reject them. Modern IACTs are composed of more than one telescope for better background suppression and better reconstruction of the direction of the incident gamma-ray.

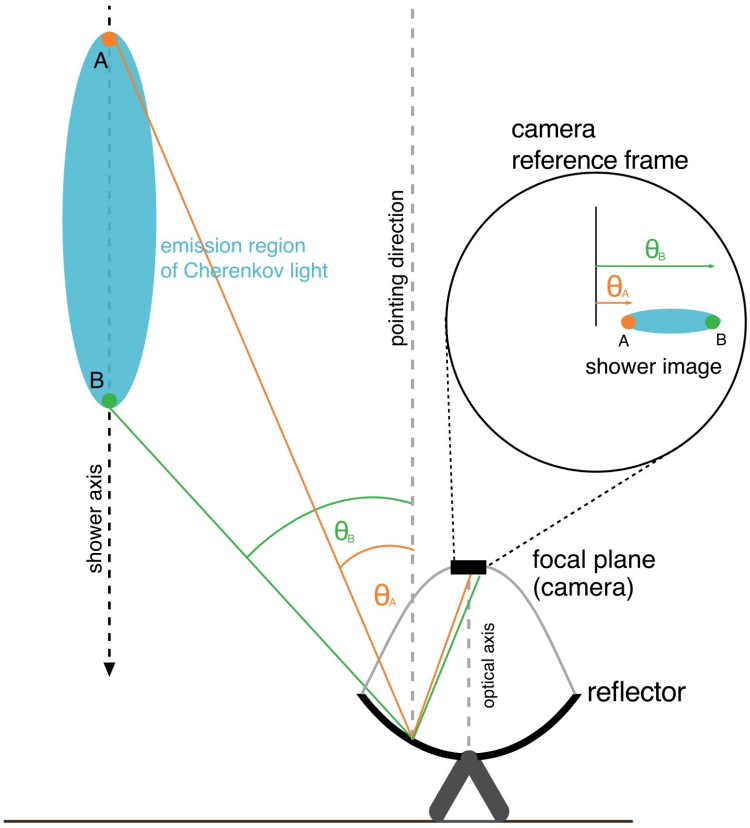

Figure 2.7: Diagram of the imaging technique. A gamma-ray originated shower illuminates the telescope and is reflected into the camera located in the focal plane of the reflector. Two example trajectories of Cherenkov light from different regions in the shower are shown in green and orange, with their corresponding locations in the shower image from the frame of reference of the camera. In this example, the shower axis is parallel to the pointing direction of the telescope, which results in an elliptical image with its major axis pointing to the centre of the camera. The light trajectories are drawn to illustrate the technique and may not realistically follow the principles of optics.

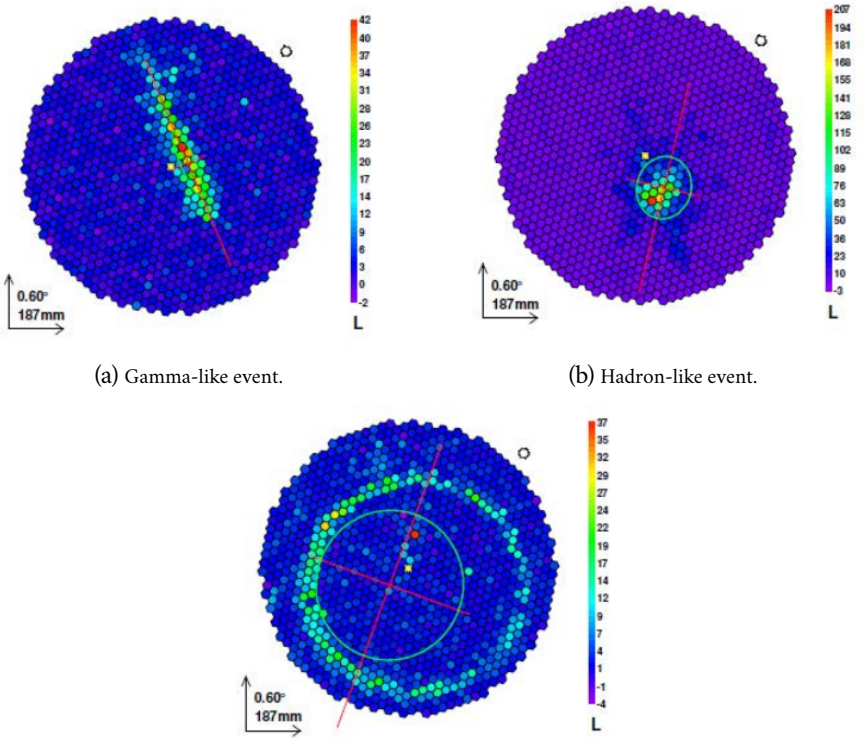

(a) Gamma-like event.

(b) Hadron-like event.

(c) Muon-like event.

Figure 2.8: Examples of real events captured by the PMTs in the camera of M-II. **a)** Shows the typical ellipse from an EM shower candidate observed at low Zd. **b)** This irregular shape likely corresponds to a hadron initiated shower and **c)** is the characteristic muon ring originated from the secondary particles in a hadronic shower. Images extracted from Aleksić (2013).

Chapter 3

The MAGIC telescopes

Figure 3.1: Picture of the MAGIC telescopes on the Roque de los Muchachos observatory. From left to right we have MAGIC-I, MAGIC-II and the counting house (the data taking building) with the LIDAR dome on top. The large structure seen in the background is the Gran Telescopio de Canarias (GTC). Image credit: Robert Wagner.

The MAGIC telescopes (fig. 3.1) are a stereoscopic system of two 17 m diameter telescopes located at the Roque de los Muchachos observatory at La Palma (Spain) at an altitude of 2200 m a.s.l. MAGIC was originally composed of a single telescope, MAGIC-I (M-I), which started operations in the year 2004 with the largest reflector at the time[1] and was joined in 2009 by its clone, MAGIC-II (M-II), for stereoscopic observations. The system was last upgraded

[1] This record was held until 2012, when the 28 m diameter H.E.S.S.-II telescope started operations.

in 2012, when the camera and readout system of M-I were replaced to match the newer M-II [2].

Their design, with a large reflector area, sensitive and fast cameras, an optimized distance between the telescopes and a light-weight structure allows them to reach a very low energy threshold and fast repositioning, a key factor in the detection of GRBs. This design was proven a success when 15 years after the start of operations MAGIC detected the first GRB in VHE (Mirzoyan 2019).

The current energy threshold is $\sim 50\,\mathrm{GeV}$ for low zenith distance observations under dark conditions (Aleksic et al. 2012) and a repositioning of $180°$ is achieved in less than $20\,\mathrm{s}$.

3.1 Hardware

In this subsection we will give a brief overview of the main hardware components and subsystems of the MAGIC telescopes. More detailed descriptions can be found in (Aleksić et al. 2015a) and (López-Coto 2015).

3.1.1 Reflector

Each telescope has a $17\,\mathrm{m}$ diameter tessellated reflector with an approximately parabolic surface and a focal length of $17\,\mathrm{m}$. The reflective plane of the two telescopes forms a parabolic octagonal surface with an area of approximately $234\,\mathrm{m}^2$, comprised of individual mirror panels of $1\,\mathrm{m}^2$ each. Despite prevalent aberrations like coma and astigmatism, this reflecting surface is optimal for achieving isochronous focus.

Although the mirror shapes tessellating the telescopes are spherical, their radius of curvature are increased from the centre of the dish ($33.9\,\mathrm{m}$) to its edges ($36.4\,\mathrm{m}$) to approximate an overall parabolic shape. This ensures isochronicity for signals reflected at the same angular distance from the surface center, preserving the temporal structure of a Cherenkov light pulse reflected on the camera within $0.6\,\mathrm{ns}$. Consequently, this enhances the signal-to-noise ratio of the photon pulse in each camera pixel. This improvement allows for narrower integration windows in the search for signals, reducing background interference

[2] See Aleksić et al. (2015a) and Aleksić et al. (2015b) for the current performance of the updated system.

from spurious night sky light or stars.

The position of each mirror is controlled with a dedicated software and individual actuators that work to minimize the total Point Spread Function (PSF) of the reflector and counteract the deformation of the structure during the movement of the telescope.

In contrast with optical telescopes that are protected by a dome whenever they are not in operation, MAGIC's reflectors are exposed to the climate and the possible contact of foreign objects. The mirrors have a delicate front coating that enhances the transmittance of blue and ultraviolet photons. This coating can be easily damaged by contact, which prevents the reflector form being manually cleaned and its reflectivity can be significantly reduced in the case of calima [3]. Luckily, the rain storms of late summer remove the calima debris and the reflectivity is recovered.

3.1.2 Camera

The pixelized camera of MAGIC is composed of 1039 PMTs arranged in an hexagonal lattice. The photo cathodes of these PMTs have a circular shape, so the gaps between them are covered by hexagonal Winston Cones that help increase light collection. Each pixel has a Field of View (FoV) of about 0.1° and the full camera has a FoV of 3.5°.

The camera, weighing 850 kg, is mounted in front of the reflector on an aluminium arc supported by steel cables tied to the dish frame. The PMTs and electronics are insulated and protected from the exterior with a polymethyl methacrylate window and movable lids, while the Data AcQuisition system (DAQ) (the trigger and readout systems) are located in a specialized building at a few tens of meters distance, the Counting House (CH).

3.1.3 Trigger and readout

The optical signal from the individual PMTs arrives at the receiver boards in the CH, where it is converted into an electrical signal. This signal is split into a digital trigger branch and an analogue readout branch. The trigger region is

[3] This is a meteorological phenomenon caused by the high concentration of dust, ash or sand. The island of La Palma is commonly subject to this condition in the summer months due to its closeness to the Sahara desert.

formed by the inner 547 pixels of the camera, spanning a radius of $1.17°$.

The trigger logic consists of three levels (Aleksić et al. 2015a), which we outline here:

- **Level 0 (L0):** The lowest level trigger is applied by the receivers to each pixel. It evaluates if the signal amplitude from a PMT is above a discriminator threshold and issues a digital 1 in the positive scenario. It is calibrated during observations to take into account the Night Sky Background (NSB) level and avoid accidental triggers. The L0 rate is $\sim$ 800 kHz with the discriminator threshold typically set to $\sim$ 5 photoelectrons (phe).
- **Level 1 (L1):** This trigger is a digital coincidence filter that searches for n Next Neighbour (NN) pixels around the L0 signal, within a 8 ns to 9 ns time frame. The number of neighbouring pixels is configurable, but it is usually 3 for stereoscopic observations.
- **Level 3**[4] **(L3):** This is the stereo trigger. It receives the L1 trigger signals from both cameras and checks for temporal coincidence between them by stretching them to 100 ns and then delaying them according to the zenith and azimuth orientation of the telescopes to take into account the different arrival times of the Cherenkov photons to each telescope. L3 activates the individual telescope readout when it receives a signal from both L1 triggers within 200 ns. It has a rate of 250 - 350Hz.

MAGIC utilizes two additional trigger systems: the Sum-Trigger (Dazzi et al. 2015) and the Topological (Topo) trigger (López-Coto et al. 2016). However, as all the data utilized in this study were obtained using the trigger system described previously, further explanation of these additional trigger systems will not be provided in this work and the reader is referred to the aforementioned articles.

The readout system of MAGIC is provided by the Domino Ring Sampler chip version 4 (DRS4) (an in-depth description can be found in Sitarek et al. (2013) and Bitossi et al. (2016)). This is an analogue memory chip with 1024 switching capacitors with a sampling frequency of 0.7 to 5 GSamples/s. In MAGIC, the sampling frequency is tuned to 1.64 GSample/s to take into ac-

[4]The L2 trigger was a system that worked on top of the L1 trigger of M-I, but it is no longer in use.

count the delay in signals between the two telescopes.

The DRS4 chips can recover a smaller number of 50 relevant capacitors around the signal arriving time, which are readout sequentially by Analogue Digital Converters (ADC). That is, whenever the L3 trigger is activated, a time series of 50 values is stored for all the pixels in the camera. This allows us to digitize less signals, thus reducing the dead time to 26 µs, which is negligible compared to the data acquisition rate of 250 Hz (Aleksić et al. 2015a). The duration of the shower signal is defined by the sampling speed and the length of the readout capacitor chain as $1.64\text{GHz} \times 50 = 30.5\text{ns}$.

3.1.4 Auxiliary subsystems

Other relevant subsystems that are needed for the correct and safe operation of the MAGIC telescopes are:

- **Pyrometer and Light Detection And Ranging (LIDAR):** Two instruments measure the atmospheric transmission, assessing the data quality. A pyrometer, installed in the dish of M-I estimates the transparency of the atmosphere by measuring the temperature of the sky in the pointing direction. The presence of clouds causes the reflection of infrared light from Earth and, therefore, causes an increase in the sky temperature that is transformed into the *cloudiness* parameter. The LIDAR provides a more accurate measurement of the atmosphere's transmission. Its laser fires light pulses in the pointing direction of the telescope that are backscattered by clouds or aerosols and detected back by the LIDAR. The arrival time distribution of the photons can be used to measure the transmission of the atmosphere at different heights.
- **Drive monitoring:** The pointing of the telescopes, precise up to $\sim 0.02°$, is monitored and calibrated with two Charge-Coupled Device (CCD) cameras installed in the centre of the reflector, the *starguider* and the *T-point* cameras. The *starguider* camera constantly monitors the pointing by comparing the position of the camera (a ring of Light Emitting Diode (LED) lights signals the edge of the camera) with the background of stars. The *T-point* camera, in turn, calibrates the pointing of the telescope to take into account any deformation in the structure by taking pictures of stars along the whole range of zenith and azimuth angles.

3.2 Data taking

In MAGIC observations, data are collected in time intervals of approximately $20\,\mathrm{min}$, referred to as *runs*. Depending on the importance of the source that is being observed and its position in the sky, the number of runs dedicated to it will vary, but they usually amount to a couple of hours. In most cases, both telescopes are used, measuring simultaneously and pointing to the same coordinates. This is the *stereo* mode, as opposed to the *mono* mode, where only one telescope is operated. All the data analysed in this work corresponds to stereo observations.

To account for varying performance of the hardware, some calibration procedures are done at the beginning of the telescopes operation every night, as well as in between observations. The performance of the telescopes can vary with the observing conditions, such as the Zd, the quality of the atmosphere or the NSB level. The standard operation of MAGIC, and when the telescopes achieve their best performance, is on nights without moon, which are referred to as *dark* conditions.

This *dark* time amounts to a total of $\sim 1600\,\mathrm{h/yr}$. A $\sim 35\,\%$ of it is lost to bad weather conditions or technical problems. The low gain of the PMTs in the camera allow observations on low moonlight conditions (up to $75\,\%$ of the moon phase), but not on the 3 to 4 full-moon nights, when operations are paused. Moon observations extend MAGIC's duty cycle by a $40\,\%$ (Ahnen et al. 2017a) but the treatment of these data differs from the standard analysis chain. The data analysed in this thesis was taken only during *dark* conditions.

3.2.1 Observation strategies

The relatively small FoV of MAGIC requires that observations have a target source, instead of mapping large areas of the sky. Within the FoV, an ON-region, where the gamma-rays from the target are expected to arrive from, and an OFF-region, a purely background spot for comparison, are defined. Two observation strategies are used in MAGIC's data taking following that premise.

3.2.1.1 ON/OFF mode

In this observation mode, the telescopes are pointing and tracking the coordinates of the target, performing the so-called ON observation for one run. After

that, another run is dedicated to the OFF observation, where the telescope is pointed to a background region with a similar zenith and azimuth path than those for the ON run. This is the simplest configuration for data taking, but one that reduces the amount of observation time available. In addition, the changing of weather, NSB level or the response of the camera, can be fast and make it difficult to maintain the same observing conditions between ON and OFF runs.

3.2.1.2 Wobble mode

The most common observation strategy in IACTs was introduced by Fomin et al. (1994) to maximize the observation time and the background estimation. In this mode, the telescopes are pointed at a slightly offset angle in Right Ascension (R.A.) from the target coordinates in what is called the wobble angle. In MAGIC, the wobble angle is usually $0.4°$, but it can be changed if there are other sources close to the OFF region or if we are observing an extended source.

The advantage of this scheme comes from the use of a simultaneous OFF region that naturally appears as the mirror point of the target ON region. The two regions should in theory have the same acceptance (probability of detecting an event from an EAS within the FoV of the telescopes. This concept is detailed further in chapter 5), but the intrinsic inhomogeneities of the camera can still add systematic effects. This is fixed by adding a rotation angle to the offset in the subsequent runs. The angle is selected depending on the number of runs so that the coverage of the camera is homogeneous, as seen in fig. 3.2, with the simplest choice being two observations with a $180°$ rotation.

3.3 Data analysis

The raw data collected by the readout system is processed and reduced from the time series of the PMTs in the cameras to the main characteristics of the EASs, which allow us to derive scientific results from the VHE particles that arrive at Earth. The data collected by MAGIC is reduced and analysed with the MAGIC Analysis and Reconstruction Software (MARS) (Zanin 2013). This software is a collection of **C++** routines built on top of the **ROOT** framework (Brun et al. 1997) and is only accessible to those within the MAGIC collaboration. In order to maintain a general discussion, and since the work done in this thesis does not involve the treatment of low level, raw data, the following section will give a fast overview of the first steps of data processing.

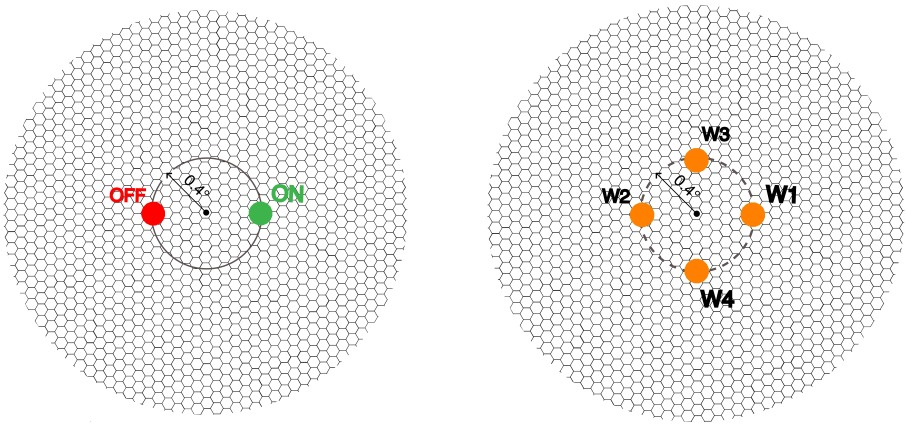

Figure 3.2: Wobble mode diagram with a typical observation configuration of four wobble positions. In the left diagram, we show the camera frame of reference, where the centre of the image corresponds to the pointing of the telescopes and the source is located in the green ON circle. In the right diagram we show the reference frame of the sky, where the centre of the image corresponds to the source position and the orange circles are the offset, wobble pointing positions of the telescopes.

3.3.1 Calibration and image cleaning

An *event* is considered to be anything that triggers MAGIC's readout system (see section 3.1.3). The raw data of MAGIC events contain the charge in ADC counts of the DRS4 capacitors for all the pixels in the cameras for each L3 triggered event and for the interleaved pedestal and calibration events. Every night, an average of $\sim$1 TB of raw data per telescope is produced. These data are paired with the reports from auxiliary systems and saved in **ROOT** format. In the case that the event is induced by an EAS, the resulting time series of the PMTs exhibit a characteristic pulse shape, with a sharp increase followed by a plateau. The area under this pulse is proportional to the number of photons detected by the PMT.

In the first step of data processing, the time series of each PMT pixel is reduced to integrated charge and arrival time. Pedestal events, characterized as randomly triggered events with no signal, are used to estimate the baseline to be subtracted from the pulses. Following this subtraction, the charge of an event is identified by a *sliding window* algorithm that finds the 5 consecutive time slices (an event has 50 time slices as seen in section 3.1.3) that provide the maximum sum. The summed charge in ADC counts is then converted to

units of photoelectrons (phes) with the *F-factor* method (Mirzoyan 1997). The associated arrival time is defined as $t_{\text{arrival}} = \sum_i i s_i / \sum_i s_i$, where i is the time slice number, and s_i is the signal in slice i. A more detailed description on the extraction of photon charge and arrival time and the previous pre-processing of the pixel signals can be found in Aleksić et al. (2015a), Aleksić et al. (2015b) and Albert et al. (2008c).

Even in the darkest conditions, MAGIC's cameras are still continually exposed to some level of NSB. This, together with the electronic noise results in signal counts being detected not only in pixels illuminated by the shower but in all the camera pixels. The next step of data processing is the removal of signal counts from NSB photons and the transformation of the remaining counts into relevant shower image information. Cherenkov light from an EAS illuminates clusters of pixels in the camera in a small ns time window. The core of the image is found by the identification of groups of 2,3 or 4 NN pixels with a summed charge above a given threshold, Q_{core}, and with arrival times within a given time window Δt_{core} (these values are listed in table 3.1).

Topology	$Q_{\text{core}}/\text{phe}$	$\Delta t_{\text{core}}/\text{ns}$
2NN	2×10.8	0.5
3NN	3×7.8	0.7
4NN	4×6	1.1

Table 3.1: Values for the charge threshold and time window in the different NN combinations.

To complete the image of the shower, boundary pixels are selected. The pixels adjacent to the core ones with a signal over $3.5\,\text{phe}$ arriving within a $1.5\,\text{ns}$ window from the signal arrival time of the brightest pixel in the core are included in the image. The plots in fig. 3.3 show the cleaning procedure of an event on the pixels of the camera. After this step, the charge and arrival time information of the remaining pixel signals can be parametrized to deduce key properties of the incident particle.

3.3.2 Hillas parameters

To reduce the amount of information stored for every event and prepare the data for the following steps of energy reconstruction and gamma/hadron sep-

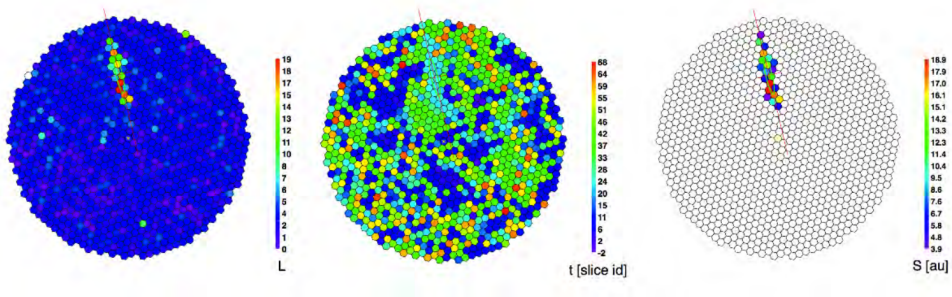

Figure 3.3: Charge distribution (**left**), time distribution (**centre**) and final cleaned image (**right**) of the pixels of an event in the camera of M-II. Image extracted from López-Coto (2015).

aration, the cleaned shower images are parametrized. The initial approach for this data reduction, proposed by Hillas in 1985 (Hillas 1985), and still used to this day with minor adjustments, involves fitting an ellipse to the shower image. The key image parameters used by the MAGIC software are the Centre of Gravity (CoG), the minor (*width*) and major (*length*) axes of the ellipse, the photon count (*size*), the time gradient of signal arrival times along the major axis, and the *leakage*, calculated as the charge contained in the outermost pixel ring of the camera divided by the *size*. Another parameter employed for discriminating hadronic events subsequently is the number of islands, representing the count of distinct regions of pixels surviving the image cleaning process. Storing only the Hillas parameters of the events reduces the total size of data to $\sim$8 GB per night.

3.3.3 Stereoscopic reconstruction

Events that survive the cleaning process in both telescopes are combined to extract information about the position and orientation of the shower. Operating more than one Cherenkov telescope allows us to reconstruct more characteristics from the observed EAS than using only one. Since no Cherenkov light is detected from the impact point of the shower in the ground nor from the arrival point in the atmosphere, the axis of the shower and, therefore, its arrival direction can't be directly inferred. Therefore, the image from a single telescope just determines the orientation of the shower with respect to the optical axis of the telescope. The problem is easily fixed by combining the shower images from both telescopes, which allows us to create a three-dimensional reconstruction of the shower.

The plane defined by the major axis in the Hillas ellipse and the optical axis of the telescope contains the axis of development of the real shower. Therefore, the crossing of the planes from the two images determines the shower axis, as shown in fig. 3.4. The impact point is then given by the crossing of the planes at ground level. Projecting both event images into a common camera coordinate system allows the estimation of the shower direction (Hofmann et al. 1999).

The height of the shower maximum is obtained by projecting the CoG of both images into the sky as shown by the green dashed lines in fig. 3.4. Ideally, the projected lines would intersect with the shower axis at the height of the shower maximum. However, the projection is done taking into account the angular offset of the image from the pointing position, so the lines may not necessarily intersect. Instead, the shower maximum is determined by triangulation, as the height where the perimeter of the triangle formed by the three lines (depicted as the blue triangle in fig. 3.4) is minimized.

Additional physical parameters can be estimated from the shower images once the shower maximum is determined, like the Cherenkov radius R_{C}, and the Cherenkov density ρ_{C}. R_{C} is the radius in the ground of a Cherenkov annulus emitted by an electron with critical energy located at the shower maximum and travelling towards the impact point (see section 2.2.1). ρ_{C} is the density of photons generated by the same electron inside the Cherenkov ring. The reconstructed stereoscopic parameters are used in the analysis chain to estimate the key characteristics of the primary particle of the shower, such as the species, the energy and the direction.

3.3.4 Quality selection

The level of NSB light and the transmission of the atmosphere have a significant effect on the performance of the telescopes and their effects must be accounted for in the analysis. In order to do so, data are categorized based on the sky brightness and transmission conditions of the observation.

Throughout the observations, the NSB spectrum is not measured. Instead, we monitor the Direct Current (DC) of each camera pixel. The NSB level is inferred by comparing the measured median DC in the camera of M-I, with a reference average median DC obtained under well-defined observation conditions (Ahnen et al. 2017b). Data are grouped into levels of NSB by how many times the median DC of their observations exceeds the reference value. Subse-

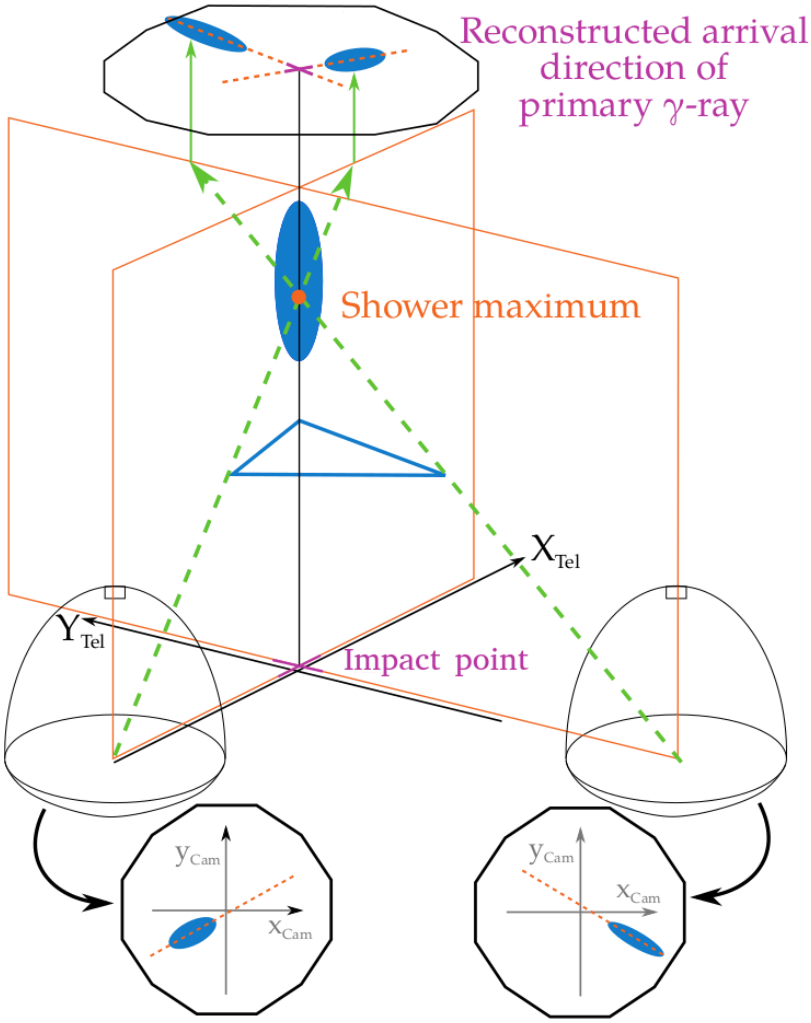

Figure 3.4: Geometry of the stereoscopic reconstruction of the shower parameters with two Cherenkov telescopes. In this diagram we assume a zenith pointing of the telescopes and a shower with axis parallel to the telescopes optical axis. Image adapted from Strzys (2020).

quently, cleaning levels can be adjusted for each group accordingly. The data used in this work was selected to contain only level 1 NSB observations, that is *dark* conditions observations, an thus requires no adjustment of the cleaning procedure outlined in section 3.3.1.

Transmission levels are determined using LIDAR measurements, or, in their absence, they are estimated from pyrometer readings. Additionally, some metrics such as the number of stars in the FoV or the event rate of the telescopes can be used as a measure of atmospheric transmission. However, these measures are less reliable compared to the direct measurements of the LIDAR. Data with transmission levels exceeding $80 - 85\%$ can be analysed using the standard procedure outlined in this section, but lower transmission data have to undergo corrections using the LIDAR profiles. In this work data with an atmospheric transmission of less than $80\,\%$ measured at an altitude of $9\,\mathrm{km}$ with the LIDAR were discarded. When no LIDAR information was available, data were discarded on the basis of the *cloudiness* parameter from the pyrometer, which was selected to be under $45\,\%$.

3.3.5 Monte Carlo simulations

Many of the electronic and optical subsystems of MAGIC are calibrated individually. However, it is not possible to artificially generate gamma-ray shower references in the atmosphere to calibrate the telescopes. It is also impossible to have natural references, since the proportion of hadronic showers against gamma-ray showers is very large. Nevertheless, to analyse imaging Cherenkov data we need to know the response of the telescopes in a variety of conditions, so the use of simulated gamma-ray showers becomes necessary.

To cover the different performance of the telescopes depending on the energy of the primary gamma-ray, its incoming direction and the impact point of the EAS on the ground, numerous samples are generated. The samples are created randomly within some parameter ranges so as to adequately cover these diverse scenarios, in a method known as MC simulation. The simulated gamma-ray events are then used to optimize the algorithm aimed at identifying the real gamma-ray events in observation data and to estimate their energy and direction. They are used to compute the probability of a given gamma-ray event to survive the trigger system and the analysis cuts. This, in turn, allows us to calculate the effective collection area of the telescopes and, therefore, be able to infer the flux of gamma-rays of an observed source.

The MC simulations used by MAGIC (Majumdar et al. 2005) consist of multiple stages. First, the EAS is simulated with some initial parameters such as the primary particle species, the energy of the particle, its incoming direction, etc. Secondly, the atmospheric absorption and scattering of the Cherenkov photons from the EAS is simulated, along with the response of the mirrors and the reflection of the photons onto the camera plane. Thirdly, the response of the camera, the readout electronics and the triggers are simulated for the distribution of photons arriving at the camera plane. After this process, the simulated events have almost the same format as the real observation data and can be processed by the same the analysis chain.

As stated before, a large amount of events must be generated with different configurations of primary gamma-ray energy, incoming direction and impact position on the ground to provide a homogeneous coverage of the response of the telescopes. Since the simulations are computationally expensive, their production is standardized and centralized within the MAGIC collaboration. The standard MC productions of MAGIC are defined by three key parameters:

- **Pointing direction:** The response of the telescopes varies with Zd due to the difference in energy threshold and collection area. Consequently, the standard MC productions are generated with a flat distribution in $\cos(\mathrm{Zd})$ in different Zd ranges: low (5° - 35°), medium (35° - 50°), high (50° - 62°) and very high (62° - 70°).
- **Incoming direction:** Standard MAGIC observations are performed in wobble mode with an offset of 0.4°, so the gamma-rays are simulated in a ring with the same offset from the camera centre (*ringwobble* simulations). These are the simulations used in the analysis of point-like sources. Alternatively, the analysis of gamma-rays from an unknown direction requires the evaluation of the telescope response with respect to any location in the FoV. For those situations, gamma-rays are simulated with a uniform distribution covering a circle of 1.5° or 2.5° radius (*diffuse* simulations). Figure 3.5 shows the distributions of the projection of the arrival directions for both types of simulated events on the camera.
- **Energy:** The energy range covered by the simulated gamma-rays must coincide with that of possible detection in MAGIC, for each Zd considered. It goes from $10\,\mathrm{GeV}$ to $30\,\mathrm{TeV}$ in the low and medium Zd ranges. The spectrum of simulated events follows a power-law distribution with

a spectral index of -1.6. This is determined by the trade-off between the low trigger rate at the lowest energy range, the significant computational demands at the highest energy range and the broad energy span that is covered.

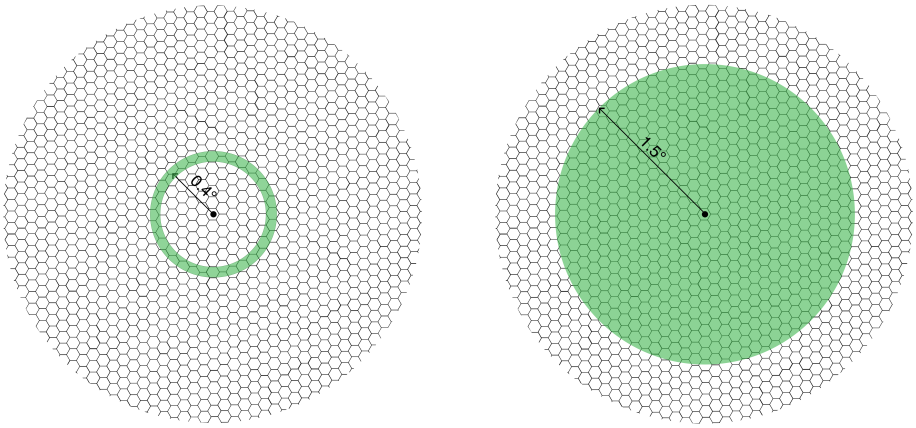

Figure 3.5: Incoming direction distributions of the MC simulated gamma-rays in the *ringwobble* scheme (**left**) and the *diffuse* scheme (**right**).

The standard MC productions for the different parameters are contained within production periods. A MC production period refers to specific versions of standard productions within the simulation process. These periods are defined whenever there is a major hardware intervention or a significant change in performance due to factors like weather conditions or minor hardware maintenance. The purpose of defining these periods is to ensure that the simulations accurately reproduce the real response of the telescopes. The standard MC simulations played a big role in the development of this work. The treatment and use of their simulated gamma-rays within the archival search framework are further explained in the next chapter.

3.3.6 Event reconstruction

The last step in the characterization of the shower event is the computation of its three main properties: the particle species, its incoming direction and its energy. Most of the images that survive up to this stage are still originated by hadronic showers even in observations of strong gamma-ray sources like the Crab Nebula. The identification of the primary particle allows the reduction of this background.

3.3.6.1 Gamma/hadron separation

The discrimination of events into gamma-ray or CR originated is referred to as gamma/hadron separation. This process relies on a multi-dimensional classification algorithm based on binary decision trees, the so-called Random Forest (RF) (Albert et al. 2008a). In order to train the RF to distinguish between gamma and hadronic images, it is given two inputs: a sample of MC simulated gamma-rays and a sample of real background data (events from a region of the sky without known gamma-ray sources). Both samples need to have similar observational conditions to those of the data we intend to analyse, that is, same Zd range, moonlight and weather conditions. The MC sample used to train the RF has to be different than the one used to calculate the collection area of the telescopes and the energy migration matrix, so the standard production is divided into a *train* subsample and a *test* subsample.

The training process starts with all the training events in a single node, with hadrons tagged as 1 and gammas tagged as 0. In each node, a randomly selected Hillas parameter from the events is used to discriminate between the gamma and hadron-enriched subsets, splitting the sample in two branches, iteratively. A cut value for that parameter is chosen, so that it minimizes the Gini (1921) index

$$Q_{\text{Gini}} = 4\frac{N_\gamma N_h}{(N_\gamma + N_h)^2}\,, \tag{3.1}$$

where N_γ is the number of gamma-ray events and N_h is the number of CR/hadronic events. A sample with equal number of events in each class would give an index of 1, whereas a sample with only one class would give a 0. The splitting of a branch stops when the Gini index is 0, or when it contains less than 5 events (Albert et al. 2008b). A *hadronness* estimator, had is assigned to the last branch to show its final hadron content, $had = N_h/N$.

The trained RF, containing around 100 decision trees, is then applied to the data under investigation. Each real event passes through the previously trained trees for its classification, getting a *hadronness* score in all the them. The final had is the average of the scores achieved in all the trees, and goes from 0, most "gamma-like", to 1, most "hadron-like". An example of the different *hadronness* distributions of real CR events and simulated gamma-ray events can be seen in fig. 3.6.

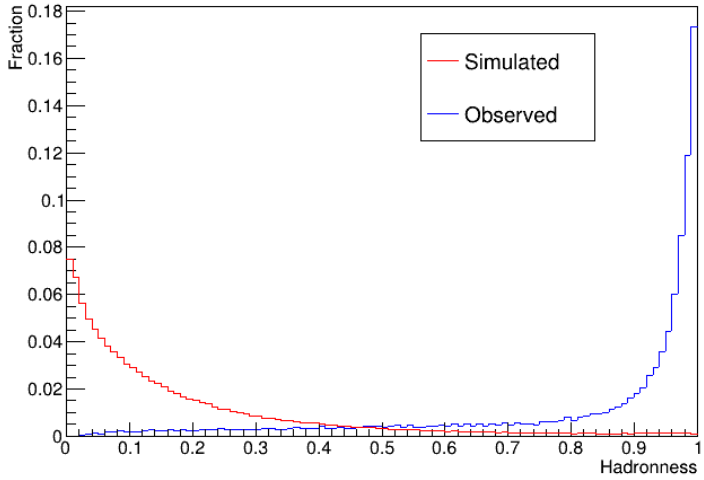

Figure 3.6: Distribution of the *hadronness* parameter of simulated events from a standard MC production and of observed events from a background region. Even the representative samples for gamma-ray and CR events have a continuous distribution in this parameter.

3.3.6.2 Arrival direction reconstruction

The crossing point method described in section 3.3.3 can fail for low energy events or very large impact parameters, which result in approximately parallel images. The precision of this method can, however, be improved by taking into account the timing information and shape of the events. Based on that premise, Lessard et al. (2001) developed the *disp* method to reconstruct the arrival direction of an event with a single telescope. In it, *disp* is the distance between the CoG of the ellipse and the estimated arrival direction of the shower, which is supposed to lie somewhere on the line defined by the major axis of the Hillas ellipse. The method suffers from the so-called head-tail ambiguity, since it only provides a distance and not a direction (see fig. 3.7). Luckily, the skewness of the light distribution can be used to break the ambiguity.

The standard MAGIC analysis performs the arrival direction reconstruction of the incoming gamma-rays with a *Disp RF* method (Fomin et al. 1994 and Lessard et al. 2001). In this method, the *disp* parameter is estimated for each image in both telescopes with a RF (instead of the Gini index, the variation of *disp* between nodes is minimized) using simulated gamma-rays with known incoming direction and *disp*. Two possible arrival directions are therefore estimated

for each telescope, as shown in fig. 3.7, with 1A and 1B for M-I and 2A and 2B for M-II. The direction of the primary gamma-ray lies in the smallest possible segment created between those estimated points. If the length of that segment is larger than $0.22°$, the event is rejected, increasing the rejection power of background events. In the opposite case, the estimated arrival direction of the event is taken as the average of the couple of selected points, weighted with the number of pixels in each image.

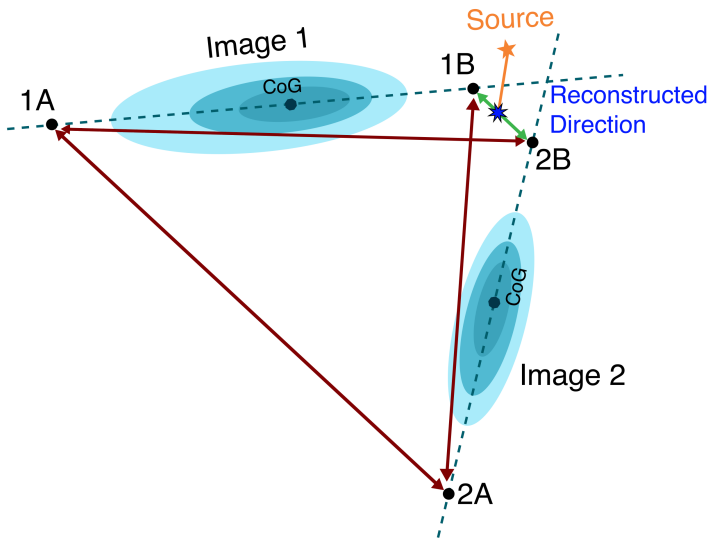

Figure 3.7: Diagram of the stereo *disp* method for arrival direction reconstruction. The black dots indicate the possible arrival directions estimated by the *disp RF* for each telescope (**1A,1B,2A,2B**) and the double pointed arrows indicate the distances between them. The smallest of which (**green line**) is used to compute the reconstructed direction of the event. The blue dashed lines indicate the axes of the showers and the different shades of blue in the ellipses indicate the light distribution.

3.3.6.3 Energy estimation

The energy of the events is estimated with a Look-Up Table (LUT) created also with MC simulated gamma-rays. A two-dimensional table is produced for each telescope separately and they are binned in image *size* as $\sqrt{\log(size)}$ and in the ratio of impact parameter and Cherenkov radius, $\frac{I}{R_C}$, where I is the distance from the telescope to the impact point of the event. Bins are filled with the

mean and Root Mean Square (RMS) of the distribution of true energy and scaled with the Cherenkov density and size ratio, $E_{\mathrm{true}}\rho_{\mathrm{C}}/size$ (Aleksic et al. 2012). Once we have the tables, the estimated energy and uncertainty of an event is obtained by "looking up" the image parameters of that event in the M-I and M-II tables. The final stereo estimated energy E_{est} is the average of the energy value returned by each table weighted with the inverse of their uncertainty[5].

3.3.7 Instrument response function

Up to this point, the data processing has been focused on the individual air shower events and their characteristics. However, to obtain scientific results, the observed events must be combined to investigate global features like their energy distribution or flux variations over time.

In astrophysics and astronomy, the intention behind observing any source is, most commonly, to investigate its flux, $\Phi(E,t)$. In the context of IACTs, a differential flux is typically measured, that is, the number of events per unit energy, area, and time, and it is usually given in $\mathrm{TeV}^{-1}\mathrm{cm}^{-2}\mathrm{s}^{-1}$. The true flux emitted by a source is convoluted with the instrument response R of the telescopes, i. e., a particle with true energy E and arrival direction $\boldsymbol{p}$ is measured with an estimated energy $\hat{E}$ and direction $\hat{\boldsymbol{p}}$ or may not even be detected at all.

The probability distribution for the estimated direction and energy of the particle depends on the true characteristics of the particle and on the characteristics of the telescopes. The number of events N detected from a gamma-ray source with flux $\Phi(E,\boldsymbol{p},t)$ is given by

$$\begin{aligned} &N(\Delta\hat{E},\hat{\boldsymbol{p}}) = \\ &\int_{t_0}^{t_1} dt \int_{\Omega} d\hat{\boldsymbol{p}} \int_{\Delta\hat{E}} d\hat{E} \int_{0}^{\infty} dE d\boldsymbol{p} \frac{d\Phi(E,\boldsymbol{p},t)}{dE d\boldsymbol{p}} R(\hat{E},\hat{\boldsymbol{p}}|E,\boldsymbol{p},t) \\ &\quad + b(\Delta\hat{E},\hat{\boldsymbol{p}})\,, \end{aligned} \tag{3.2}$$

where t_0 and t_1 are the start and finish times of the observation[6], $\Delta\hat{E}$ is the

[5] Some corrections are applied to each energy bin to take into account the $\cos(\mathrm{Zd})$ dependence, the angle between the shower axis and the geomagnetic field and the leakage of the image.

[6] The estimator for the time of arrival of the particle has a much better precision than the temporal effects we want to investigate, so we can assume that its PDF is a delta function and $\hat{t} \equiv t$.

range of estimated energies, Ω is the integrated solid angle and b is the number of events from the irreducible background that is observed together with the signal.

The instrument response function $R(\hat{E}, \hat{\boldsymbol{p}}|E, \boldsymbol{p}, t)$[7] can be factorized into several components that characterize the relation between the estimated energy and position of the events to their true ones. These components are estimated with MC events, which are the only ones for which their true E and $\boldsymbol{p}$ are known. Assuming no correlation between the energy and position estimators, R can be factorized into:

- Point Spread Function (PSF): $f_{\boldsymbol{p}}(\hat{\boldsymbol{p}}|E, \boldsymbol{p})$ is the 2-dimensional Probability Density Function (PDF) of the direction estimator and can be approximated by the spatial distribution of photons emitted by a point source. A Gaussian function can be used, and its standard deviation σ_{PSF} is also referred to as the angular resolution of the instrument. To report the PSF, a containment radius is defined. This is the maximum distance between the true and estimated positions that contains a set percentage of events (68 % when using a Gaussian distribution (Aleksić et al. 2015b)).

- Energy dispersion: $f_E(\hat{E}|E, \boldsymbol{p})$ is the PDF for the energy estimator. It contains the probability of a particle with energy E to be reconstructed with energy $\hat{E}$.

- Effective Area: $A_{\mathrm{eff}}(E, \boldsymbol{p})$ is the instrument collection area corrected by the gamma-ray detection efficiency of the instrument, which varies with the analysis cuts. It is calculated as

$$A_{\mathrm{eff}}(E, \boldsymbol{p}) = \frac{N_{\mathrm{MC,final}}(E, \boldsymbol{p})}{N_{\mathrm{MC,total}}(E, \boldsymbol{p})} \pi I_{\mathrm{max}}^2 \,, \tag{3.3}$$

  where $N_{\mathrm{MC,final}}$ is the number of events that survive the analysis cuts, $N_{\mathrm{MC,total}}$ is the total number of simulated events and I_{max} is the maximum impact parameter of the simulated events.

The functions listed above describe the response of the instrument at any point in the FoV, so they are valid for observing sources at unknown positions. Their $\boldsymbol{p}$ dependence can be expressed in camera coordinates or as an offset from

[7] R depends on more parameters, like the *hadronness* of the events or the Zd of the observation, which are taken into account by calculating it using the same cuts as the analysed data.

the centre of the FoV if the detection efficiency of the telescopes is assumed to be symmetric, which is the case in standard MAGIC analysis. Such assumption is not correct in the context of this work, where we look for transient gamma-ray signals at any location in the FoV. It can be inferred from the unaddressed time dependence of $R(\hat{E}, \hat{\boldsymbol{p}}|E, \boldsymbol{p}, t)$, that the response of the MAGIC telescopes is not fully described from the functions listed above. Indeed, all of them are obtained from gamma-ray events of MC simulations, which are generated with a set of parameters that may differ from the particular conditions of an observation at a given time t, such as the atmospheric transmission, the NSB level, the temperature of the electronics, etc. Consequently, we can't naively obtain the flux of a source by simply inverting the product of the instrument response functions, $R(\hat{E}, \hat{\boldsymbol{p}}|E, \boldsymbol{p}) = f_{\boldsymbol{p}}(\hat{\boldsymbol{p}}|E, \boldsymbol{p}) \cdot f_E(\hat{E}|E, \boldsymbol{p}) \cdot A_{\text{eff}}(E, \boldsymbol{p})$, we need to have a sample of background counts with (ideally) the same $\hat{\boldsymbol{p}}$ and t distributions as $N(\Delta\hat{E}, \hat{\boldsymbol{p}})$ to account for these differences.

3.3.8 Significance and higher scientific products

In a standard IACT analysis, the first step after obtaining all the relevant information about the observed showers is to evaluate whether a gamma-ray signal is significantly detected in the data. Even after applying cuts (*hadronness*, *size*, incoming direction, etc.) on the data, many background events still survive. The confirmation of gamma-ray emission from the target requires the comparison between the events from the region where the signal is expected, the ON region, and the events from the purely background populated OFF regions. For visualization, events are distributed in the so-called θ^2 plot as a function of their squared angular distance to the position of the source or the OFF central point, respectively.

The ON region is considered to contain a number of background events plus an excess due to the real gamma-ray signal. The number of this excess events is computed by maximizing a likelihood function that contains the number of events in each region as described in (Li et al. 1983). An example of clear gamma-ray excess can be seen in fig. 3.8, where the θ^2 plot of an observation of the Crab Nebula is shown.

In the following steps, the instrument response functions are used to obtain higher level scientific products such as the flux, light curve and spectrum of the source. These results can provide an insight into the physical processes that produce such energetic radiation or into the characteristics of the observed

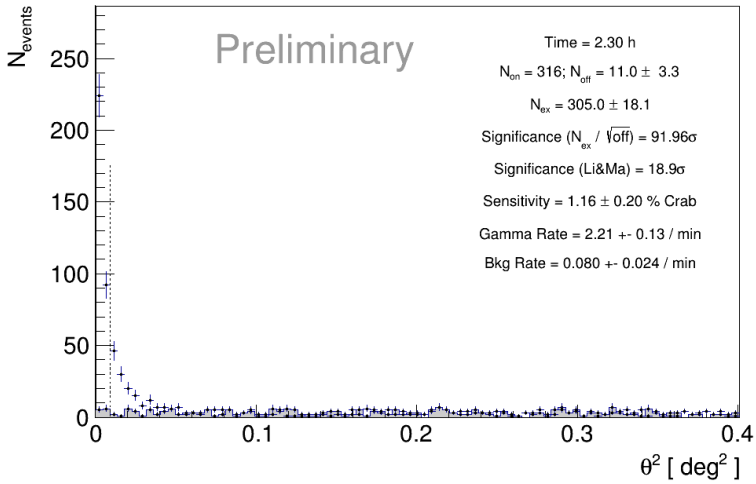

Figure 3.8: ON and OFF θ^2 event distributions for an observation of the Crab Nebula. The significance of the signal is computed in the region to the left of the vertical dotted line.

source.

The work performed for this thesis branches out from the standard procedure at this point, so the reader is redirected to Fernandez Barral (2018) and Ishio (2020) for in-depth descriptions on the computing of the standard IACT scientific products (i.e. spectral energy distribution, flux points, light curve, etc.). Particularly, the definition of light curve used in this work differs from the standard one, as the latter represents the evolution of the flux of a source as a function of time and is usually expressed in $\mathrm{cm}^{-2}\mathrm{s}^{-1}$. Here, light curves denote the changes in the rate of detection of gamma-like events as a function of time and are expressed in $\mathrm{events/s}$. In the following sections, we describe the alternative analysis method used for the search of transient gamma-ray signals in archival data and the specific software tools developed for it.

Chapter 4

Search method for VHE transients

The goal of this chapter is to describe and characterize a new method to perform a full-FoV, unbiased search for VHE transients in MAGIC's data with a specific interest in PBH evaporation signals.

Most commonly, MAGIC's observations are target based, and the analysis of the collected EAS information is restricted to a few small sky regions in the FoV of the telescopes (see section 3.3). The motivation behind this work is the desire to leverage all the information contained in hundreds of thousands of hours of observations stored in MAGIC's archives through the years. Furthermore, the method could be extended to perform an online monitoring of the sky and provide alerts for the astronomical community.

For an unbiased search, our transient search algorithm divides the sky in overlapping areas (denoted as "cells" from now on) with fixed coordinates and size, and cross-checks the FoV of the given observation against them. Gamma-like events with reconstructed directions within a cell are associated to this cell and a light curve of the changing rate of events is created. This is repeated for all the available observations, thus constructing light curves for all the sky seen by MAGIC with independence of the original observation characteristics.

Cells that correspond to known TeV sources are excluded from the analysis to limit the possible significant detections to those from transient signals. After that, the gamma-like events in the light curves are divided into fixed-width time windows with a certain overlap. At each cell and time window, the number of events observed is tested against the hypothesis that they originate from

background EAS only. In this scenario, a strong upward deviation from the estimated background level is interpreted as a transient gamma-ray signal candidate.

The design of the search allows us to explore sky regions that had not been previously considered, opening a window to a variety of analysis and discoveries. However, the non-specific nature of the algorithm and the vast amount of data used in the search forbids us from attempting to fit a light curve profile in each search case, so we use a fixed-width window. Different transient phenomena can be searched for by applying the algorithm in a variety of time window widths or by selecting a specific width when their emission timescale is known.

The following sections in this chapter describe the design and implementation of the search method, the developing and testing of the background model, the management of statistical uncertainties and the trials correction for the different search timescales used in our analysis.

4.1 Spatial search

The spatial search of VHE signals is performed on a set of circular cells centered at a fixed grid of equatorial coordinates (R.A./Declination (Dec)). Each point of the grid corresponds to the centre of a cell . The gamma-like events of a given observation are divided into cells depending on their reconstructed arrival directions. If their direction is within a fixed distance to a cell centre, the number of that cell is added to the rest of characteristics of the event. Using a circular area for the search instead of a rectangular one allows us to use the angular resolution of the instrument as the radius of the cells.

The possible issue of having areas of the sky unmapped due to the geometry of the cells is solved by selecting a grid where the distance between points is smaller than the radius of the cells. This creates an overlap in the cells, which has two effects: first, it creates correlation among the results for neighbouring cells, which needs to be taken into account when considering the number of independent trials to correct for the significance of a potential signal and second, the overlap results in a better resolution in the origin of the possible signal, e.g., if a signal is detected in two neighbouring cells we can assume that its origin lies in the overlapping area of the cells, which is smaller than the area of the individual cells.

The angular resolution of the MAGIC telescopes depends on the energy of the events and on the Zd of the observation. As previously mentioned in chapter 3 and seen in fig. 4.1, the angular resolution becomes better when events have a higher estimated energy and it becomes slightly worse for observations with higher Zd. The reason behind this is that the images produced by high energy EAS are larger and can be better reconstructed, while the ones recorded at higher Zd can be attenuated by the atmosphere or cropped in the camera plane.

This project evaluates archival data in a wide range of Zds ($5°$ to $50°$) and energies (70 GeV to 10 TeV). Therefore, we chose the radius of the search cells, r_S, to be the mean value of the angular resolution of low and medium Zd at low energies, that is, $r_S = 0.15°$. However, r_S can be modified to increase the significance of the results in searches for signals at higher energies or different Zd ranges.

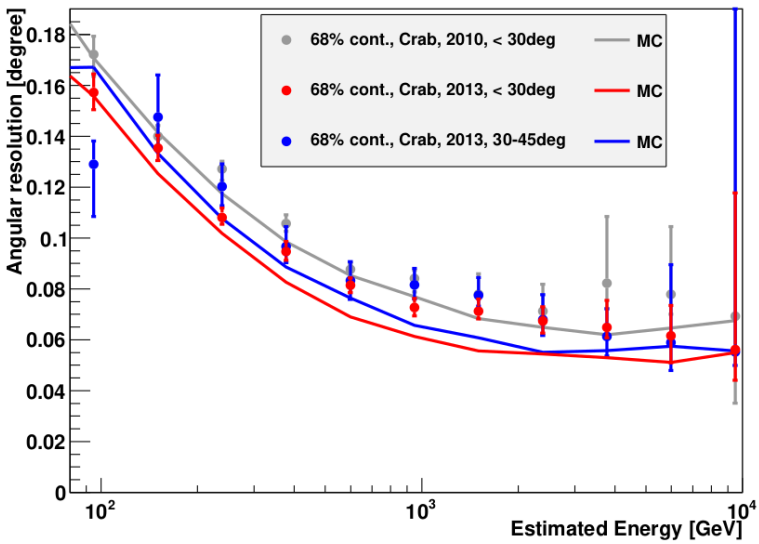

Figure 4.1: Angular resolution of the MAGIC telescopes as a function of the estimated energy of the detected particles, obtained as the 68 % containment radius. Points correspond to resolutions obtained with a Crab Nebula data sample and the solid lines correspond to MC simulations. Red points: low zenith angle sample, blue points: medium zenith angle sample. The angular resolution before the camera upgrade is shown in grey. Figure extracted from Aleksić et al. (2015b).

The grid used in the algorithm would ideally be a regular one, with evenly

spaced coordinates that had the same distance between any two neighbouring centres. Unfortunately, a sphere cannot be covered by evenly spaced points unless the number of points is 4, 6, 8, 12 or 20. For that reason, we are using **HEALPix**[1] (Górski et al. 2005), an algorithm for the pixelisation of the spherical surface (see fig. 4.2.). This algorithm was originally created for satellite missions that measured the Cosmic Microwave Background (CMB) anisotropy (Górski et al. 2005).

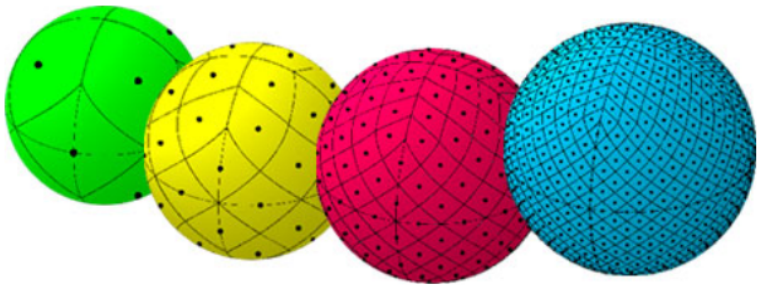

Figure 4.2: Example of the **HEALPix** partitioning of a sphere at progressively higher resolutions. The green sphere has the lowest resolution possible in the algorithm, with 12 equal sized pixels. The yellow sphere has a **HEALPix** grid of 48 pixels, the red one of 192 pixels, and the blue one has a grid of 768 pixels, corresponding to a $\sim 7.3^\circ$ resolution. Figure from NASA, https://healpix.jpl.nasa.gov/.

HEALPix allows us to select the grid characteristics so that the spherical surface is covered by the cells of the chosen radius with the appropriate level of overlap among them. The parameter in **HEALPix** that sets the number of divisions on the sphere and thus the closeness of the grid points is *NSIDE*. The *NSIDE* used in this project is 256, which creates a grid of 786 432 pixels. Each pixel covers an area of roughly $0.05246^{\circ 2}$, providing a mean overlap of 20% for the required area of the cells.

Two example pixelations, one with $NSIDE = 10$ and one with the pixelation used for the search algorithm are shown in fig. 4.3. If we use an even finer grid (one that contains a larger number of pixels, more tightly placed), we can show the overlap created for this analysis and simulate the correlation between the results of each trial, as we will see in section 6.1.

[1] An acronym for Hierarchical Equal Area isoLatitude Pixelization of a sphere. In this work we used the *HealPy* Python package that bundles the **HEALPix** C++ libraries (Zonca et al. 2019). http://healpix.sourceforge.net.

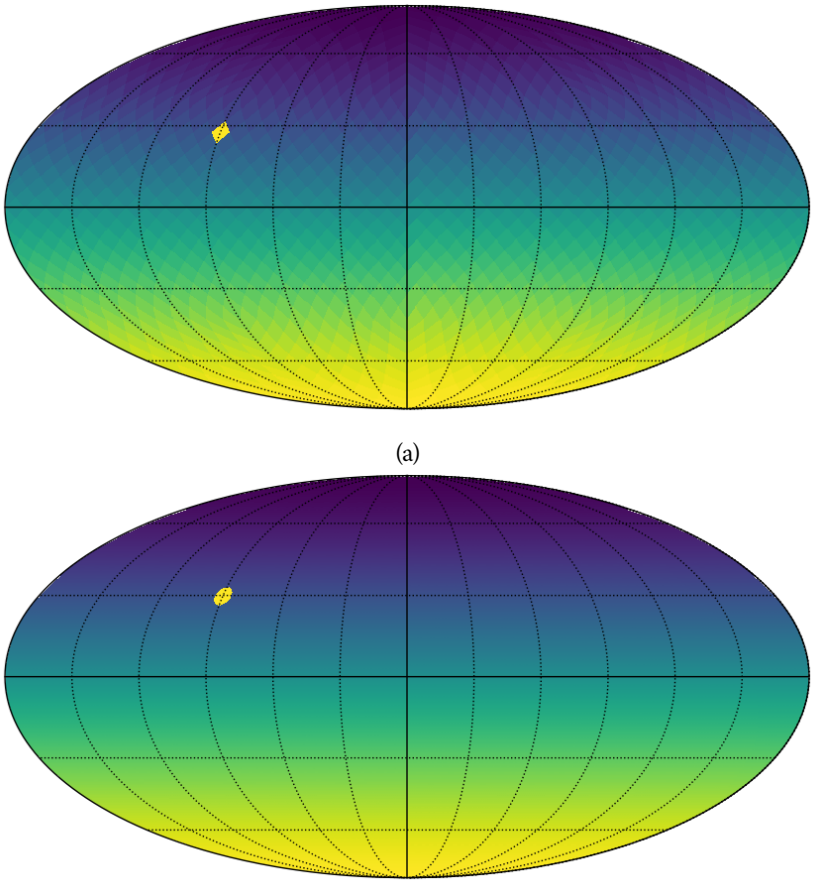

(a)

(b)

Figure 4.3: Mollveide projection of the **HEALPix** pixelisation of the sphere for two grids: (a) Example wide grid with 1200 pixels, (b) The finer grid used in this project, with 786432 pixels. The yellow patch in both figures corresponds to a selection of pixels around $3.5°$ of the equatorial coordinates R.A. $= 22.92\text{h}$ and Dec $= 16.146°$.

In fig. 4.4, a small diagram of a zoomed-up region of the search is shown, with the areas covered by the spatial cells and how they overlap for the selected grid characteristics. To show the overlap within **HEALPix**, our grid of *NSIDE* $= 256$ is used to find the pixels of a larger grid of *NSIDE* $= 9000$ that correspond to the centres of the cells. Each small pixel around the centre, up to the radius of a cell, has its content raised by 1 count.

A similar approach will be used in section 6.1 to simulate correlation, and in chapter 7 to estimate the effective volume probed in the search for PBH

evaporation.

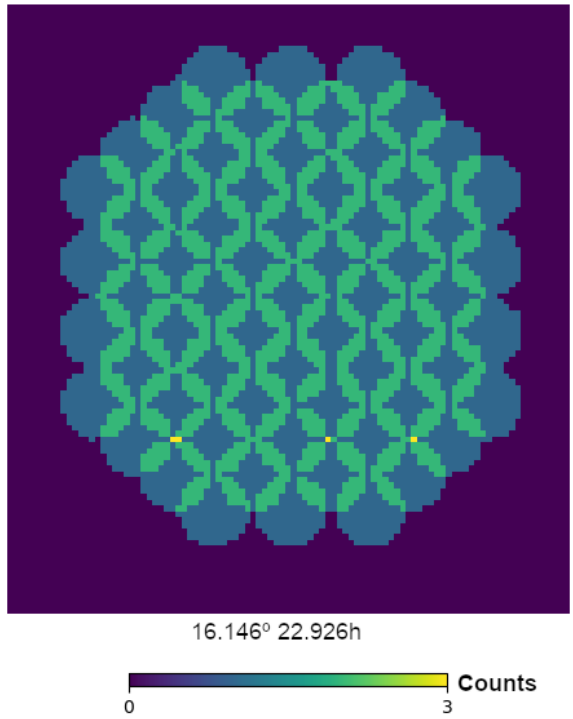

Figure 4.4: Gnomonic projection of a section of the grid with search cells of radius $0.15°$ centered around the equatorial coordinates R.A. $= 22.92$h and Dec $= 16.146°$. The number of counts denotes how many cells cover a given area or position in the sky. Only a small number of cells are portrayed, surrounded by 0 counts regions due to the computer memory requirements needed to show the overlapping regions within **HEALPix**.

Since we are using archival data, we need to incorporate some safety measures to prevent strong gamma-ray signals from known sources from contaminating our analysis and appearing in the results. To do so, we downloaded the coordinates and morphology information of all **TevCat** sources (*TevCat Online Catalog*) and applied an exclusion zone around them to remove any cell that was too close to a known source.

Originally, this exclusion zone had a radius equal to the standard cut for low-energy analysis in MAGIC, $\theta^2 = 0.02^{\circ 2}$. However, when applying the search algorithm to the whole dataset of approximately one year of observations, the implemented alert system would be filled with signal detections. When examined, these signals corresponded to cells in the vicinity of a known

source (and were adjacent to already excluded cells), so the radius of the exclusion zone was increased to $0.2°$. For extended sources, we manually removed any grid points within a distance equal to their major axis. This reduced grid allows us to perform the transient search without signal contamination from known sources.

Furthermore, to lower the number of cells that the software has to iterate over, we checked MAGICs visibility and removed the cells with coordinates not available for MAGIC observations, such as most of the southern hemisphere. The final number of cells exported from **HEALPix** is equal to $588\,080$. The implementation of this grid in the search algorithm is described further in the next sections.

4.2 Temporal search

Once the gamma-like events from a cell are selected we can construct the light curve of that cell and divide it into fixed width time windows to search for a transient signal in each of them.

We have found the best range for the time window width to be between $1\,\mathrm{s}$ and $1200\,\mathrm{s}$. Time windows smaller than $1\,\mathrm{s}$ have a very low mean number of observed events after cuts (< 1) and were not explored in this work due to increased uncertainties in background estimation and technical application issues.

On the opposite side of the range, $1200\,\mathrm{s}$ corresponds to the usual length of a run in MAGIC observations. The expected duration of the transient signals that we aim to detect is shorter than the standard MAGIC run. Therefore, we chose to run the search algorithm in four different time windows within this range, $2\,\mathrm{s}$, $10\,\mathrm{s}$, $100\,\mathrm{s}$ and $1000\,\mathrm{s}$. The $2\,\mathrm{s}$ time window can be used to simultaneously search for PBH evaporation and short GRBs.

If we wanted to use a longer time window, we would have to take into account the deadtime in between runs due to the repointing of the telescopes (WOBBLE mode) or the stop in the DAQ and technical runs (ON mode) before data-taking. This could be an interesting extension of this work and be used to, for example, monitor sources such as AGNs during long periods of time and check for quiescent and flaring states. The extension of the search algorithm to work with longer time windows was attempted during the development of

this work. However, the correct interpolation of the light curves through empty bins caused by any type of operation halting was found to require a dedicated study that is beyond the scope of this work.

In the application of the time windows, we can choose a level of overlap in time to lessen the chance of a signal being detected in the middle of two windows to get lost in the analysis. Since we don't fit the temporal profile of the different transients to the data, we chose to apply a simple 50% overlap for the time windows to balance the possible signal loss with the increase in the number of trials. In contrast, the $1000\,\mathrm{s}$ analysis is left with no overlap in the time windows, since the length of the observation runs would require an overlap of $\sim 80\%$ that does not provide an increase in sensitivity.

The existence of gaps (empty bins due to periods of no data-taking) in the observed light curves forbids us from naively dividing them into whatever number of time windows can fit in them between the start and the end of the observation. We have to provide a list of good observation timestamps to ensure that the number of events seen in a window is not lowered by periods in the light curve where the telescopes were not taking data.

To apply the time window division of the light curves, we have to first divide the light curves into their corresponding runs and gaps between runs and any other gaps in the data. Since the window widths are fixed but the lengths of the good observation times are heterogeneous, the last few seconds of a run may be discarded so that an integer number of windows can fit. Ultimately, for every spatial cell and time window, the number of observed counts is compared against the expected background for that position and time.

Chapter 5

Estimated background model

In a blind search, finding a signal from a PBH evaporation, a GRB, another transient phenomena, or any other gamma-ray source comes down to the ability of discerning a characteristic in the data that is not compatible with the known background characteristics. In this work, what we look for is an excess amount of gamma-ray events arriving together within a predefined time duration and with similar directions (within a sky cell). The gamma-hadron separation cut applied in our analysis reduces the number of CR air showers contributing to the background of our search but it does not result in the complete elimination of background events. In the data investigated for this analysis, after applying the background rejection cuts (listed in table table 5.1) , the average background rates of the whole camera are found to be $3.44\,\mathrm{events/s}$ for galactic FoVs and $2.58\,\mathrm{events/s}$ for extragalactic FoVs.

In the standard analysis for point-like sources, the number of background events is estimated from dedicated observations or regions of the FoV where no gamma-ray source is expected, as seen in section 3.3.8. Since we are investigating all the FoV and want to use all available data, we can't use either of those approaches. The following discussion describes the development of a model to estimate the gamma-like background rate for the cells in our search as a function of time.

In section 3.3.7 we saw how the number of detected events depends on the instrument's response and on the flux of the observed source. The same can be said for observations with no gamma-ray source, where only events from background EAS that survived the analysis cuts are detected. Therefore, the number

Parameter	Cut values
Hadronness	< 0.3
$0° \leq \mathrm{Zd} < 35°$	
$\hat{E}$	$> 70\,\mathrm{GeV}$ and $< 10\,\mathrm{TeV}$
$35° \leq \mathrm{Zd} < 50°$	
$\hat{E}$	$> 200\,\mathrm{GeV}$ and $< 10\,\mathrm{TeV}$

Table 5.1: Parameter cuts used in the creation of the background estimation model and in the analysis of the observational data for the transient search. The *hadronness* cut is the same for low and medium Zd observations, while the cuts on the estimated energy, $\hat{E}$, depend on the range of Zd.

of background counts detected in a cell c, assuming a constant background flux $\Phi(E, \boldsymbol{p})$ is

$$b_{\mathrm{c},i} = \int_{t_0}^{t_1} dt \int_{\Omega_\mathrm{c}(t)} d\hat{p} \int_{\Delta\hat{E}} d\hat{E} \int_0^\infty dE d\boldsymbol{p} \frac{d\Phi(E,\boldsymbol{p})}{dE d\boldsymbol{p}} R_i(\hat{E}, \hat{\boldsymbol{p}} | E, \boldsymbol{p}, t)\,, \quad (5.1)$$

with $\Omega_\mathrm{c}(t)$ the projection of the cell in the camera at time t and R_i the instrument response for each particle i that contributes to the gamma-like background (protons, He nucleii, electrons, etc.). To obtain b_c we would have to integrate over all the i contributions, but, as discussed in section 3.3.7, we don't fully know R_i.

What we can know, on the other hand, is the total rate of events detected at time t in the FoV after applying the analysis cuts, $R_\mathrm{T}(t)$. If no VHE sources are in the FoV, we can use the fact that the solid angle of a cell is very small compared to the solid angle of the whole FoV to divide eq. (5.1) into a contribution from $R_\mathrm{T}(t)$ and from the relative efficiency of the instrument at different $\hat{\boldsymbol{p}}$:

$$b_\mathrm{c} = \int_{t_0}^{t_1} dt R_\mathrm{T}(t) \int_{\Omega_\mathrm{c}(t)} d\hat{\boldsymbol{p}} A(\hat{\boldsymbol{p}})\,. \quad (5.2)$$

$A(\hat{\boldsymbol{p}})$ is the relative camera acceptance, which determines the probability of detecting a gamma-ray candidate (or indistinguishable, irreducible background) with certain reconstructed arrival direction $\hat{\boldsymbol{p}}$, in the camera reference frame. $A(\hat{\boldsymbol{p}})$ integrates the whole energy range and depends on the azimuth angle and

Zd of the observation.

In this section, we first obtain $A(\hat{\boldsymbol{p}})$ by accumulating events from different observations where no gamma-ray signal was detected, the so-called OFF sources or OFF observations, and then we adapt the process so that we can obtain $A(\Delta\hat{E}, \hat{\boldsymbol{p}}|E, \boldsymbol{p})$ from MC simulated events.

5.1 Camera acceptance characterization

Following the procedure of Da Vela et al. (2018) and using the same OFF sources used in their paper, we evaluate the relative camera acceptance $A(\hat{\boldsymbol{p}})$ by filling a two-dimensional histogram with the reconstructed directions $\hat{\boldsymbol{p}}$ (in camera coordinates) of the background events that pass the signal selection cuts (*hadronness*, Zd, energy, angular distance to the centre of the FoV) used in the analysis and normalizing it to 1 (see fig. 5.1), thus creating a camera "map" of the relative acceptance of the instrument. This acceptance map is effectively a matrix $\boldsymbol{A}$ where each element is the bin content of the histogram.

When using a single telescope, the camera acceptance is, at first order, symmetric with respect to its centre and can be modelled by a function of the angular offset from the centre. For MAGIC, this function peaks at offset 0 and rapidly descends toward the edge of the FoV. Hence, events further away from the centre have a higher probability of not being detected. This is in part due to shower images being truncated at the L0 trigger level (see section 3.1.3). Second order asymmetries are caused by large Zd observations and the geomagnetic field. Particularly, the effect of Earth's magnetic field on the charged particles of the cascades creates a preferred direction in the camera acceptance for events with lower energies.

In stereo observations, the camera acceptance becomes the result of the intersection of each telescopes efficiency and the effect of the L3 trigger. The relative orientation of the telescopes optical axes with the axis connecting them changes with the pointing direction. This results in the camera acceptance having an ellipsoidal shape centered in the FoV, which rotates as a function of the azimuth angle. This effect can be taken into account by calculating the relative camera acceptance in bins of azimuth, as portrayed in fig. 5.2.

However, the introduction of too many bins in any variable (azimuth, Zd, energy) can lead to low statistics in certain acceptance maps. A low number

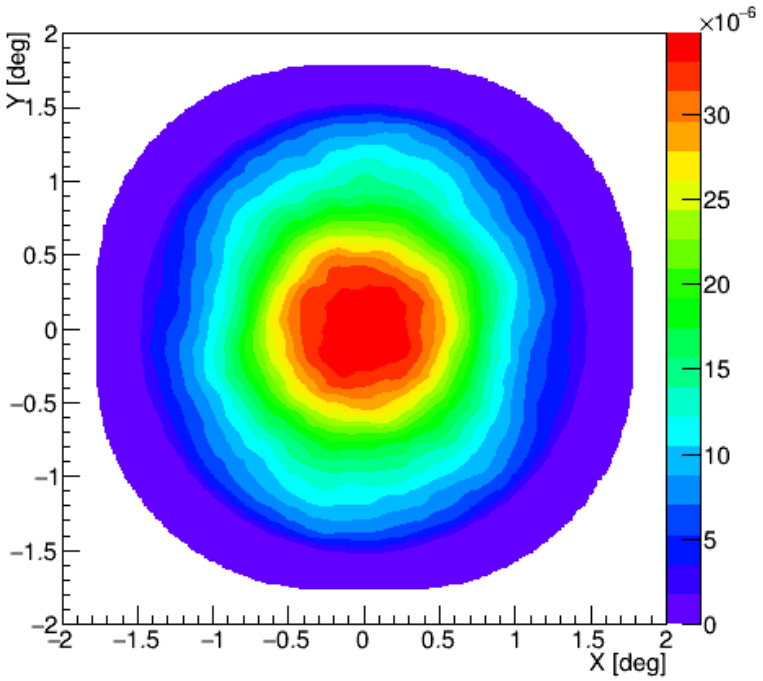

Figure 5.1: MAGIC's relative event acceptance obtained with $14.4\,\mathrm{h}$ of OFF observations of the FoV containing the not detected AGN 3c454.3. The two-dimensional histogram contains the reconstructed directions of the gamma-like events (after gamma-ray selection cuts) of the observation. The Zd range of the observations is $10°$ to $35°$ and the azimuth range is $100°$ to $250°$. The estimated energy cuts applied are in table 5.1. The reference frame is centered in the pointing direction of the telescopes and the X and Y axes correspond to the angular distances in the camera reference frame. The histogram is normalized to 1. A Gaussian smear of 0.046 is used in the histogram for display purposes only.

of azimuth bins is not acceptable as well, since we would be erasing a known dependence of the instrument's acceptance.

From Prandini et al. (2016), we know that an alternative approach can be adopted, where the relative camera acceptance is a continuous function of the azimuth angle. To correct for the effect of this azimuth-dependent rotation of the acceptance maps, the camera coordinates of the reconstructed arrival direction of every event have to be de-rotated by an angle given by

$$\phi_0 = \phi - 120° \,, \tag{5.3}$$

where ϕ is the azimuth angle of the event and ϕ_0 is the de-rotation angle in de-

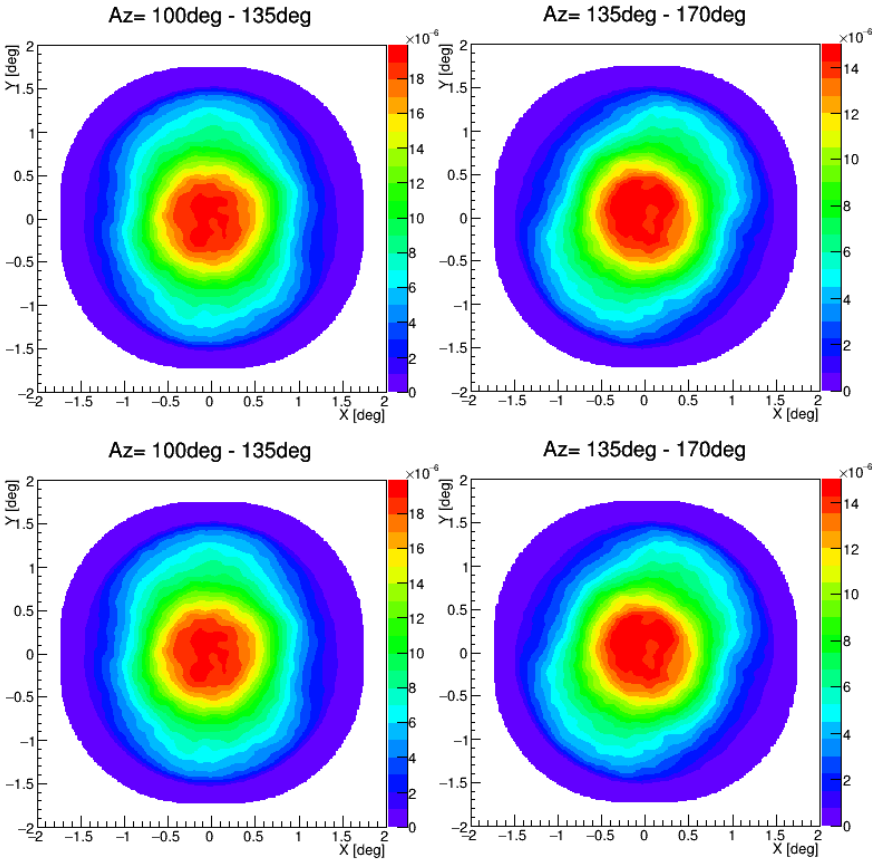

Figure 5.2: MAGIC's relative event acceptance from fig. 5.1 divided in four azimuth bins to show its rotation as a function of the azimuth angle. For more details see the caption in fig. 5.1.

grees (relation obtained from Prandini et al. (2016)). The reconstructed arrival direction of each event in the camera plane, (x, y), is rotated by the angle ϕ_0,

$$\begin{aligned} x' &= x\cos(\phi_0) - y\sin(\phi_0) \\ y' &= x\sin(\phi_0) + y\cos(\phi_0)\,, \end{aligned} \tag{5.4}$$

to obtain a new set of coordinates (x', y') for that event with no azimuth dependence.

Along with the azimuth angle, the relative camera acceptance changes slightly with Zd as a function of $\cos(\mathrm{Zd})$ (Aleksić et al. 2015b). The application of eq. (5.3) and eq. (5.4) allows us to address this weak dependence by simply obtaining the acceptance maps in a few bins of Zd. In fig. 5.3 we show accep-

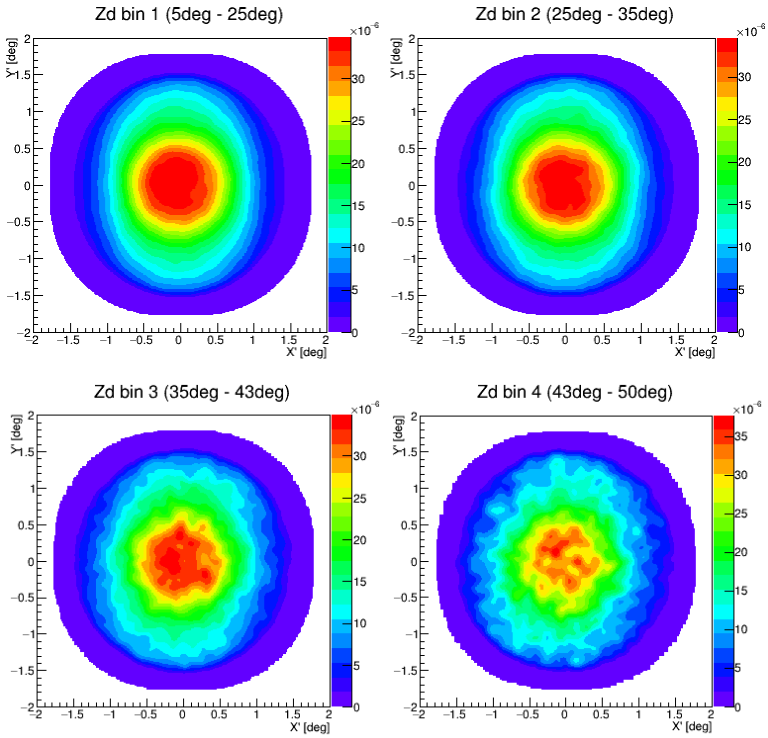

(a) Corrected acceptance maps in four Zd ranges.

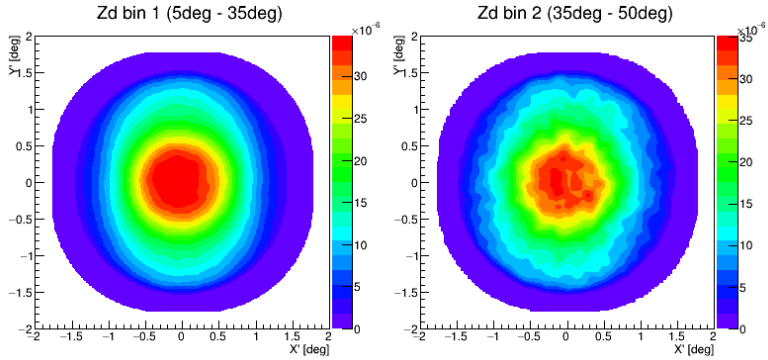

(b) Corrected acceptance maps in two Zd ranges.

Figure 5.3: Acceptance maps (see caption in fig. 5.1) obtained with OFF data after applying the azimuth correction and Zd range cuts. In *a)*, the events are divided into four Zd ranges to create four acceptance maps, while in *b)*, the events are divided into only two Zd ranges.

tance maps obtained by dividing the events into two and four Zd ranges. The acceptance map in the range of $\mathrm{Zd} = 43°$ to $\mathrm{Zd} = 50°$ does not reproduce the expected distribution of events due to the lack of statistics in that range.

This could be fixed by adding more OFF data, from observations in that particular Zd range, to the sample we are using, but this is not always possible as the amount of OFF data we have is finite. For that reason we choose to divide the events into two Zd ranges, $5° < \mathrm{Zd} < 35°$ and $35° \leq \mathrm{Zd} < 50°$ and have two acceptance maps for the search of transient signals.

5.2 Simulated camera acceptance

The acceptance maps described above are the key element on top of which the background model for our search algorithm is built. However, the use of extensive hours of OFF data for their generation, as done by Da Vela et al. (2018), would mean, in our case, a substantial reduction in the observations available for the unbiased search. If we want the maximum amount of data to probe for transient signals we are not able to use any real data in the creation of the acceptance maps. Consequently, we resorted to MC simulated data to create a background estimation model based on MAGIC's relative camera acceptance.

The MC files used in this work for the development of the background model correspond to the *diffuse* - low Zd and the *diffuse* - medium Zd standard productions of period ST.03.03 (see section 3.3.5), which is the one optimized for the observations taken between 2013/07/27 and 2014/06/18 and between 2014/07/05 and 2014/08/05. As per standard practice, both simulated datasets were divided equally using MARS to obtain a *train* sample and a *test* sample. The RF and LUTs necessary to analyse all the observations from this period were already created and validated by MAGIC's DL3 group (Nigro 2019) using the *train* sample. The remaining *test* sample events were used to create the acceptance maps of low and medium Zd and the subsequent background model.

The use of simulations instead of real observations introduces a constraint on the size of the considered FoV for the analysis. Most MC diffuse productions are generated with a FoV of radius $1.5°$, whereas MAGIC's FoV has a diameter of $3.5°$ and thus extends further. To prevent edge effects[1] on the acceptance maps due to the limited extension of the MC simulation, we apply a cut of $1.4°$ on the maximum distance to the camera centre for the reconstructed direction of events. This creates a Region of Interest (RoI) within the FoV of the camera that is also applied to the analysed observation data.

[1] A pile-up of events with reconstructed directions in the edge of the FoV is known to occur (Rowell 2003).

Apart from the introduction of a RoI, the use of MC simulations instead of OFF data has two more effects on the construction of the background model. One related to the Zd of the telescopes pointing and one other related to the difference in the energy spectrum of gamma-rays compared to CRs. The simulations take into account the effect of the Zd in the instrument's response and provide a uniform distribution in Zd within a given range. Therefore, for this model we must divide the acceptance maps in a minimum of two Zd bins, which coincide with the ranges in MAGIC's standard MC productions (see section 3.3.5).

Regarding the energy spectrum, as mentioned in chapter 3, MC events are simulated with a power-law energy distribution with photon spectral index of $\Gamma_s = 1.6$. In observations, even after *hadronness* cuts, most of the surviving events correspond to showers originated by CRs with an energy spectrum following a power-law with $\Gamma_d \sim 2.7$ (Thoudam et al. 2016). This means that to be able to use eq. (5.2) and estimate the number of observed background counts, we need to weight the simulated events during the computation of the acceptance map $A(\hat{\boldsymbol{p}})$, to account for the difference in energy spectrum between the simulated and observed events. The weight for event i is given by

$$w_i = k\frac{E_i^{-\Gamma_d}}{E_i^{-\Gamma_s}} = kE_i^{-(\Gamma_d-\Gamma_s)}\,, \tag{5.5}$$

where E_i is the true energy of the simulated i event and k is a normalization constant. The weight w_i is applied to each event when filling up the two-dimensional histogram that constitutes the acceptance map. This way, observation data can be compared to the predictions by MC simulations to test the presence of signal events.

The number of events in the binned acceptance maps is arbitrary (i.e. depends on the simulation statistics), so we can obtain the value of k by imposing that the sum of all the weights is equal to 1,

$$\begin{aligned} \sum_{i=1}^{N_{\mathrm{MC}}(\mathrm{Zd})} kE_i^{-(\Gamma_d-\Gamma_s)} &= 1 \\ k &= \frac{1}{\sum_i^{N_{\mathrm{MC}}(\mathrm{Zd})} E_i^{-(\Gamma_d-\Gamma_s)}}\,, \end{aligned} \tag{5.6}$$

where $N_{MC}(\mathrm{Zd})$ is the total number of simulated events, for a given Zd range

selected, after cuts. Now we can finally use eq. (5.2) to estimate the number of expected background events, b_c, detected from a region of the sky with some radius r_S with centre at (x', y') when projected in the camera plane,

$$b_{c(r_S,x',y')}(t) = R_T(t)\Delta t_0 \sum_{i,j} \delta(r_S, x', y')a_{ij} \,, \tag{5.7}$$

where a_{ij} is the number of counts in the bin ij of the acceptance map $\boldsymbol{A}$ and Δt_0 is the temporal precision of R_T (i.e. the temporal interval between measurements of the rate). $\delta(r_S, x', y')$ is a parameter that is equal to 1 for the bins of the acceptance map with centres at equal or less distance of (x', y') than r_S and is equal to 0 for the rest of the bins.

The rate of detected events varies in time for any observation, be it due to changes in the weather conditions, the pointing of the telescopes or technical issues. For that reason, R_T and the projected coordinates of the cells in the camera are obtained in bins of $1\,\mathrm{s}$ width, independently of the duration of the time window. This process is described in more detail in chapter 6.

The final acceptance maps used in this analysis for the estimation of b are shown in the bottom plots of fig. 5.4, with the Gaussian smear version at the top for better visualization and for the comparison to the ones obtained from OFF data. The binning used for both sets has a width of $0.005°$. The selection of bin size for the acceptance maps was optimized to simultaneously minimize the uncertainty of b and the computational time required to obtain it within the analysis. A full description of the process and the tests carried out for that purpose can be found in appendix A.

5.3 Source signal contamination

The basis of this background estimation model lies in the assumption that no already-known VHE gamma-ray source is in the FoV of the observations. Since we are using archival data for the search of transient signals, this is hardly the situation for most of the observations used. As mentioned in section 4.1, the cells located near known sources are removed from the search. The same is done when computing R_T to prevent real gamma-ray signals from being included in the background counts, which would spoil our normalization method (see section 5.2).

To prevent this contamination, we put an additional cut to the reconstructed direction of all the events in the camera, which removes those reconstructed within a 0.2° radius of a TeVCat source. If the source is not point-like, its largest dimension is used as the cut radius.

This prevents R_{T} from being enhanced by the added gamma-ray events, but it also removes part of the background counts of the camera, decreasing the overall rate. In most cases, the excluded region corresponds to a known gamma-ray source that was being observed in a high acceptance region of the FoV, which leads to the model significantly underestimating the number of backgrounds counts expected from any part of the FoV. Therefore, when one or more VHE sources are in the FoV, we measure a smaller background rate R'_{T} instead of R_{T}, which needs to be taken into account.

In this work we used a geometrical approach to estimate the ratio between the measured R'_{T} and the R_{T} needed for background estimation. The ratio is given by the number of sources and their positions in the FoV at a given time during an observation, as follows.

Let's consider an observation with a point-like source in the centre of the FoV. To obtain R'_{T} we exclude events with a reconstructed direction of less than 0.2° around the centre or, in other words, with $\theta^2 \leq 0.04^{\circ 2}$. Since the camera acceptance is not flat and it is actually higher at the centre, more background events have been excluded in this cut than if the source had been near the edge of the RoI. To take this into account, we calculate the relative acceptance in the excluded area, $a_\epsilon(0.0, 0.0) = \sum_{i,j} \delta(0.2, 0.0, 0.0) a_{ij}$, where i goes over the X' axis bins, j goes over the Y' axis bins and δ is 0 for bins with centre outside the θ^2 cut, and 1 otherwise. If more than one source is present, an a^ϵ is calculated for each of them, Since the sum of all the bins in $\boldsymbol{A}$ is equal to 1, we can obtain the background rate in all the RoI as $R_{\mathrm{T}} = R'_{\mathrm{T}} / \left(1 - \sum_i a_{\epsilon,i}\right)$. The validation of the background estimation model for FoVs with and without VHE sources can be found later in section 6.2.

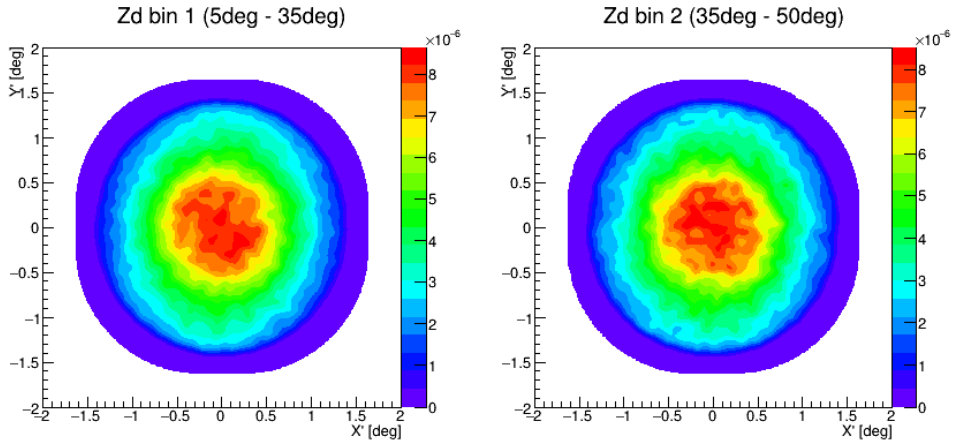

(a) MC acceptance maps with Gaussian smear.

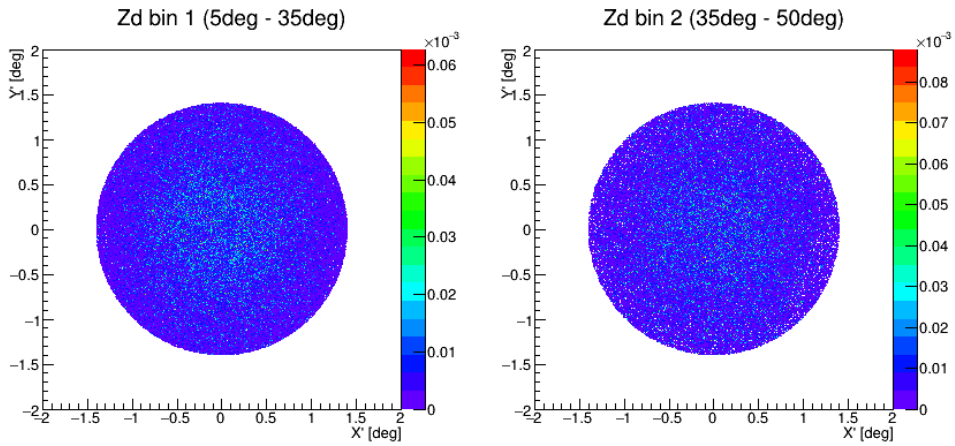

(b) MC acceptance maps with no smearing.

Figure 5.4: Acceptance maps obtained with the *diffuse* MC simulations of period ST.03.03 after applying the azimuth correction for the low (**left**) and the medium (**right**) Zd ranges. For more details on the top figures refer to the caption in fig. 5.1.

Chapter 6

Analysis

Now that we have a model that provides the expected number of background events for any given time and arrival direction within an observation, we can search for the signals of transient phenomena in the archival data we have selected. This is done by comparing the number of observed events with the number of expected background events for each cell and time window. The process is carried out night by night for all the different observed FoVs since the pointing of the telescopes and the event detection rate in all the camera are inputs in the model.

First, the data are divided by cells, and then the events in each cell are grouped into overlapping time windows of chosen width Δt, depending on their arrival time. All the time span of an observation is divided into time windows, common for all the cells in the RoI. Every time window of every cell is considered as a trial when computing the significance of a possible signal (as long as the camera rate is not zero at that time period, which would mean that data taking was halted for whatever reason).

To get the expected number of background events in a window, we follow eq. (5.7) and sum it over the window duration Δt. In the expression, the elements a_{ij} are fixed (inside a range of Zd: low or medium) and $R_{\mathrm{T}}(t)$ is the same for all the cells that are visible during one night of observations of a source. What has to be calculated for each cell is $\delta(r_{\mathrm{S}}, x', y')$, which is obtained through a MARS function from the equatorial coordinates of the cell and the specific pointing of the telescopes at a given time. The same cell can be projected into different parts of the camera plane at different times. This is caused, by the most

part, by the change in pointing coordinates in wobble mode observations.

Additionally, the altazimuth mount of the MAGIC telescopes (see chapter 3) and the mechanical fluctuations of the structures holding the mirrors can cause small variations in the projected coordinates of a cell within one run.

Since we have the overall rate of the camera and the telescopes pointing for every second of an observation, we can calculate the expected number of background events b_i for every second a cell is observed. Finally, we sum all the b_i according to the chosen time window width (Δt) and overlap to obtain the number of expected background counts in a time window j that starts at time t,

$$B_j = \sum_{i=j}^{j+\Delta t-1} b_i \,, \tag{6.1}$$

where B_j is the number of background events in a time window that starts at second $j = t$ and has a width Δt.

The number of observed events follows a Poisson distribution, regardless of whether we expect only background counts or also a VHE signal to be present for that particular time window and cell, as seen in fig. 6.1. Thus, we can express the mean of the distribution, μ, as the sum of a background only contribution and a signal only contribution, $\mu = \mu_{\text{bkg}} + \mu_{\text{signal}}$.

Since we don't know *a priori* the signal characteristics of the transient phenomena we are searching for, we have to look for an excess of events over the expected background. That is, we have to test our data against the null hypothesis, H_0, that $\mu_{\text{signal}} = 0$. Our test-statistic is the number of gamma-like events N observed in a spatial cell and temporal window of width Δt.

To estimate the significance of any upward deviations in the data, and, therefore, the significance of the presence of a signal, we compute the p-value for each time window and spatial cell. The p-value is the probability of obtaining a result as compatible or less with H_0 than the one actually observed. Therefore, a very small p-value would mean that the likelihood of N consisting of only background events is very low and the null hypothesis can be rejected. In our case the p-value is given by the one-sided cumulative function of the Poisson distribution,

$$p = P(n \geq N; \mu) = \sum_{n=N}^{\infty} \frac{\mu^n e^{-\mu}}{n!} \,, \tag{6.2}$$

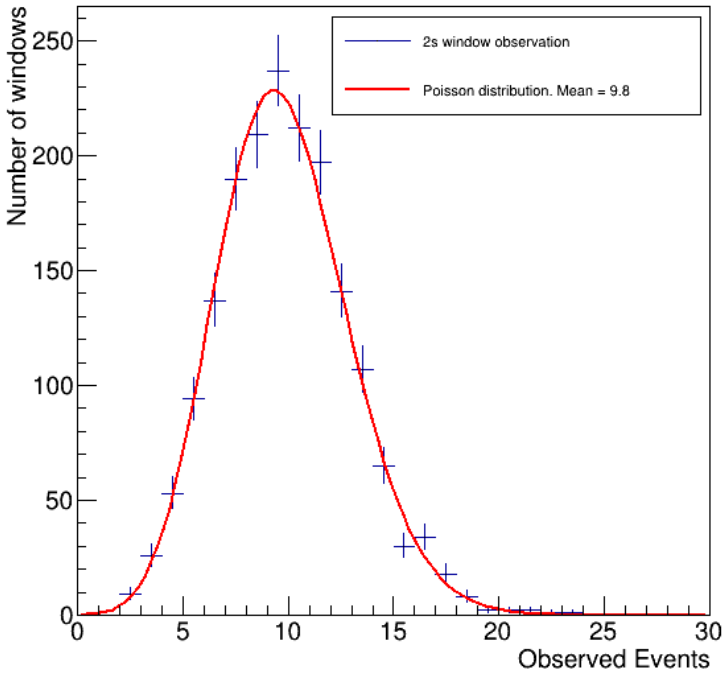

Figure 6.1: Distribution of the number of observed events (after event selection cuts) in 2 s time windows and all the spatial cells of the FoV corresponding to observations of 3c454.3. The red line corresponds to a Poisson fit with the same mean as the data.

where p is the p-value and $P(n \geq N; \mu)$ is the probability of detecting a number N or more of events, when n follows a Poisson distribution with mean μ.

For easier visualization, we can translate the p-value into significance $\mathcal{S}$ as the number of standard deviations in a normal distribution with the complement of the error function, erfc:

$$\mathcal{S}(n \geq N; B) = \sqrt{2}\mathrm{erfc}(2\,P(n \geq N; B))\,. \tag{6.3}$$

In this simple approach, a fluctuation with $p = 2.87 \times 10^{-7}$ corresponds to a 5σ detection. However, determining the real significances in the present algorithm is more complicated than this. The cause is the large number of trials used in the search and the existence of systematic uncertainties introduced by the background model.

A large analysis such as this one, where more than 1000 h of data were analysed with time windows of 2 s, 10 s, 100 s and 1000 s, faces the challenge of

estimating the correct significance of a possible signal when a vast amount of trials have been performed. A trial is considered to be each time a time window is tested against the background only hypothesis. While these trials are essential for a comprehensive investigation, they also elevate the risk of making one or more Type I errors, or false positives. This is known as the FamilyWise Error Rate (FWER), or experimentwise error rate. Without correction, the chance of making at least one false discovery among all the trials becomes unacceptably high.

We can account for this effect by applying the Šidák correction (Šidák 1967). Assuming that the individual trials are independent from each other, this problem of multiple comparisons can be corrected by calculating an adjusted p-value,

$$p = 1 - (1 - p_{\min})^{N_t}\,, \tag{6.4}$$

where $p_{\min}$ is the minimum p-value obtained in the N_t trials. That is, the probability that in at least one of the trials we would get a result in the region of equal or lesser compatibility with H_0 than that of the observed result, given that H_0 is true. This p, known as the post-trials p-value, refers to the true rate of occurrence for a result to be obtained after multiple trials, and is no longer equivalent to eq. (6.2).

In practice, p controls the significance level of the whole experiment, so if we require a 5σ significance to claim the detection of a signal, it is referred to this p. As we will see, the individual p-values calculated in many time windows and cells will give pre-trial significances of over 5σ, that do not warrant a detection after correcting for the number of trials used. In fig. 6.2 we can see the pre-trials significance of a sample of time windows and how it relates to the post-trials significance at 3σ and 5σ.

6.1 Effective number of trials

Along with the large number of trials, an additional layer of complexity emerges due to the application of overlap in the time windows and spatial cells used in the search. This overlap introduces correlations between the p-values obtained for the different trials, rendering them non-independent.

However, we can use the definition of p-value to calculate the number of effective independent trials in our search, N_{eff}, for which eq. (6.4) holds true. In

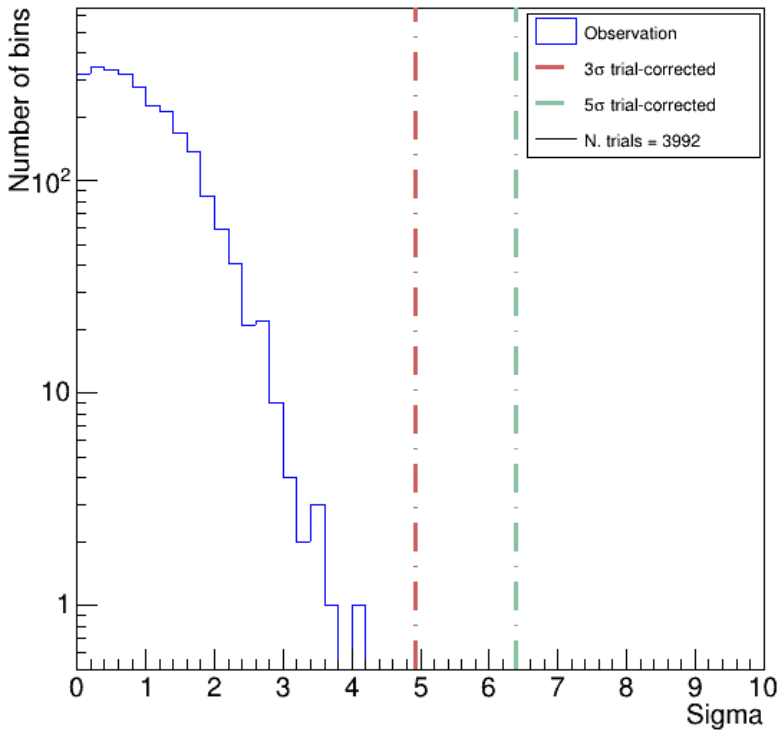

Figure 6.2: Histogram with the pre-trials significance of the excess in events of every time window and spatial cell in 2.1h of observations in the FoV of 3c454.3. The red line corresponds to the significance needed, before trials correction, for a 3σ detection and the green line corresponds to the 5σ detection. The time window used has a width of $\Delta t = 100s$.

eq. (6.4), p is the p-value of the random variable $p_{\min}$, so, by definition, p can be calculated as the Cumulative Distribution Function (CDF) of $p_{\min}$. The result of the two approaches coincide when trials are independent, and differ otherwise. Therefore, if we can calculate $\mathrm{CDF}(p_{\min})$ when trials are correlated, we can equate it to eq. (6.4) and obtain N_{eff}, which must be $N_{\mathrm{eff}} \leq N_{\mathrm{t}}$.

Since we don't expect the PDF of $p_{\min}$ to be an analytical expression, we use toy simulations to estimate it and fit its CDF to eq. (6.4) leaving N_{t} as a free parameter. This way we can verify that we obtain $N_{\mathrm{eff}} = N_{\mathrm{t}}$ when trials are independent, and then obtain the N_{eff} in our experiment.

In the search algorithm used in this work there is a spatial and a temporal overlap. The contribution of each one to the correlation of observed events is independently simulated to obtain a ratio between the number of effective trials

and the number of simulated trials, $k = \frac{N_{\text{eff}}}{N_{\text{t}}}$. Consequently, the effective number of trials in the real analysis is calculated as $N_{\text{eff}} = N_{\text{windows}} N_{\text{cells}} k_{\text{s}} k_{\text{t}}$, where k_{s} is the effective coefficient for cell overlap and k_{t} is the effective coefficient for time window overlap.

The design of the toy simulations is, in general terms, the same for temporal overlap and spatial overlap. The main difference between them is the geometry used to introduce correlations between trials, with time windows being one-dimensional and spatial cells being two-dimensional[1]. This is an outline of the process:

- Consider N_{fine} bins of size t_{fine} with no overlap among them. Each of these "fine" bins contains a number of expected background counts, ν_k, with $k = 1, 2 \ldots N_{\text{fine}}$.
- Then we have N_{coarse} bins of size $t_{\text{coarse}} = n_{\text{fine}} t_{\text{fine}}$, where n_{fine} is a positive integer.
- To induce correlation in the p-values calculated for these "coarse" bins, we add an overlap between them.
- The level of overlap is quantified as $n_{\text{common}}/n_{\text{fine}}$, where n_{common} is the number of fine bins that belong to a coarse bin and to the next one at the same time.
- We simulate a large number of detected counts for the fine bins using a Gaussian distribution with ν_k as the mean and $\sqrt{\nu_k}$ as the standard deviation.
- This way we have a large number of executions of the experiment of "counting the events detected in the N_{fine} bins".
- For each experiment, the number of events of the fine bins are summed into the coarse bins. The resulting content is $n_{i,j}$, the observed number of events in the $j\text{th}$ coarse bin and the $i\text{th}$ experiment.
- The expected number of counts in a coarse bin, μ_j, is the sum of the nu_k of the fine bins that are summed into it.
- We calculate the p-values of each coarse bin and experiment, $p_{i,j}$ with $n_{i,j}$ and μ_j.

[1] The position of the cells is based on a HealPy grid, as described in section 4.1, which introduces constraints on the precision we can use in the simulations and to calculate their overlap.

- For each experiment i, we select the minimum p-value out of the N_{coarse} bins, so that we have $p_{\text{min},i}$.
- We can estimate the PDF and CDF of p_{min} with these simulated $p_{\text{min},i}$.
- Finally, we fit eq. (6.4) to $\text{CDF}(p_{\text{min}})$ leaving N_{t} as the free parameter. N_{t} will be N_{coarse} when no overlap is applied, and a smaller number otherwise.

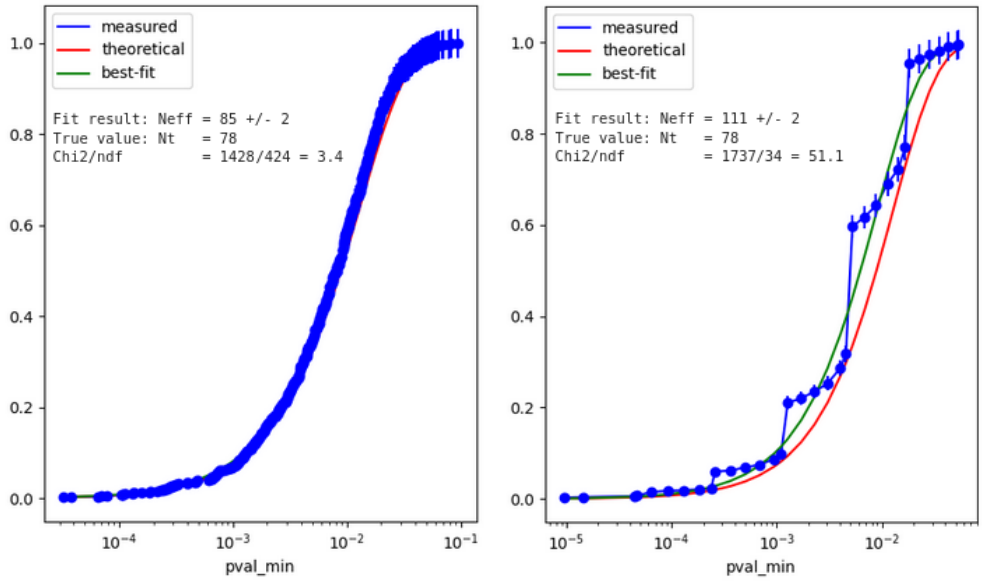

Figure 6.3: Cumulative distribution of the simulated $p_{\text{min},i}$. The blue line corresponds to the summed $p_{\text{min},i}$, the red line corresponds to eq. (6.4) with $N_{\text{t}} = N_{\text{coarse}}$ and the green line corresponds to the fit of eq. (6.4) to $\text{CDF}(p_{\text{min}})$. The result of the fit is shown together with the actual number of trials used. In the left plot, 1000 random numbers were generated following a Poisson distribution with 78 different μ values from the observation of cell 120 866. In the right plot, 1000 random numbers were generated following a Poisson distribution with 39 of the μ values set to 2 and 39 set to 100.

We can't use a Poisson distribution to generate the $n_{i,j}$, since we are using μ_j, which are also integers. If we do use it, the result is a discrete distribution of p-values which fails to reproduce eq. (6.4). The effect becomes more obvious when the distribution of μ_j is not uniform. In fig. 6.3 we show this by comparing two results of the simulations using a Poisson distribution. In one of them μ_j was obtained from the time windows of a given cell in the search and in the other one μ_j is set to be 100 for half of the simulations and 2 for the other half.

On the other hand, we can use a Gaussian distribution to generate the $n_{i,j}$,

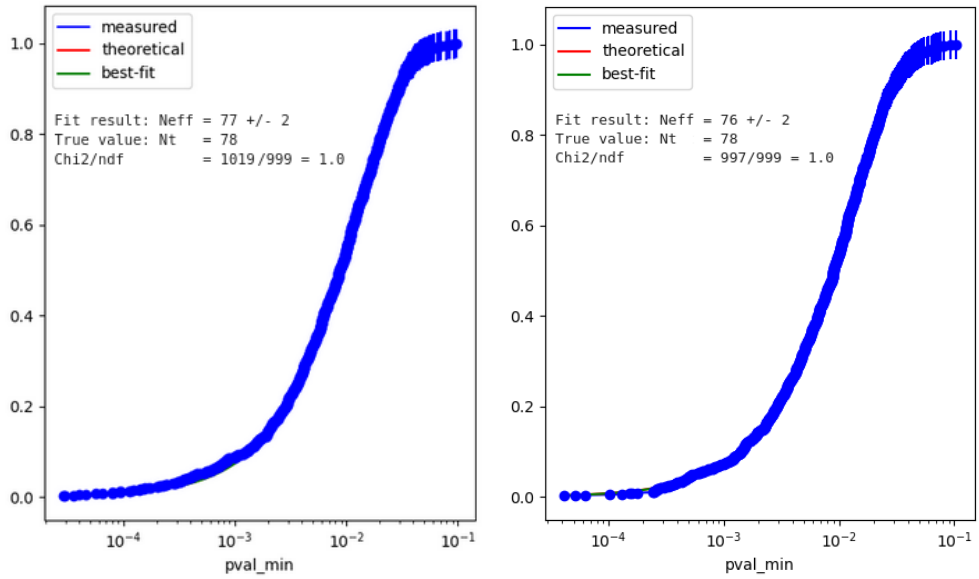

Figure 6.4: Cumulative distribution of the simulated $p_{\min,i}$. The blue line corresponds to the summed $p_{\min,i}$, the red line corresponds to eq. (6.4) with $N_\mathrm{t} = N_\mathrm{coarse}$ and the green line corresponds to the fit of eq. (6.4) to $\mathrm{CDF}(p_\mathrm{min})$. The result of the fit is shown together with the actual number of trials used. In the left plot, 1000 random numbers were generated following a Gaussian distribution with 78 different μ values from the observation of cell 120 866. In the right plot, 1000 random numbers were generated following a Gaussian distribution with 39 of the μ values set to 2 and 39 set to 100.

as it is continuous and is therefore able to reproduce eq. (6.4) regardless of the values used as μ_j. In fig. 6.4 we repeat the test done for fig. 6.3 using a Gaussian distribution instead. These plots show that the fit of the CDF of simulated p_min to eq. (6.4) results in $N_\mathrm{eff} = N_\mathrm{t}$ when the trials are not correlated.

Now that we have checked that the simulation method works, we can start to obtain the effective coefficients k_t and k_s for different overlaps, bin sizes and ν_k. This will allow us to see if the results of the simulations are consistent and if they follow any trend depending on the varied characteristic. For example, it can be expected that the number of effective trials will be lower for higher percentages of overlap.

6.1.1 Temporal overlap

We start by obtaining the effective coefficient for temporal overlap, k_t. In fig. 6.5 we show the resulting distribution of minimum p-values for 50 % overlap. The

ν_k used are the number of detected events in time bins of $10\,\mathrm{s}$ in cell $120\,866$, summed into larger bins of $100\,\mathrm{s}$. We can see that the cumulative distribution of the simulated p-values still follows eq. (6.4) but with $N_{\mathrm{eff}} < N_{\mathrm{t}}$, as expected. From the result of the fit we calculate k_{t} as $N_{\mathrm{eff}}/N_{\mathrm{t}}$.

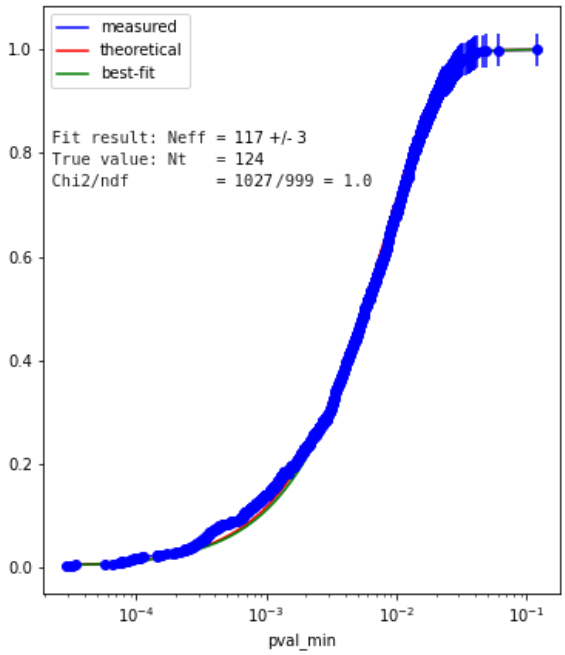

Figure 6.5: Cumulative distribution of the simulated $p_{\mathrm{min},i}$ with a $50\,\%$ overlap. The result of the fit of the curve to eq. (6.4) shows a lower number of effective trials than the true number of trials, as expected. For more details refer to fig. 6.4.

We performed multiple simulations with different levels of overlap and taking ν_k from different cells to test the validity of the method and obtain k_{t} in a variety of scenarios. We selected cells from different directions and with different mean event detection rates. In fig. 6.6 we can see how the percentage of overlap and the differences in the mean event rate in a cell can affect the value of k_{t}.

We also tested how k_{t} varies for different time window sizes. In fig. 6.7, the ν_k used for the simulations are obtained from the same spatial cell. First, the time that the cell is observed is divided into 396 time windows, where the mean number of detected events is 19.78. Then, the cell is divided into increasingly larger time windows which have, consequently, a higher number of detected

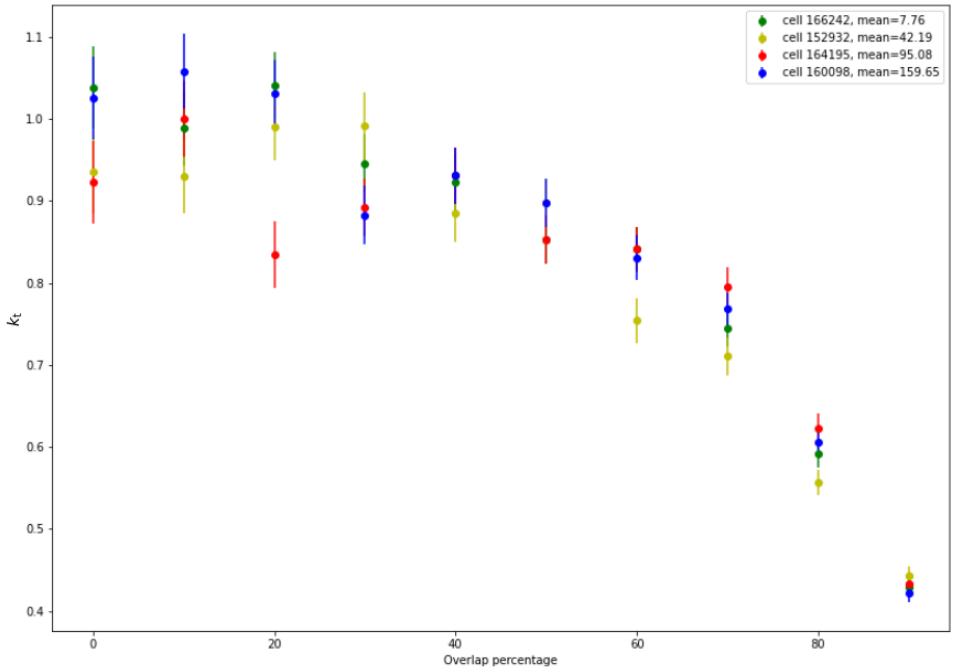

Figure 6.6: Results for the ratio of N_{eff} and N_{t}, denoted in this plot as k, due to the overlap of time windows in the search algorithm. Each dot denotes the result of the simulation carried out with a different percentage of overlap in the coarse bins (time windows). The different colours correspond to the use of ν_k from spatial cells with different mean event detection rate.

events.

In the results obtained in this work, we used a 50% overlap on the $2\,\text{s}$, $10\,\text{s}$ and $100\,\text{s}$ windows, which corresponds to an effective coefficient of $k_{\text{t}} = 0.87$. The $1000\,\text{s}$ time window analysis requires a minimum of $80\,\%$ overlap due to the limited duration of an observation run. We found that this overlap does not result in an increased sensitivity to transient signals, so the $1000\,\text{s}$ time window search is performed with $0\,\%$ overlap, and thus $k_{\text{t}} = 1$ in this case.

6.1.2 Spatial overlap

The procedure to obtain the effective coefficient for spatial overlap (i.e., due to the overlap in the search cells), k_{s}, is essentially the same as the one just detailed, with some technical differences.

In this case we are not able to define fine and coarse bins as freely as we

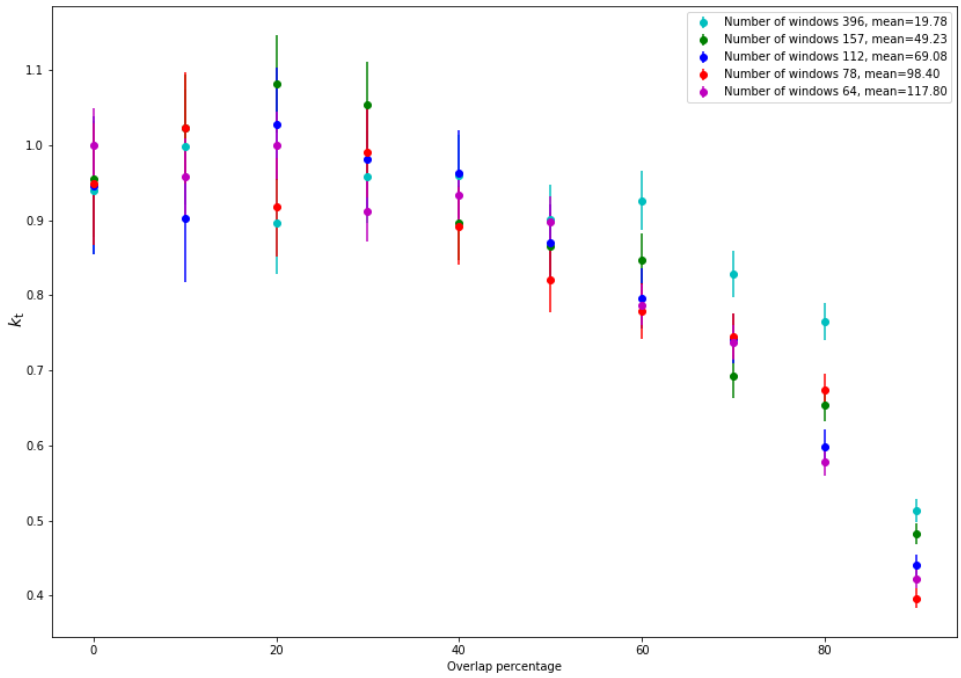

Figure 6.7: Results for the effective coefficient k_t obtained by varying the size of the time windows and their overlap percentage. The different colours indicate the sets of simulations performed with ν_k from time windows of varying sizes and mean.

want, we have to use the **HEALPix** grid of the search algorithm, which is described in section 4.1. As opposed to the number of time windows in the search and, therefore, the number used for the simulations, which can vary depending on the total amount of time that the selected cell has been observed, the number of cells that fit into the FoV of MAGIC, or the RoI that we are selecting within it, is more or less fixed.

The exact number of cells can change slightly depending on the pointing of the telescopes, since the grid is not regular (see section 4.1), but it is always around 110 cells for the $3.5°$ FoV of MAGIC. Extending the simulations past this size does not provide more information on the correlation of p-values in the analysis.

The spatial cells of the search algorithm correspond to the coarser bins in the simulation outline. The finer bins are obtained with **HEALPix** as the smaller pixels of a much finer grid: $NSIDE = 2^{13}$ versus our original grid of $NSIDE = 256$.

The correlations between trials are introduced in the same way, by summing fine bins into coarser bins, but this time they are two-dimensional pixels summed into our two-dimensional cells. This introduces a technical difficulty. Compared to the temporal overlap simulations, the precision we can obtain when simulating overlap in the cells is limited by the number of **HEALPix** pixels we can create[2]. Furthermore, to validate that $N_{\text{eff}} = N_{\text{t}}$ when no overlap is applied to the spatial cells for our grid with $NSIDE = 256$, we have to reduce the size of the cells. Consequently, we can not use the results from the search algorithm (the number of detected events per cell and time window) to obtain the ν_k we use in the simulation.

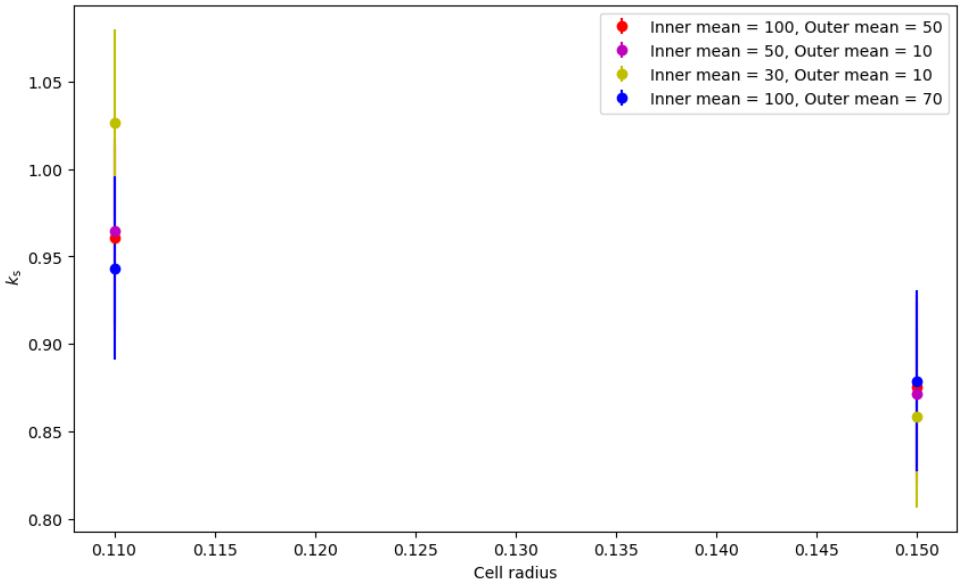

Figure 6.8: Effective coefficient for spatial overlap as a function of the cell radius. The simulations were done for a FoV with a $0.85°$ radius divided into a centre circular area of $0.6°$ radius and an outer ring area. The different colour dots correspond to different ν_1 and ν_2 used. The dots to the left correspond to no overlap and the dots to the right correspond to the overlap used in the analysis.

Since we are not able to use the real number of detected events in a variety of FoVs and observation conditions, we try to recreate them by choosing different sets of ν_k. To roughly reproduce the camera acceptance shape with the numbers introduced in the simulation, we divide the FoV into a centre circular

[2] **HEALPix** pixels are rhomboids, while our spatial search cells are circles, so a very large number of infinitesimally small pixels is needed to accurately map the area of the circle.

area and a varying number of external rings. The fine bins (pixels) of the different areas will have a single ν_l value assigned to them, with $l = 1, 2 \ldots N_{\text{divisions}}$ and ν_l being a higher number at the centre that descends toward the edge of the FoV. For example, if we do $N_{\text{divisions}} = 2$ and divide the FoV into a centre area and a ring, we have ν_1 and ν_2 for generating numbers according to a Gaussian distribution.

To obtain k_{s} for a variety of conditions we performed the simulations with different FoV sizes, different ν_l and $N_{\text{divisions}}$ and modifying the proportions of the divided areas within the chosen FoV size. We started with a FoV of $0.85°$ in radius and 1000 simulations per fine bin.

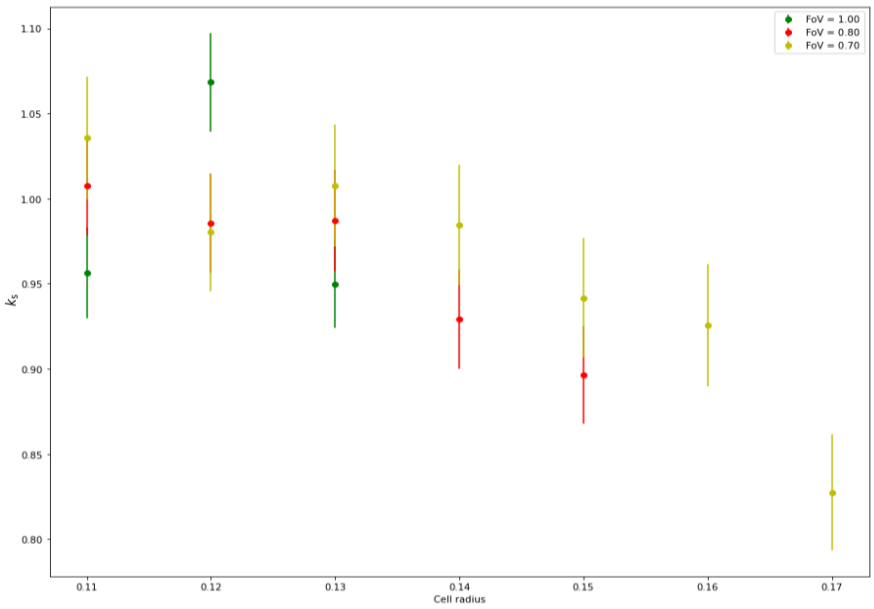

Figure 6.9: Effective coefficient for spatial overlap as a function of the radius of the cells. The simulations were done with $\nu_1 = 100$ and $\nu_2 = 50$ and a central circular area of radius 0.5 times the radius of the FoV. Three different FoV radii were explored.

In fig. 6.8 we show the k_{s} values resulting from two sets of these simulations. The first four simulations have no spatial overlap, as the fine bins have been summed into cells of radius $0.11°$, without spatial or temporal overlap.

We also checked how the coefficient would vary with different cell radius (overlap level) and different FoV sizes (see fig. 6.9). Various configurations of the areas of the FoV were also checked for consistency, involving more than

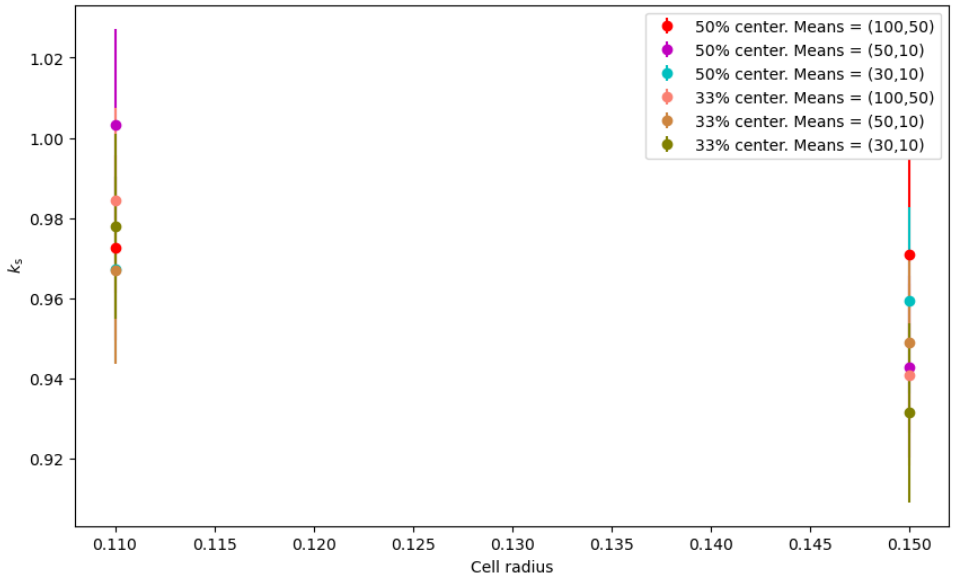

Figure 6.10: Effective coefficient due to the spatial overlap of cells, for a case with no spatial overlap and the case with the overlap used in the transient search. The simulations were done over an area equal to a FoV of radius $1.4°$. The simulations were done with different centre and corona mean values and two different centre radius.

two areas and different size ratios among them. In fig. 6.10 we show the results of some of the simulations done on an area covering the RoI used in the analysis, with a radius of $1.4°$.

For FoVs over $1.0°$, we had to reduce our smaller grid one order of magnitude due to computational constraints, which results in a lower resolution of the overlap and, therefore, more disparity in the results from the simulations. Over the multiple configurations tested we saw that some of them would give very different k_s values depending on the seed used to generate the random numbers.

The tests done on smaller FoVs provide a lower mean value for k_s with a narrower distribution than those done on larger FoVs (see fig. 6.8 against fig. 6.10). Since the larger tests had to be done with a lower number of simulations ($NSIDE = 2 \times 10^{12}$), we calculated the effective coefficient for spatial overlap as a weighted average of the results for FoV = $0.85°$ and FoV = $1.4°$.

In the end we have $k_s = 0.93$ for the spatial overlap correction and $k_t = 0.87$ for the temporal overlap correction. Therefore, the effective number of

trials in the final analysis of the significance of a transient signal candidate is $N_{\text{eff}} = N_{\text{windows}} \times N_{\text{cells}} \times 0.87 \times 0.93$.

6.2 Background model validation

The validation of the background estimation model obtained in chapter 5 is performed by applying the search algorithm to a reduced subset of observations and comparing the results with those obtained from simulated background-only events. Given the current, most stringent, upper limits on PBH evaporation, $\dot{\rho} = 3300\,\text{pc}^{-3}\text{yr}^{-1}$ (Albert et al. 2020), and MAGIC's GRB detection rate of $0.067\,\text{yr}^{-1}$ (MAGIC Collaboration 2019), we expect most of the analysed data to consist only of gamma-like background events, given that we have already excluded known VHE sources from the data.

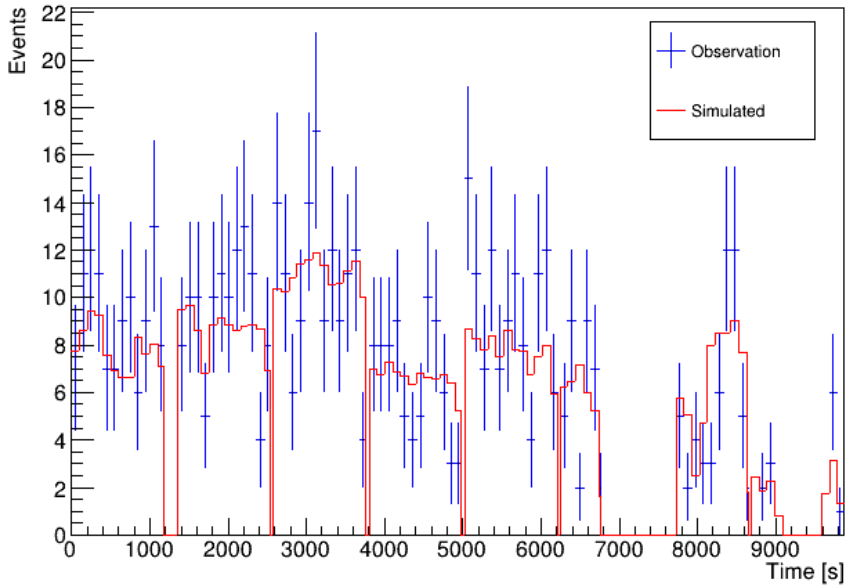

Figure 6.11: Light curve of a cell in the extragalactic FoV around 3c454.3, with window size $\Delta t = 100$s. The blue line corresponds to the observed events and the red line corresponds to the expected number of background counts predicted by our model.

Therefore, we should be able to use some randomly selected observations to check that the number of detected events in their time windows and spatial cells do, indeed, follow a Poisson distribution with a mean given by our model.

We first select OFF observations to perform the validation tests to remove any possible effects due to signal contamination from known gamma-ray sources.

6.2.1 OFF sample validation

The background rates of galactic and extragalactic observations are different. In order to see if this has an effect on the accuracy of the background estimation model, we selected some observations from a galactic FoV with no source detections and an extragalactic FoV with no detections. The non-detected sources whose observations were used are, specifically, B1957+20 and 3c454.3, on the nights of 2013/08/30 and 2014/07/27, respectively.

The method to test the model requires that we apply the search algorithm to the selected data, in order to obtain the number of events detected in every time window of every cell, N_i, and their corresponding expected number of background counts, B_i, as detailed in chapter 5 and in the first part of chapter 6.

In fig. 6.11 we can see the light curve of detected events and expected background counts in one cell in the FoV of 3c454.3 as an example of the application of the background model. These histograms are equivalent to a time window search of the cell with no overlap[3]. Thus, the blue histogram corresponds to the N_i of the cell and the red histogram corresponds to the B_i.

To compare the distribution of observed events with a distribution that is known to be caused only by the background, we use the B_i to simulate numbers of detected events, M_i. We have established (see chapter 5) that background counts should follow a Poisson distribution with mean $\mu = \mu_{\mathrm{bkg}} = B_i$. Consequently, we simulate a number M_i for each time window and cell, using B_i as the mean of the Poisson distribution.

We obtain the p-values of the number of observed events N_i and of the simulated M_i using eq. (6.2) and plot their distribution for comparison. For a more quantitative comparison we calculate the studentized residuals of the distributions of $\log_{10}(p)$ and fit them to a constant function. Studentized residuals are computed as residuals (the difference between the observed value and the

[3]The tests were performed with the $50\,\%$ overlap chosen for the transient search, but we see no advantage in showing the second light curve of the cells, which is simply displaced to the right by $0.5\Delta t$.

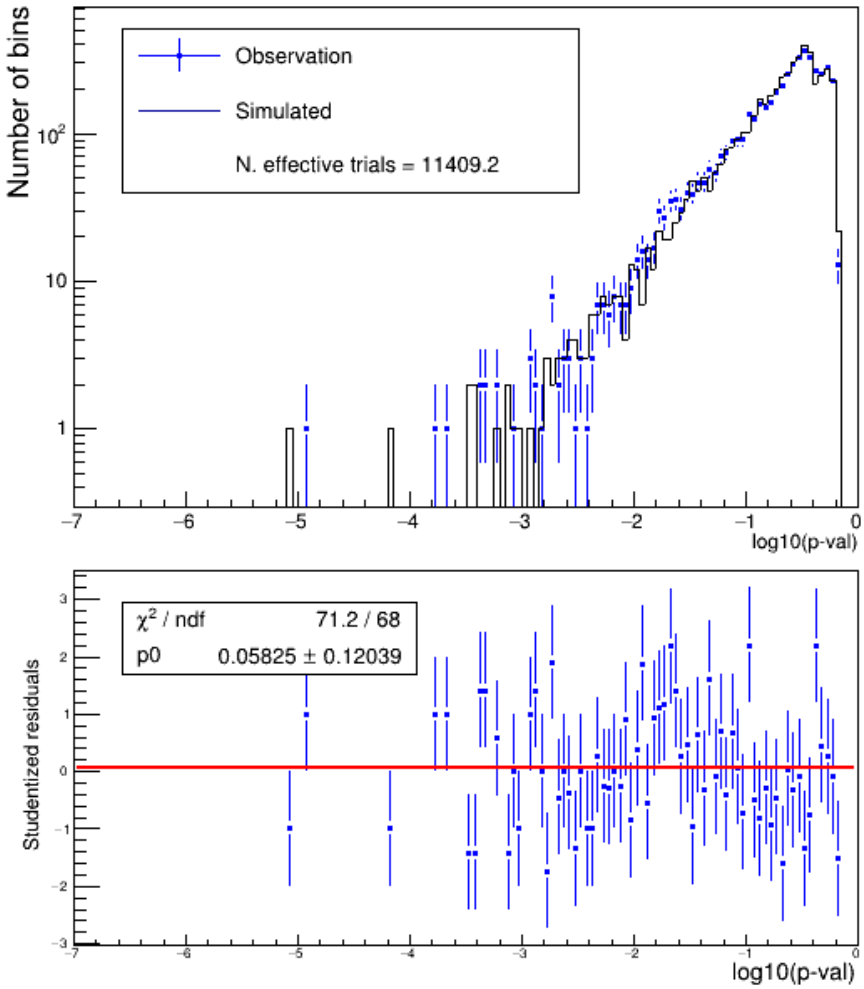

Figure 6.12: Comparison between the results from observed events and from simulated background events for one night of observations of the extragalactic FoV around 3c454.3. **Top:** Distribution of $\log_{10}(p)$ (pre-trials correction) from observed events (blue dots) and simulated events (black histogram). **Bottom:** Residuals of the p-value distributions with the results of the fit to a constant function (red line).

estimated value we are considering), divided by their standard deviation. The results for 3c454.3 and B1975+20 are shown in fig. 6.12 and fig. 6.13.

There is a good agreement within the distributions of simulated and observed results in both figures, confirming that the background estimation model presented in chapter 5 is successful at providing the gamma-like background for the data in the selected period.

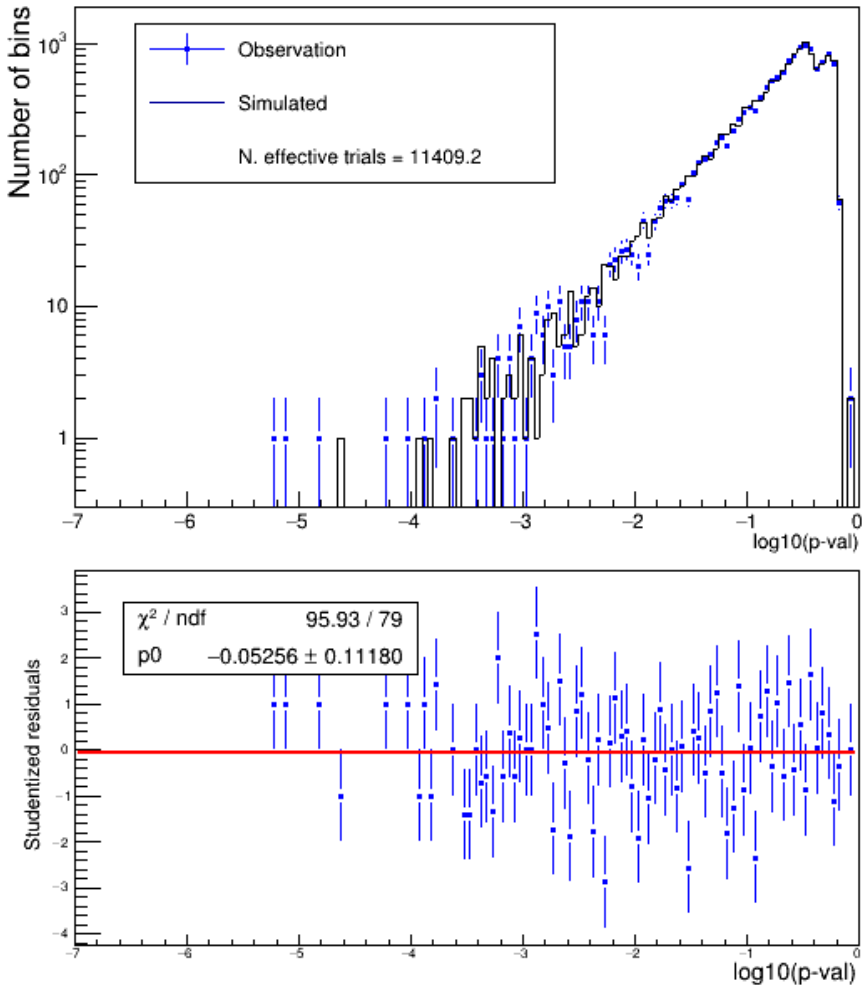

Figure 6.13: Comparison between the results from observed events and from simulated background events for one night of observations of the extragalactic FoV around B1957+20. **Top:** Distribution of $\log_{10}(p)$ (pre-trials correction) from observed events (blue dots) and simulated events (black histogram). **Bottom:** Residuals of the p-value distributions with the results of the fit to a constant function (red line).

6.2.2 VHE signal sensitivity

We test the capabilities of the algorithm to detect known gamma-ray sources by applying the analysis on Crab Nebula data without excluding any cell from the grid (see section 4.1). Specifically, the observations used for the test were conducted on 2013/11/13. In fig. 6.14 we can see the light curve of the cell covering the position of the Crab Nebula and how the observed events are systematically

higher than the expected background in that position. The plot also shows the varying background rate with time, which is caused, by the most part, by the change in Zd over the span of the observation. Additionally, as described in chapter 5, small changes from bin to bin in the background counts estimated by the model are expected from the temporal dependence of the background rate of the whole camera and of the camera coordinates of the cell. In contrast, a cell from the same FoV but far away from the source shows a number of observed events in its time windows that is consistent with the expected number of background events predicted by our model, as is shown in fig. 6.15.

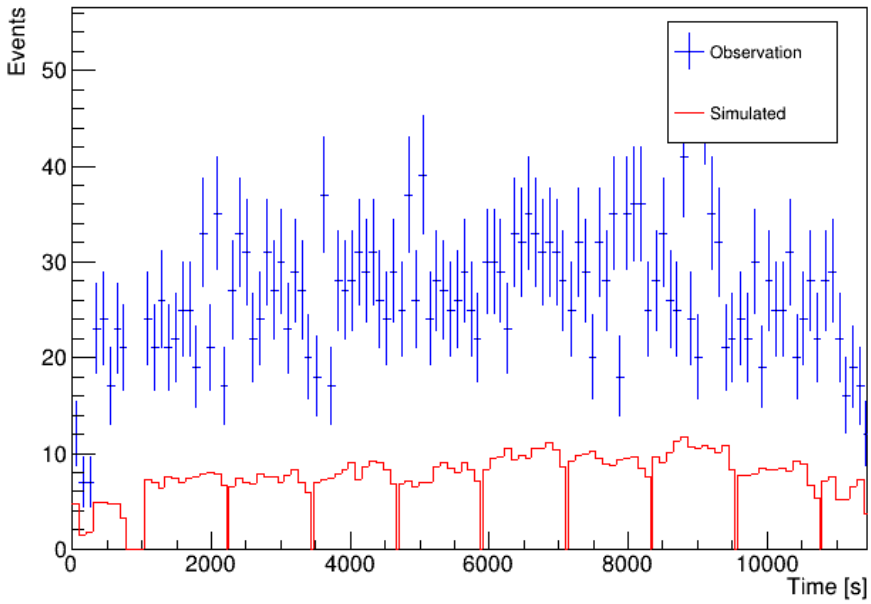

Figure 6.14: Light curve of the cell that corresponds to the position of the Crab Nebula, in seconds after the start of the observation. The blue dots correspond to the number of observed events and the red line corresponds to the expected number of background events. The binning corresponds to a 100 s search window.

The plot in fig. 6.16 shows the results of the application of the search analysis over all the cells in the RoI of the FoV of the observations of the Crab Nebula during the night of 2013/11/13, with a time window of $\Delta t = 100s$ and a 50 % overlap. We can see that the source is detected with a significance of over 5σ even after the correction for trials.

In addition, we applied the algorithm over data from Mrk421 during a flaring state to check the detection of variability in a known source. The flare

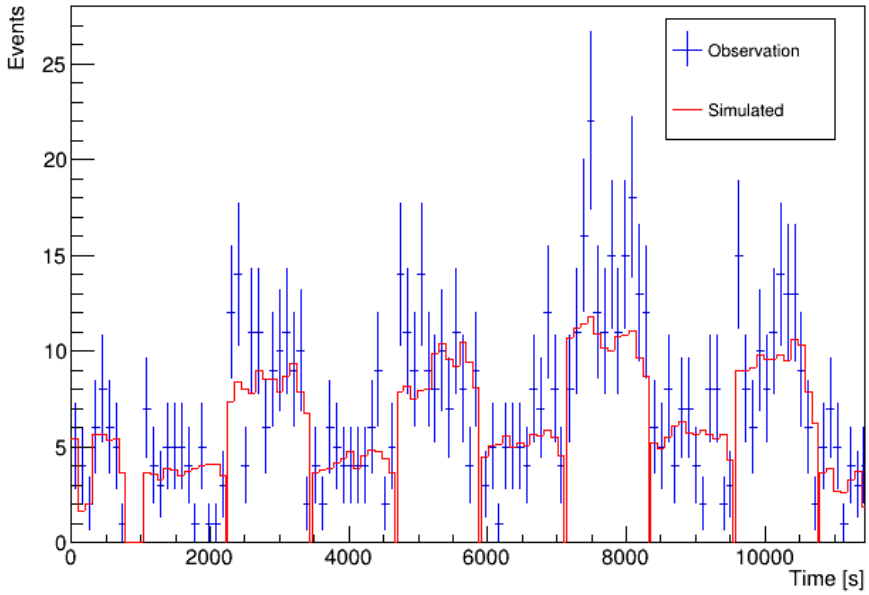

Figure 6.15: Light curve of a cell in the FoV of the Crab Nebula, in seconds after the start of the observation. The blue dots correspond to the number of observed events and the red line corresponds to the expected number of background events. The binning corresponds to a 100 s search window.

analysed was that of night 2014/04/26. The variability in number of detected gamma-like events can be seen in fig. 6.17, where the light curve of the cell containing Mrk421 is plotted together with the number of expected background events for the same time windows.

The results from the analysis of the time windows are portrayed in fig. 6.18, where the significance obtained is 2 times higher than the same analysis performed on a different day of Mrk421 observations (see fig. 6.19 for the same analysis results obtained two days after the flaring state).

6.3 Systematic Uncertainties

For small time windows (2 s to 100 s), the differences between the predicted and observed number of background events are dominated by statistical fluctuations, whereas for larger windows the systematic uncertainties of the background model become apparent. The application of increasingly longer time windows shows a widening of the distribution of significances of the observed

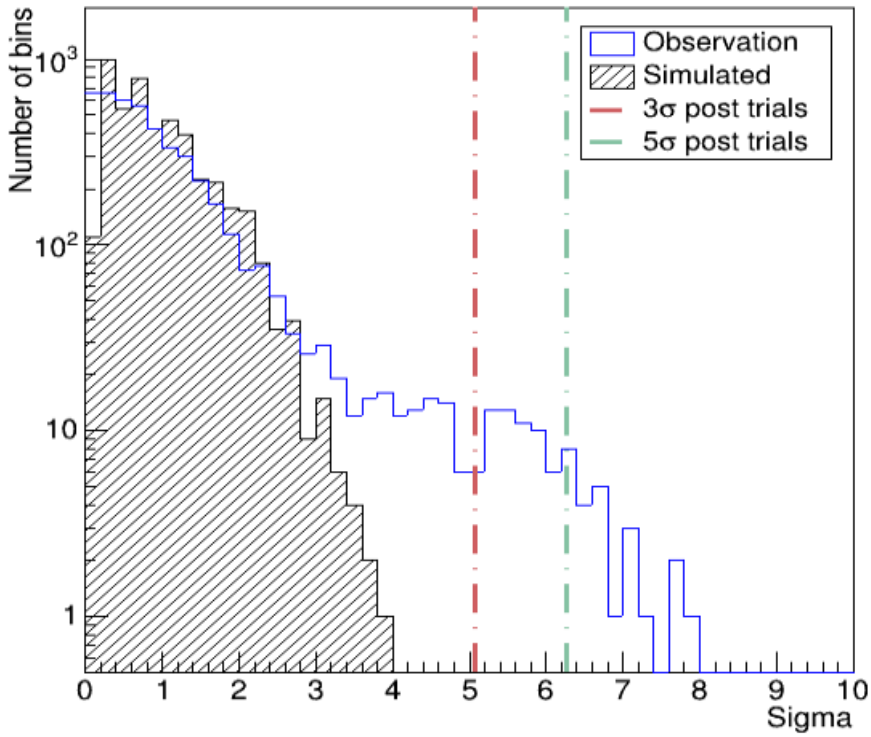

Figure 6.16: Pre-trial significance distributions from the results of the search algorithm done with a 100 s time window on one night of Crab Nebula observations. No cells containing VHE sources were excluded in this analysis. The red and green lines mark the 3σ and 5σ trial-corrected significances. The blue histogram contains the pre-trial significance of the excess of observed events in every window and cell of the RoI and the black histogram contains the pre-trials significance of the simulated background events for the same time windows and cells.

events that is not reproduced by the simulations.

To portray this effect and obtain a quantitative measure of the deviation of the distributions from each other, we applied the search algorithm on a month of observations around the FoV of 3c454.3 with time windows of 200 s, 300 s, 400 s and 500 s. In each of the analyses, the difference between the significance distribution of observed events and the significance distribution of simulated events was computed via a χ^2 test. These results can be seen in the panels of fig. 6.20. The widening effect is maximum in the 1000 s time window analysis, as we can see in the left panel of fig. 6.21.

Up until this point, we have calculated the significance of the excess in observed events compared to the expected number of background events as a

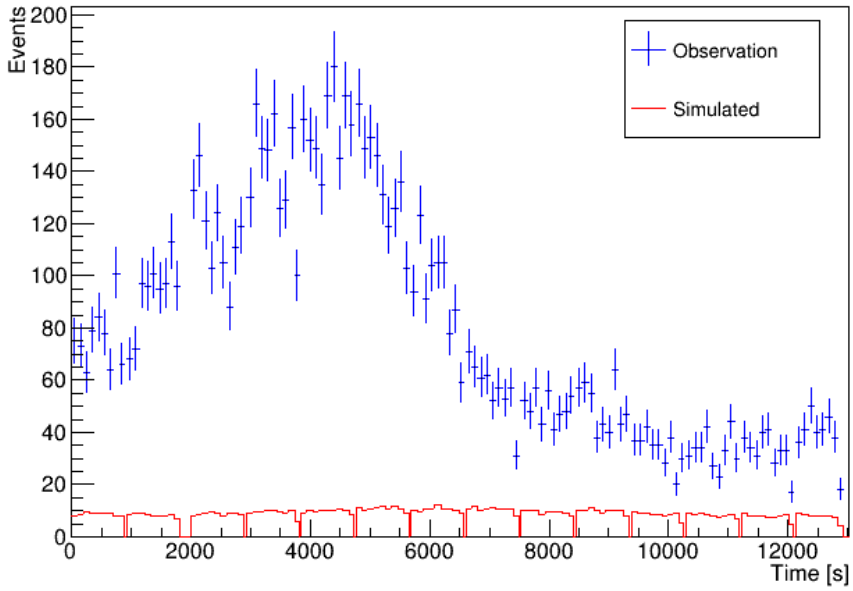

Figure 6.17: Light curve of the cell that corresponds to the position of Mrk421, in seconds after the start of the observation. The blue dots correspond to the number of observed events and the red line corresponds to the expected number of background events. The binning corresponds to a 100 s search window.

one-tailed test. That is, the p-value is calculated to estimate the significance of $N > B$, as defined in eq. (6.2). When $N \leq B$, the introduction of the corresponding p-value into eq. (6.3) results in a negative significance which can be plotted together with the positive significances from the cases when $N > B$ to have a double-tailed distribution.

By comparing the double-tailed distributions we can determine whether our model contains a bias in the prediction of the mean value of expected background events, B, or an underestimation of the fluctuations around the mean beyond the expected from a pure Poisson process, that should be attributed to effects not accounted for in our model (e.g. residual effects from the approximate Zd and Az dependencies, changes in acceptance due to weather or hardware response differences, etc.).

In the right panel of fig. 6.21 we can see that the double-tailed distribution from observed events is wider in general than its counterpart from simulated events. That is, there is no positive bias towards higher significances but a mismatch between the data and the null hypothesis used to calculate the p-values

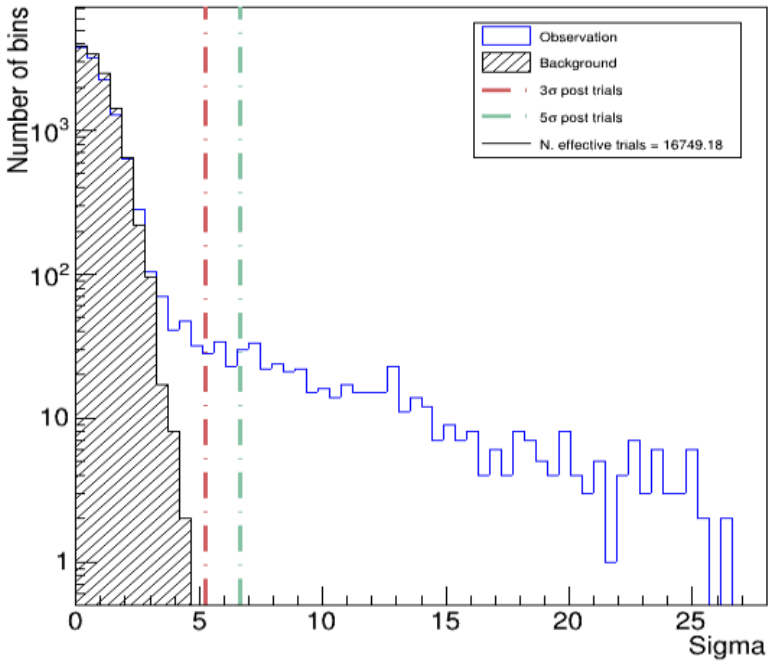

Figure 6.18: Pre-trial significance distributions from the results of the search algorithm done with a 100 s time window on one night of Mrk421 observations, during a flaring state. No cells containing VHE sources were excluded in this analysis. The red and green lines mark the 3σ and 5σ after-trials significances. The blue histogram contains the pre-trial significance of the excess of observed events in every window and cell of the RoI and the black histogram contains the pre-trials significance of the simulated background events for the same time windows and cells.

of observed events. In the case of Poisson fluctuations, the significance distribution should follow a Gaussian function with mean equal to 0 and standard deviation equal to 1.

In fig. 6.22 we plot the two distributions (the one obtained from observed events and the one obtained from simulated events) into two separate histograms for better visualization and characterize them independently. We fit each distribution to a Gaussian function and directly obtain their mean and RMS in case the fit is not good, which can be caused by a lack of statistics. In the right panel of fig. 6.22, which shows the characterization of the distribution resulting from simulated events, the obtained values for mean and standard deviation are those expected from Poisson fluctuations, whereas the left panel shows a larger standard deviation of ~ 1.1.

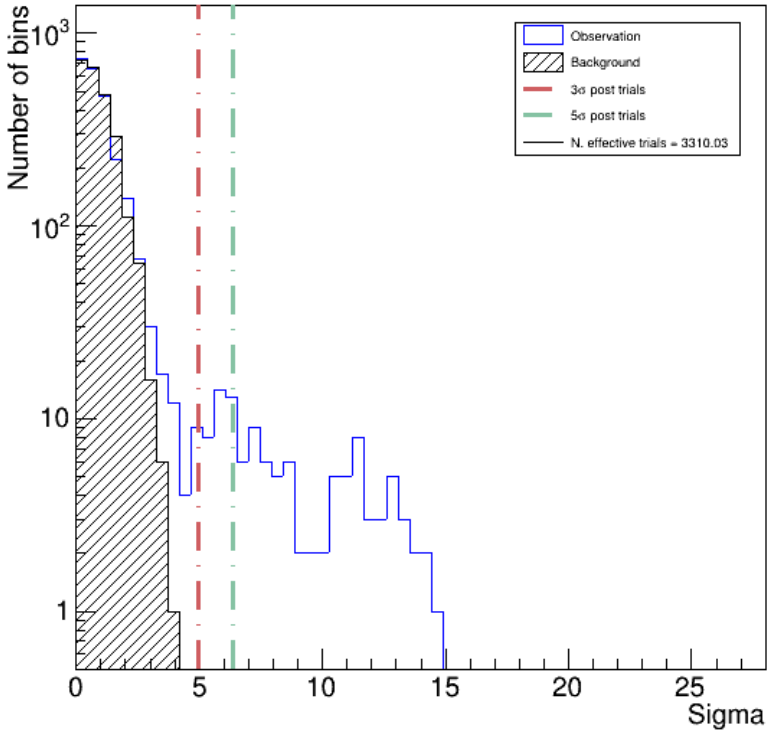

Figure 6.19: Pre-trial significance distributions from the results of the search algorithm done with a 100 s time window on one night of Mrk421 observations, during a low state. No cells containing VHE sources were excluded in this analysis. The red and green lines mark the 3σ and 5σ after-trials significances. The blue histogram contains the pre-trial significance of the excess of observed events in every window and cell of the RoI and the black histogram contains the pre-trials significance of the simulated background events for the same time windows and cells.

We have used a variety of observations to characterize the systematic uncertainty of our background estimation model. These data were selected to cover all the Zd range of the analysis, to be from galactic and extragalactic FoVs and to have a variety of mean background detection rates among them. They were also selected from various periods of time to check for temporal evolution of the systematic effects.

The used FoVs are listed in table 6.1. The first four samples were used to determine how to generate simulated events that would have a significance distribution that reproduced the one obtained from the observed number of events in each time window and spatial cell in the investigated FoVs. We found

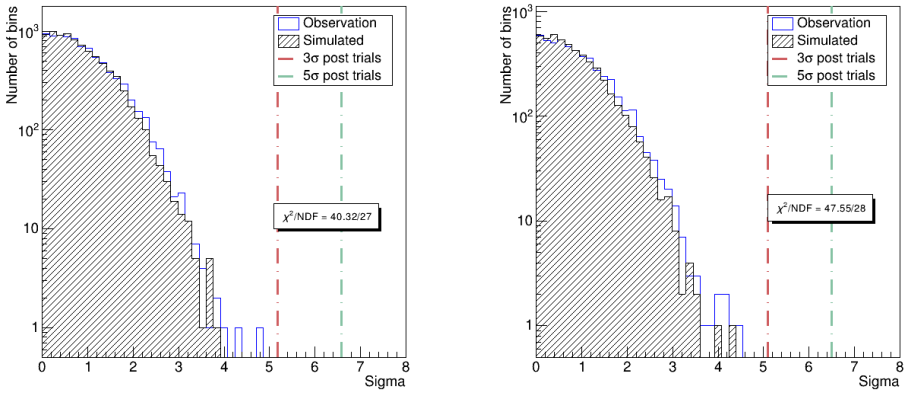

(a) $\Delta t = 200$s

(b) $\Delta t = 300$s

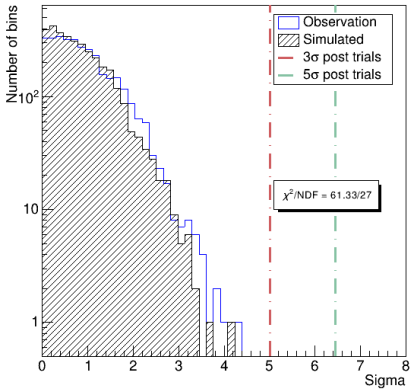

(c) $\Delta t = 400$s

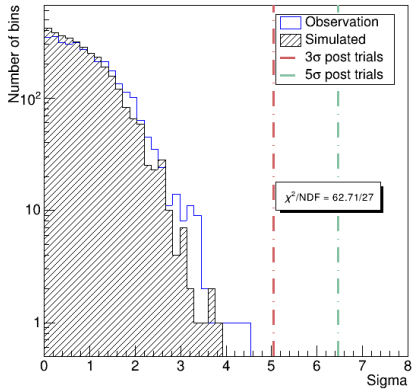

(d) $\Delta t = 500$s

Figure 6.20: Pre-trials significance distributions from the application of the search algorithm in time windows of 200 s, 300 s, 400 s and 500 s in 11.29 h of observations of the FoV around 3c454.3. The blue histogram becomes wider than the black histogram as Δt increases. The disparity between the two histograms in each plot is quantified by the χ^2/NDF.

(see appendix B for the description of the process and the tests performed) that adding a Gaussian convolution to the Poisson simulated events reproduced the significance distribution of observed events in the selected sample of observations. This can be seen in fig. 6.23, where both distributions are in agreement and have a standard deviation larger than 1. The three last samples in table 6.1 were used to validate the applicability of this result to other FoVs.

Taking $B_{i,j}$ as the number of expected background events in cell i and time window j, we found that the model had an uncertainty of a 7.6% on $B_{i,j}$, with a Gaussian distribution (see appendix B). That is, the real number of ex-

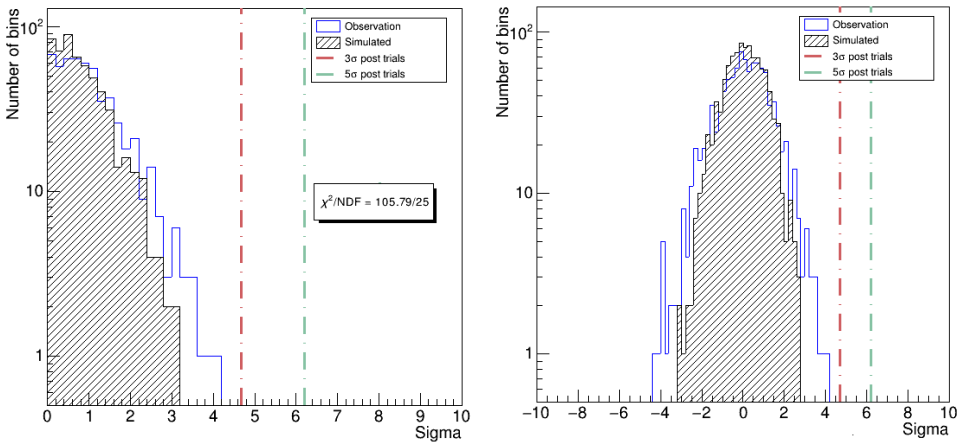

(a) Single-tailed distributions.

(b) Double-tailed distributions.

Figure 6.21: Pre-trials significance distributions from the 1000 s search window analysis on the FoV around 3c454.3. In both figures the blue line corresponds to the significance distribution from the observed events in the search algorithm and the shaded histogram corresponds to the significance distribution from simulated events. The red line marks the 3σ significance after trials and the green line marks the 5σ significance after trials. In *(a)*, we show the distributions obtained for the case of $N > B$ of the observed and of the simulated events, whereas in *(b)* we show the two-tailed distributions, with the positive significance side and the negative significance side that corresponds to $N \leq B$.

pected events of each cell i and time window j follows a Gaussian distribution around $B_{i,j}$ with a standard deviation equal to $0.076 B_{i,j}$.

When the number of detected events follows a Poisson distribution where the mean is not known exactly, it is not possible to obtain its p-value analytically. In principle, it could be calculated numerically by simulating a large enough sample of numbers following, in this case, a Gaussian distribution for each mean value of the Poisson distribution.

However, due to the large amount of data analysed in this project this method was deemed non-feasible in practice. Instead, we compute 3σ and 5σ significance thresholds for the p-values calculated with eq. (6.2). In order to do so, and as we detail in the next paragraphs, the fast simulations described earlier in section 6.2 are used to find a relation between the number of expected background events predicted by our model and the distribution of p-values obtained from the search.

To find that relation, we selected a sub-sample of observations from ta-

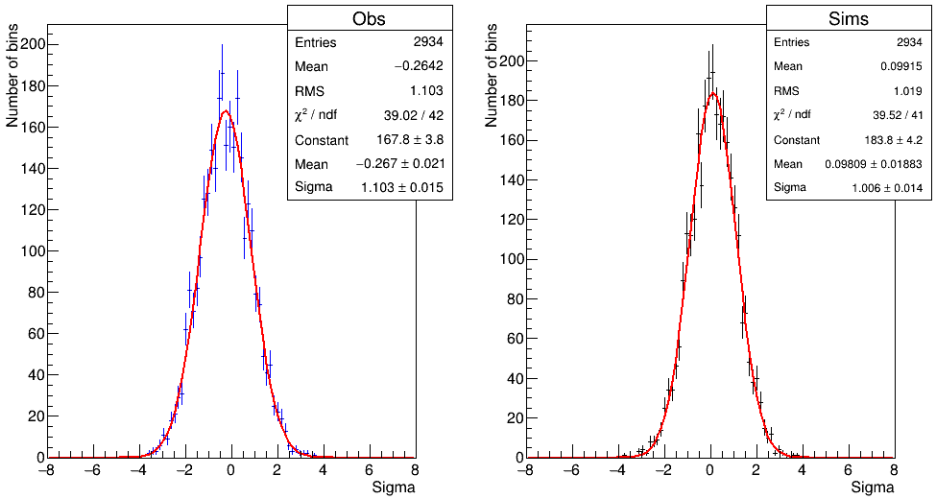

Figure 6.22: Pre-trials significance distributions from the 1000 s search window analysis on the FoV around 3c454.3. The left panel contains the significance distribution from the observed events in the search algorithm and the right panel contains the significance distribution from the simulated events. The red line in both panels corresponds to a Gaussian fit, the results of which are gathered in the upper-right box. Each box contains also the directly calculated mean and RMS of the distribution.

ble 6.1 where the estimated background had a different mean value, $\langle B_{i,j} \rangle$ (from all the spatial cells and time windows in each FoV). These corresponded to different nights of observation during September 2013. Additionally, individual cells were tested to check if the relations found for the p-value distribution from the analysis of whole FoVs could be applied them. The selected cells are included in the observations of the FoVs of 3c454.3, B1957+20 and TXS2320+343 for the time periods listed in table 6.1.

The small size of the spatial cells prevented us from performing the simulations and tests directly on them due to lack of statistics. Moreover, the projection of a cell in the camera plane is time dependent, which can result in the distribution of the B_j of that cell to have a large variance (the order of $\langle B_j \rangle$) due to camera acceptance differences. When analysing all the gathered cell results from a FoV, this variation is averaged among all the cells and the distribution of $B_{i,j}$ is narrower around $\langle B_{i,j} \rangle$, providing more stable test results.

We applied the search algorithm onto the selected sample using different time windows. The effect of the systematic uncertainty of our background model on the distribution of p-values and significance is maximum for time

Source	Period	Zd [deg]
3c454.3	September 2013	12 - 35
3c454.3	June 2014	31 - 44
B1957+20	September 2013	10 - 50
Cyg-X3	May 2014	15 - 40
3c454.3	October 2013	11 - 41
G24.7+0.6	April 2014	36 - 38
TXS2320+343	November 2013	7 - 10

Table 6.1: Data used to calculate (first 4 rows) and to check (last 3 rows) the systematic uncertainty of the background estimation model.

windows of $1000\,\mathrm{s}$ (for our case, since that is the longest time window duration that is used in this project), whereas it is not easily quantifiable in other time windows used in this work, $10\,\mathrm{s}$ and $2\,\mathrm{s}$. Therefore, in order to compute the significance thresholds and check for any possible dependence with time window duration, the time windows applied to the observations were chosen to be $1000\,\mathrm{s}$, $500\,\mathrm{s}$, $100\,\mathrm{s}$ and $50\,\mathrm{s}$.

When applying the analysis on each cell's light curve of observed events, we used the predicted B_j to generate a large amount of numbers, $N_{\mathrm{sims}} \sim 10^3$, with a Gaussian distribution with $\mu_{\mathrm{sims}} = B_j$ and $\sigma_{\mathrm{sims}} = 0.076 B_j$. Each one of those numbers was then used to simulate a new Poisson distributed number, that is compared with the original B_j to obtain its p-value.

For easier visualization, the resulting p-values are shown in a $\log_{10}$ scale histogram, as $\epsilon \log_{10}(p)$. If the generated number is larger than B_j, its p-value is computed as eq. (6.2) and introduced to the histogram as $-\log_{10}(p)$, so the factor $\epsilon = -1$ in this case. Otherwise, the complement of eq. (6.2) is calculated, $1 - p$, and what is introduced to the histogram is $\log_{10}(1 - p)$, and $\epsilon = 1$.

In fig. 6.24 we show one of the fast-simulation tests done to obtain the relation between the distribution of p-values and the mean number of expected background events $\langle B_{i,j} \rangle$ in all the spatial cells and time windows in the FoV of a galactic source. The right tail of the histogram can be fitted to an exponential function. This allows us to calculate the p-value of the distribution of $\epsilon \log_{10}(p)$ with the cumulative distribution of the exponential function, $F(x; \lambda) = 1 - e^{-\lambda x}$.

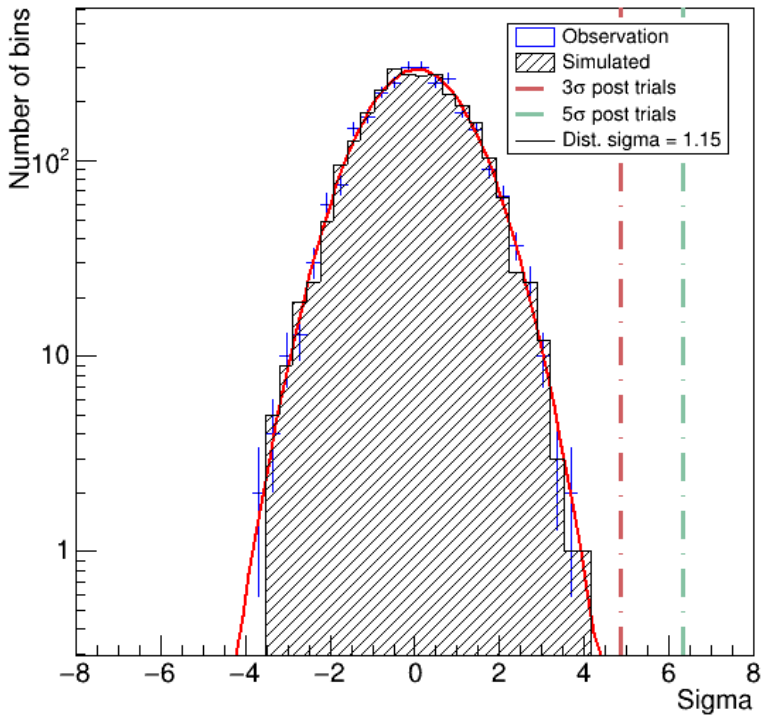

Figure 6.23: Pre-trials significance distributions from the 1000 s search window analysis over 11.08 h of observations around 3c454.3 taken on October 2013. The blue dots correspond to the significance distribution from the observed events in the search algorithm. The shaded histogram corresponds to the significance distribution from simulated events, now with the convolution of the Gaussian distribution. The solid red line marks the Gaussian fit to the distribution of observed results and has a width >1 as expected.

To obtain a 3σ threshold, we can simply calculate the p-value that is needed for that significance given the number of effective trials in the search, following eq. (6.4), which we call p_3, and set $1-p_3 = 1-e^{-\lambda x}$. Setting $-\lambda = s$, the slope obtained from the fit of the distribution, and solving for x which is, in turn, $\log_{10}(p)$, we have an estimation of the p-value needed for a 3σ significance corrected for the systematic uncertainty of the background model:

$$\log_{10}(p_3') = \log(p_3)/s\,, \tag{6.5}$$

We tested the variation of s with the mean number of expected background events by applying the search algorithm to individual cells with different

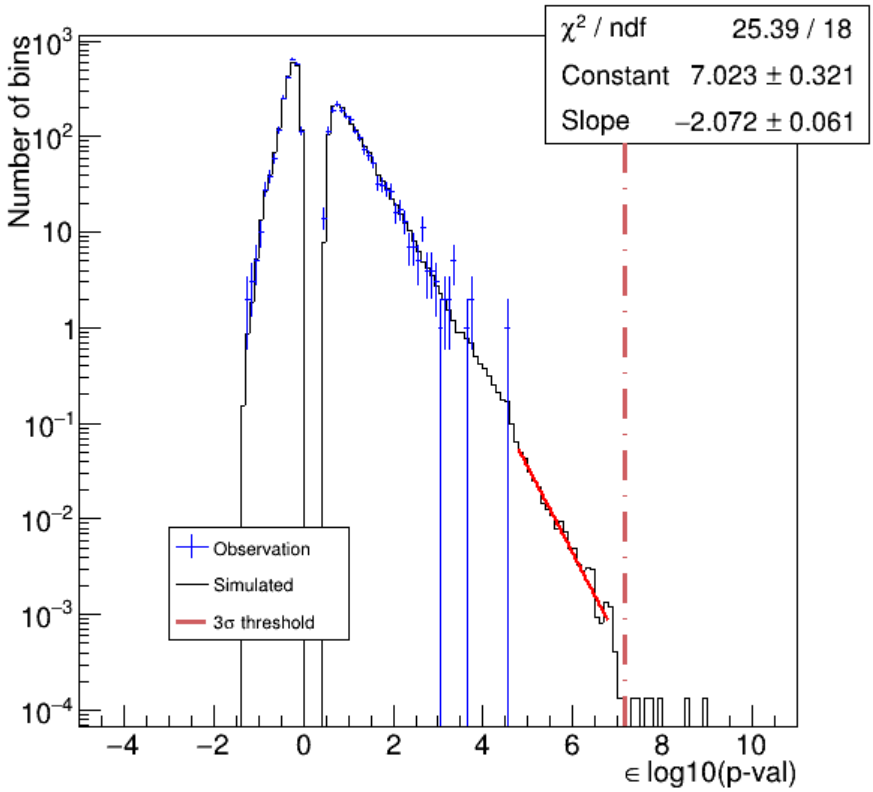

Figure 6.24: Test for the application of the systematic uncertainty of the model to obtain the flare detection 3σ and 5σ thresholds. The blue dots correspond to the analysis results over 1 h of observations around 3c454.3 taken on September 2013. The black histogram corresponds to the simulated results of the convolution of a Gaussian distribution with a Poisson distribution, normalized to the blue histogram. The red solid line corresponds to the exponential fit and the red dashed line corresponds to the 3σ threshold level calculated via eq. (6.5).

$\langle B_j \rangle$ as well as to whole FoVs with different $\langle B_{i,j} \rangle$, for the selected time windows. The result of these simulations and tests are gathered in fig. 6.26, where a linear fit to the points shows that the relation between the slope of the simulated p-values and the mean expected number of events in a cell can be expressed by $s = 2.233 - 0.009 \langle B_j \rangle$.

Therefore, this simple relation can be used as an approximate signal threshold when analysing the large amount of cells in the project, as opposed to generating millions of simulated numbers for each cell. If any cell during the run of the analysis over the whole period contained a window where the p-value was equal or smaller than p'_3, it was investigated further.

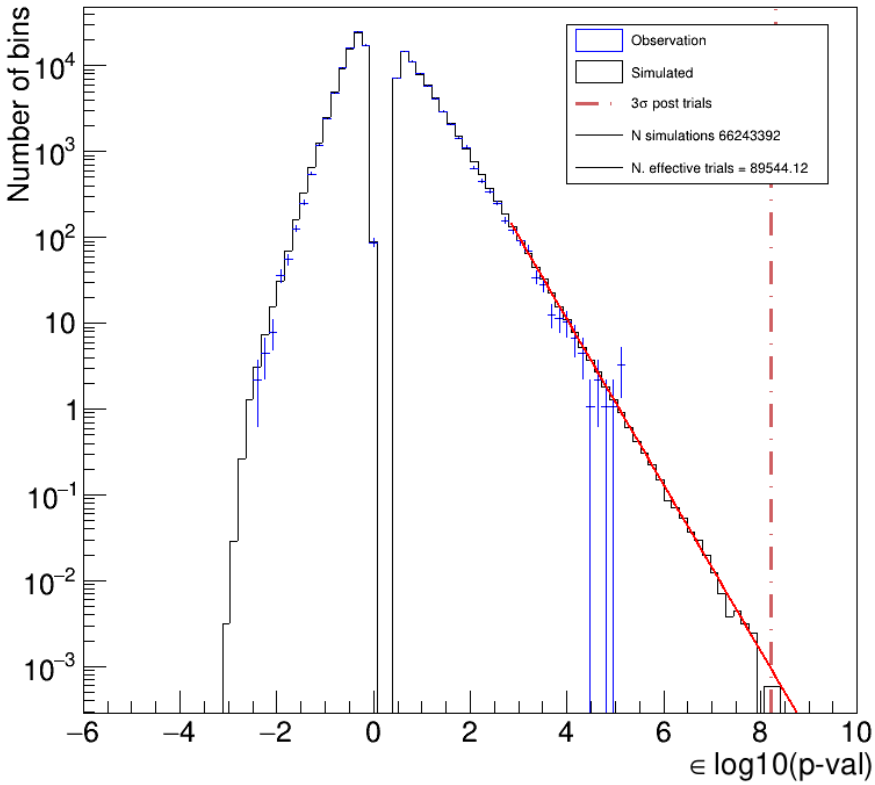

Figure 6.25: Test for the application of the systematic uncertainty of the model to obtain the flare detection 3σ and 5σ thresholds. The blue dots correspond to the analysis results over 19 h of observations around B1957+20 taken on September 2013. The black histogram corresponds to the simulated results of the convolution of a Gaussian distribution with a Poisson distribution, normalized to the blue histogram. The red solid line corresponds to the extrapolation of the exponential fit and the red dashed line corresponds to the 3σ threshold level calculated via eq. (6.5).

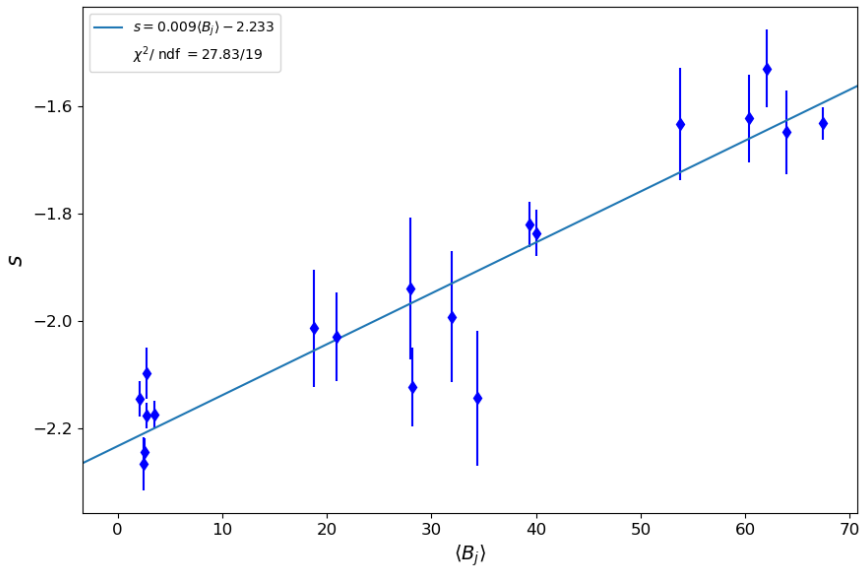

Figure 6.26: Relation between the slope of the fits to the simulated p-values and the mean number of expected events.

Chapter 7

Results

In this chapter we present the results from the unbiased archival search of transient sources, performed on data from the MAGIC IACTs, for the timescales of 2, 10, 100 and 1000 s. We report new upper limits to the number of flares from transient gamma-ray sources and to the evaporation rate density of PBHs on parsec scales. We have developed a blind search algorithm to search for bursts of gamma-ray photons in archival data within the MAGIC software framework and applied it to approximately a year of stereo observations processed following the descriptions in section 3.3.

In section 7.1 the data set is described in depth. Section 7.2 presents the best candidates for transient VHE signals found in the analysis of the different time windows. No flare candidate was found to have a high enough significance (after considering trials) to claim a detection, they are consistent with background fluctuations. In section 7.3 we describe the process of obtaining upper limits after a null detection for the transient investigated in this work. Finally we place upper limits to the number of flares from transient sources as a function of their flux and to the density of local PBH evaporations per year in the vicinity of the Earth.

7.1 Data set

The data set used in this work consists of the stereo observations performed by the MAGIC telescopes from 2013/07/27 to 2014/06/18 and from 2014/07/05 to 2014/08/05. This stretch of time corresponds to a single analysis period of

MAGIC, that is, when the state of the telescopes remains stable enough so that their response can be reasonably described (and hence all the collected data can be analysed) with a single MC production, part of which was used to create the background model, as described in chapter 5. The choice of this set of observations in particular arises from the pre-existence of an already created and validated set of RF and LUTs for the given MC period ST.03.03. The creation and validation process of the products derived from the MC simulation is not trivial and it is usually assigned to a dedicated taskforce within the MAGIC telescopes collaboration. The data from this period was considered to be enough for a proof of concept of the transient search method, without the need to spend valuable time and resources on validating the MC simulations for another period.

The total number of runs in period ST.03.03, according to the MAGIC database, is 9290, including test runs, moon time, mono observations and others. After selecting only stereo, non-test, low NSB runs, the available number of runs is reduced to 3730, which amounts to 1089 h of observations. Figure 7.1 shows a breakdown of all the runs in the period with the percentage of run types by their usability in the transient search algorithm developed in this work.

The breakdown in number of runs is a rough estimate of the final amount of data analysed, as some runs are accounted for completely, but contain some events over the Zd threshold or some events that were detected under moon conditions. In order to obtain as much live time as possible, we do not discard those runs entirely. In turn, we add a maximum Zd condition and a maximum brightness condition to remove moon data at the same time that we apply the data quality cuts to guarantee reliable results.

To select only time with dark conditions or no moon, we applied a cut on the mean current of the telescopes PMTs, $\mathrm{DC} < 2\mu\mathrm{A}$ (Aleksić et al. 2015b). The Zd selection cut was chosen by selecting observations with $\mathrm{Zd} \leq 50°$ and be able to analyse all the data with the background model described in chapter 5. In this work we applied the standard quality cuts on event rate and atmospheric transmission (see section 3.3.4). Data were rejected if the rate of events differed $\pm 15\,\%$ from the mean rate, if the atmospheric transmission value measured by the LIDAR was below $75\,\%$ or, in the absence of LIDAR data, if the cloudiness parameter measured by the pyrometer was above $40\,\%$. Along with the observation cuts, individual events were excluded from the analysis if their Hillas size was lower than 50.

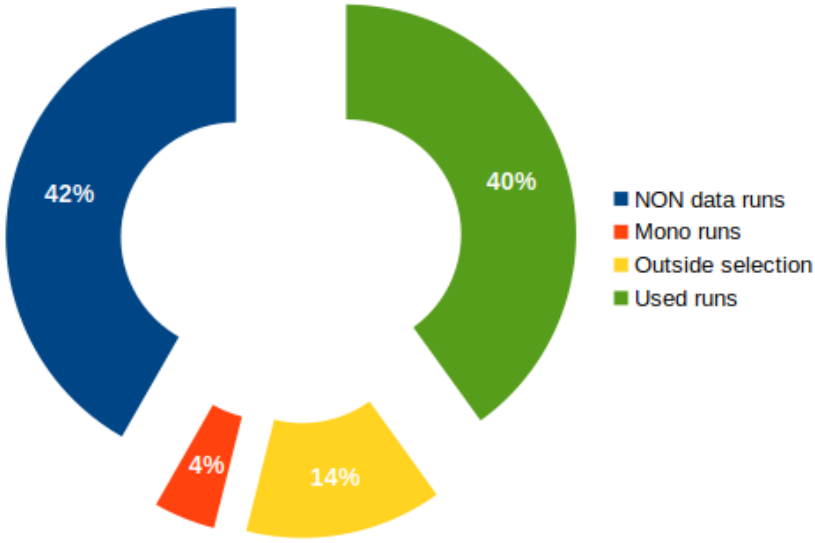

Figure 7.1: Pie chart portraying the distribution of the 9290 runs taken over the 359 days of the duration of period ST.03.03. The majority of files contained test and various types of calibration data (42 %). A small percentage of observations were performed with a single telescope (4 %). Another larger percentage of runs were outside of our requirements of Zd or moon conditions (14 %). Finally, 40 % of the runs were within our parameters and could be used for the search.

The resulting live time after all the selection and quality cuts is 973.3 h for the search of 2, 10 and 100 s bursts. Some runs are shorter than the 1000 s window, and are excluded from that search, which results in a shorter live time of 811 h for the analysis of that time window.

7.2 Signal candidates

To look for VHE transient events in the data, we first consider the trials of each cell individually. That is, all the time windows explored for a given spatial cell during approximately a year (the duration of the period we are investigating) are taken as the number of trials for that cell c and the number of effective trials per cell is $N_{\mathrm{eff,c}} = N_{\mathrm{windows,c}} \times 0.87$. If any trial-corrected p-value in that cell, when corrected for the systematic uncertainties of the background model according to eq. (6.4) and eq. (6.5), is equal to or lower than the selected significance threshold (3σ in this case), the cell is investigated further. The coordinates and size of the cell are used to check for coincidences with already known astronomical

sources in any wavelength.

Afterwards, the number of effective trials in the whole analysis ($N_{\text{eff}} = N_{\text{windows}} \times N_{\text{cells}} \times 0.87 \times 0.93$, per timescale) is used to correct the observed p-values and check if any of them correspond to a 5σ significance, which would warrant a detection claim.

The best candidates for VHE transient event signals in the four timescales inspected are gathered in table 7.1. These candidates have a significantly small p-value when corrected by the number of trials within their cell, but when the total number of trials in the analysis is taken into account, their final probability is coherent with the null hypothesis (there are no transient events in the data). The remaining candidates, due to the large amount of them, are gathered with their most relevant characteristics in appendix C.

$\Delta t[s]$	p-value	$N_{\text{eff,c}}$	N_{eff}	Post-trial ($N_{\text{eff,c}}$) p-value	Post-trial (N_{eff}) p-value
2	4.6×10^{-11}	8.9×10^{4}	2.9×10^{8}	4.1×10^{-6}	1.1×10^{-2}
10	2.3×10^{-9}	2.9×10^{3}	5.8×10^{7}	6.5×10^{-6}	1.0×10^{-1}
100	1.2×10^{-10}	1.3×10^{3}	5.4×10^{6}	1.6×10^{-7}	5.4×10^{-4}
1000	3.0×10^{-6}	2.5×10^{1}	2.2×10^{5}	7.5×10^{-5}	4.6×10^{-1}

Table 7.1: List of the lowest observed p-values in the four timescales investigated, before and after correcting for the number of effective trials in all the analysis. The significant probabilities of these candidates become consistent with the background hypothesis when the total number of trials is accounted for.

The best candidate for a burst signal, be it from the evaporation of a PBH or from any other VHE transient, is found in a 100 s time window. Its details are shown in table 7.2.

Figure 7.2 shows the distribution of observed p-values from the analysis of cell 368 935, where two time windows have a significance over 3σ after correcting for the systematic uncertainties of the background model and the number of trials in that cell. In fig. 7.3, the excess in observed events over the expected background can be seen in the zoomed-in region of the light curve of the cell. As seen in table 7.1, the candidate has a post-trials p-value higher than 2.87×10^{-7} (5σ equivalence).

100 s burst candidate	
Date	27/04/2014
Trigger time	03:47:42.01 UTC
Obs. Events	11
Bkg. Events	0.84
Cell index	368 935
Right Ascension	18 h 54′ 8.4375″
Declination	3° 34′ 59.958″
Zenith distance	39.5°

Table 7.2: Details from the VHE gamma-ray transient candidate in the 100 s search window.

Transient reports by other experiments were checked and no alarm was found near the location of this candidate at the time of its trigger. In addition, no variable or steady gamma-ray or x-ray source was found in the vicinity of the candidate coordinates when querying the Simbad database (Wenger et al. 2000).

7.3 Upper limits

Even though some transient signal candidates were found in the data, the large number of trials in the unbiased search rendered the excess in their number of detected events not significant enough to claim a detection. Yet, through the detection of known steady and variable gamma-ray sources (see section 6.2.2) we have proved the detection capabilities of the search method developed in this work. Therefore, we can compute upper limits on the flux of the general population of transients and, particularly, on the evaporation rate density of PBHs in the vicinity of the Earth. First we describe the process to obtain the general upper limits and then the PBH upper limits.

7.3.1 General

The unbiased search allows us to calculate general upper limits on the number of flares originating from any kind of transient phenomena based on their integral flux and assumed energy emission spectrum.

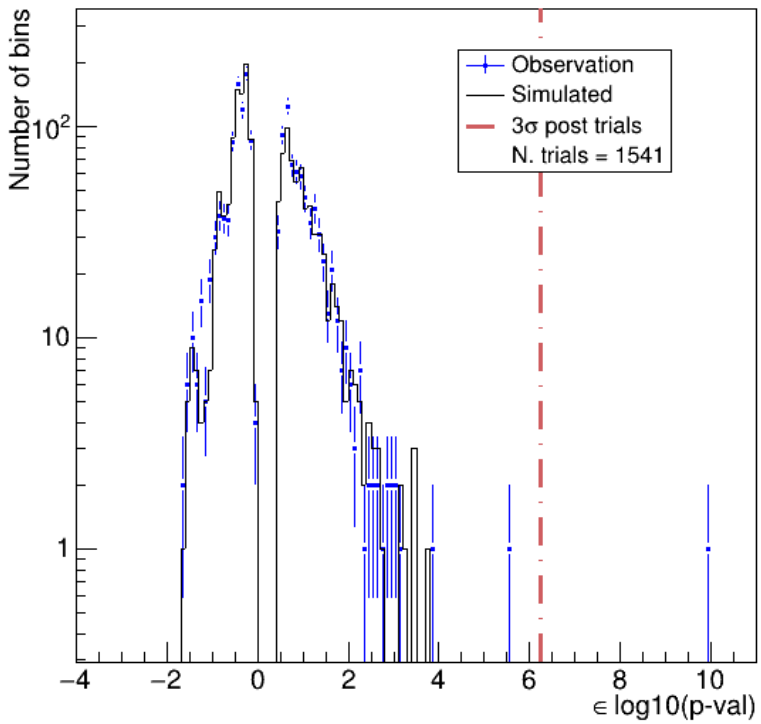

Figure 7.2: Distribution of observed p-values (times ϵ) in cell 368 935, which contains the best transient candidate in the analysis. The ϵ factor is -1 when the number of observed events is larger or equal than the number of expected background events and 1 in the opposite case. The red dashed line corresponds to the 3σ equivalence of p-values after correcting for $N_{\text{eff},368935} = 1341.54$ trials and the systematic uncertainties of the background estimation model. Events to the right of the red line have more than a 3σ significance after corrections.

The integral flux above a given energy E_0 is defined as

$$F_{>E_0} \equiv \int_{E_0}^{\infty} dE \frac{d\phi}{dE}\,, \tag{7.1}$$

where ϕ is the flux of the source ($\text{photons}\,\text{cm}^{-2}\text{s}^{-1}$). We set $E_0 = 200\text{GeV}$, which is in the range for both low and medium Zd observations.

We assume that the energy spectrum of the given transient source follows a power-law function,

$$\frac{d\phi}{dE} = \phi_0 \left(\frac{E}{E_0}\right)^{-\Gamma}\,, \tag{7.2}$$

where Γ is the so-called photon index and ϕ_0 is the normalization factor. We

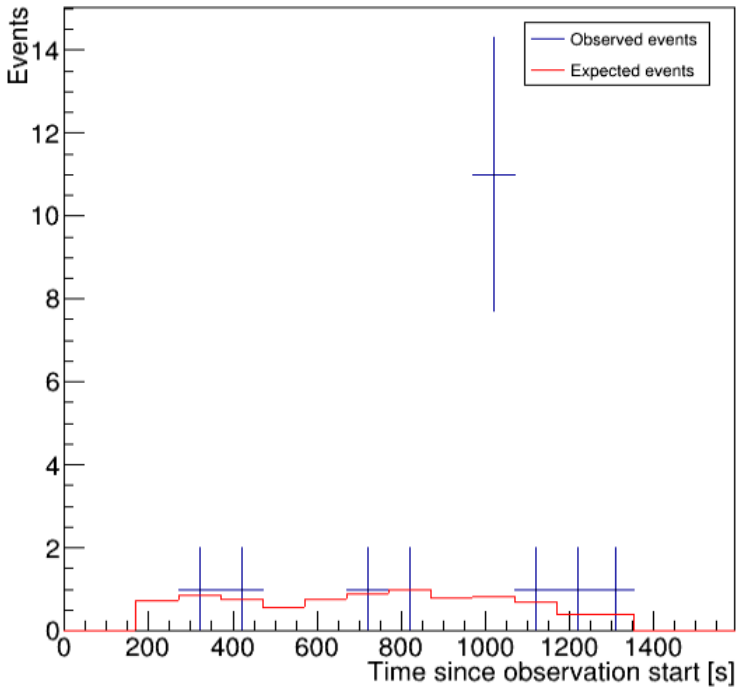

Figure 7.3: Light curve of event counts of the cell containing the best flare candidate, binned in 100 s time windows. The blue crosses mark the observed counts in each bin, while the red histogram marks the expected background counts in each light curve bin.

can calculate the normalization factor as a function of $F_{>E_0}$ if we substitute eq. (7.2) in eq. (7.1),

$$\begin{aligned} F_{>E_0} &= \int_{E_0}^{\infty} dE \phi_0 \left(\frac{E}{E_0}\right)^{-\Gamma} = \frac{\phi_0 E_0}{\Gamma - 1} \\ \phi_0 &= \frac{F_{>E_0}(\Gamma - 1)}{E_0} \,. \end{aligned} \tag{7.3}$$

By definition, the flux depends on the number of detected gamma-ray events. The expected number of gamma-ray events in a time window and cell is

$$g = \Delta t \int_0^{\infty} dE \frac{d\phi}{dE} \epsilon A_{\text{eff}}(E|\Delta\hat{E}, \text{Zd}) \,, \tag{7.4}$$

where E is the true energy of the gamma-ray and $\hat{E}$ its estimated energy.

$A_{\text{eff}}(E|\Delta\hat{E}, \text{Zd})$ is the effective area of a reference cell located at $0.4°$ off of the camera centre after all cuts, including the reconstructed energy cuts (see table 5.1 in chapter 5), and here ϵ is the mean relative acceptance of the cell we are observing with respect to such reference. ϵ is calculated as $\langle\epsilon_{\text{c}}\rangle$ / $\langle\epsilon_{\text{ref}}\rangle$, where the numerator and denominator are the average acceptance of the camera in the cell and in the reference cell respectively, according to the background estimation model (see section 5.2). $\langle\epsilon_{\text{c}}\rangle$ corresponds to the sum in eq. (5.7) for the investigated cell, averaged over the duration of the time window, while ϵ_{ref} corresponds to the sum in the same equation, but for a cell located at $0.4°$ from the camera centre. To minimize the effects of any possible inhomogeneity in the acceptance maps used to calculate ϵ_{ref}, we calculate it for 50 different camera coordinates and use their average value, $\langle\epsilon_{\text{ref}}\rangle$.

The effective area is obtained from the *ringwobble* MC simulations (see section 3.3.5) for the same period as the MC simulations used for the background model. The same *hadronness*, estimated energy and arrival direction cuts are applied, while taking all the true energy range of the simulations. This is shown in fig. 7.4 in discrete bands due to its Zd dependence.

Substituting eq. (7.2) and eq. (7.3) into eq. (7.4), we have

$$\begin{aligned} g &= \Delta t \int_0^\infty dE \frac{F_{>E_0}(\Gamma-1)}{E_0^{-\Gamma+1}} E^{-\Gamma} \epsilon A_{\text{eff}}(E|\Delta\hat{E}, \text{Zd}) \\ &= F_{>E_0} \frac{\Delta t(\Gamma-1)}{E_0^{-\Gamma+1}} \int_0^\infty dE E^{-\Gamma} \epsilon A_{\text{eff}}(E|\Delta\hat{E}, \text{Zd}) \,. \end{aligned} \tag{7.5}$$

Therefore, the flux upper limit on a certain time window and spatial cell is

$$F^{\text{UL}}_{>E_0} = \frac{g^{\text{UL}} E_0^{-\Gamma+1}}{\Delta t \epsilon (\Gamma-1) \int_0^\infty dE E^{-\Gamma} A_{\text{eff}}(E|\Delta\hat{E}, Zd)} \,. \tag{7.6}$$

We calculate the $95\,\%$ Confidence Level (CL) upper limits on the number of gamma-ray events, g^{UL}, for each spatial cell and time window following Feldman et al. (1998). In this method, the mean of the Poisson distribution is set to the number of expected background events in that spatial cell and time window predicted by the background model (see chapter 5).

In order to obtain the upper limits to the number of flares, we consider the minimum and maximum $F^{\text{UL}}_{>E_0}$ out of all the analysed cells and time windows

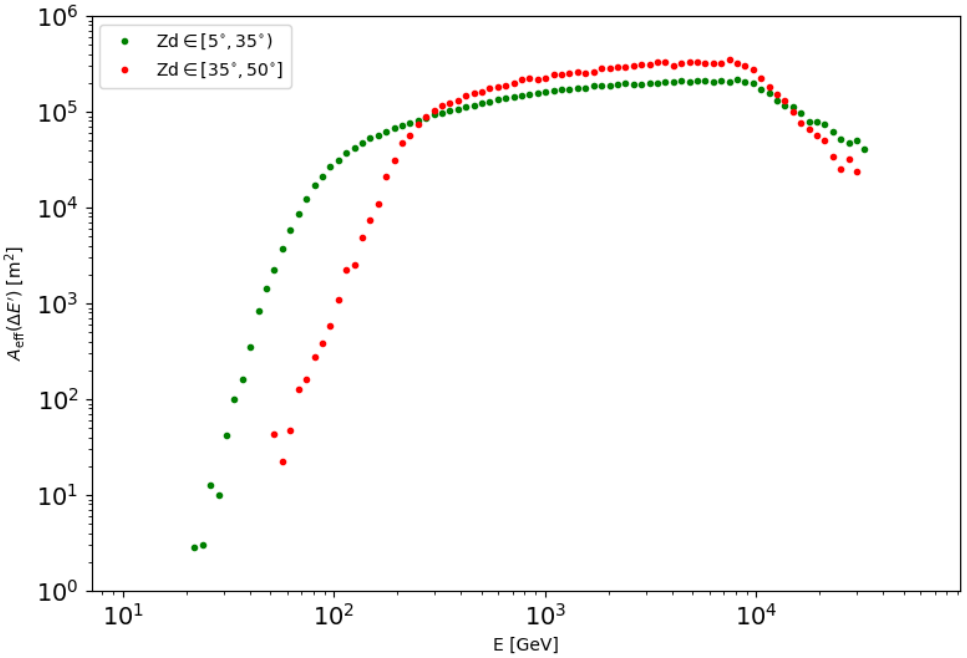

Figure 7.4: The effective area of the MAGIC telescopes for sources at a $0.4°$ offset from the pointing direction, as a function of the true energy E of the detected photons and excluding photons with estimated energies outside the $\Delta\hat{E}$ bin. Green dots correspond to the low Zd range and the orange dots correspond to the medium Zd range.

and define 20 evenly spaced (in $\log_{10}$ scale) flux values F_i between them. For each F_i, all the cells and time windows for which $F^{\text{UL}}_{>E_0} \leq F_i$ are considered. Then, we calculate the $95\,\%$ CL upper limit to the number of detected flares of flux F_i or lower ($n^{\text{UL}}_{\text{detected}}(F_i)$) following Feldman and Cousins, where the expected value is 2.5×10^{-2} and the observed value is the number of flares seen up to F_i with an associated p-value (after-trials) below 2.5×10^{-2}.

Assuming an isotropic distribution of the transient sources, the upper limit to the number of flares per year in the whole sky, of flux F_i or lower is

$$N^{\text{UL}}_{\text{flare}}(F_i) = \frac{n^{\text{UL}}_{\text{detected}}(F_i)}{f_{\text{sky}} T_{\text{eff}} \text{CDF}(F_i)}\,, \tag{7.7}$$

where f_{sky} is the fraction of sky corresponding to the FoV of MAGIC, T_{eff} is the effective time of the search and $\text{CDF}(F_i)$ is the CDF of the flux distribution, evaluated at F_i. For the RoI chosen in this work (see section 5.2), $f_{\text{sky}} = (1 - \cos(2.44 \times 10^{-2}))/2$.

We applied the search algorithm with time windows of 2 s, 10 s, 100 s and 1000 s and assumed four different photon indexes $\Gamma = 2.0$, $\Gamma = 2.5$, $\Gamma = 3.0$ and $\Gamma = 3.5$, to calculate upper limits on the integral flux of transient sources. The upper limits on the number of flares per year as a function of their flux are shown in fig. 7.5, where the integral flux of the Crab Nebula is added for comparison.

The features visible for $\Delta t = 2\text{s}$ and $\Delta t = 100\text{s}$ (for $\Gamma = 2.0$) are produced by individual flares with p-value after trial correction below 2.5×10^{-2}.

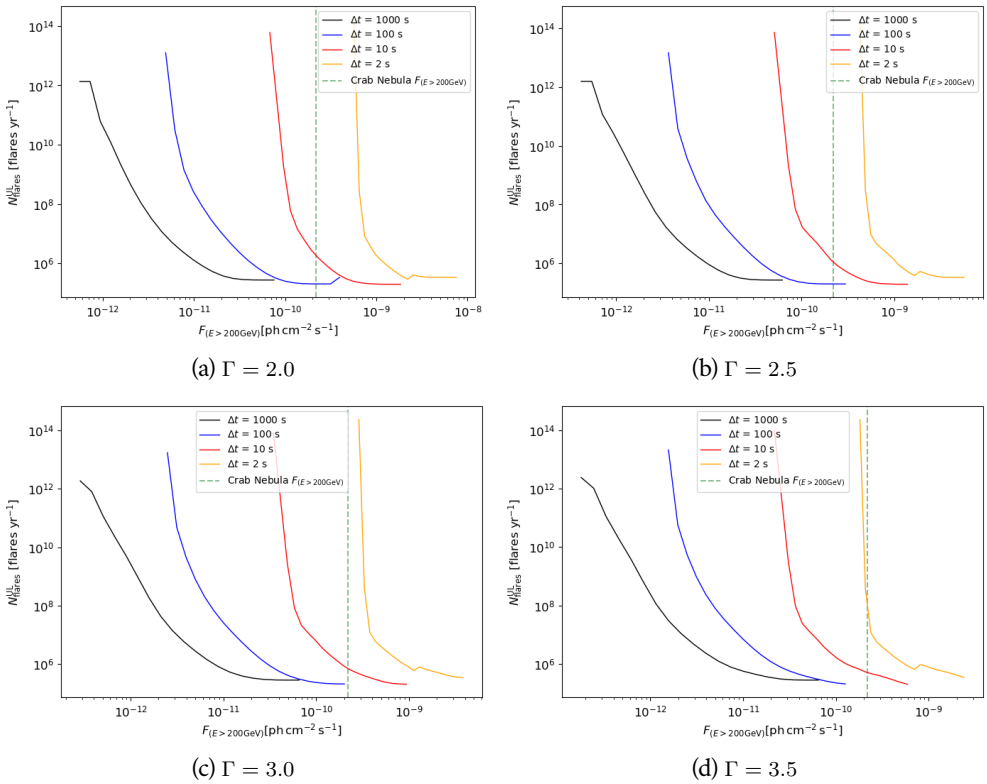

(a) $\Gamma = 2.0$ (b) $\Gamma = 2.5$

(c) $\Gamma = 3.0$ (d) $\Gamma = 3.5$

Figure 7.5: 95 % CL upper limits on the number of transient flares per year as a function of their integral flux above $E_0 = 200\text{GeV}$ assuming power-law spectral shape with $\Gamma = 2.0$ *(a)*, $\Gamma = 2.5$ *(b)*, $\Gamma = 3.0$ *(c)*, $\Gamma = 3.5$ *(d)*. Each solid curve corresponds to one of the explored timescales. The dashed green line corresponds to the flux of the Crab Nebula integrated above the same energy.

7.3.2 Primordial black hole evaporation

The non-detection of a PBH evaporation signal is consistent with the current literature (Aharonian et al. 2023, Tešić et al. 2012, Abdo et al. 2014, Albert et al. 2020 and Ackermann et al. 2018) and the sensitivity of the MAGIC telescopes.

Nevertheless, a non-detection is also a valuable result which constrains the local population of PBHs and their relation with other dark matter candidates. With the results of the analysis, we can establish upper limits on the rate of occurrence of PBH evaporation bursts within the temporal scope of our dataset and cross check them with the upper limits obtained by other gamma-ray experiments.

The method used in this section is a modification of the one described in Ukwatta et al. (2016) to calculate the evaporation rate density of PBHs in an unbiased direct search. Here, we take into account the specific detector properties of MAGIC, such as its effective area and energy resolution, as well as the intricacies introduced by the spatial and temporal binning (cells and time windows) used in this particular analysis.

In order to calculate the evaporation rate density, we need to estimate the effective volume of PBH detection for our detector. For a given cell and time window, the expected number of gamma-rays detected by MAGIC from a PBH burst of duration τ located at a non-cosmological distance r and zenith angle Zd is

$$\mu(r, \mathrm{Zd}, \tau, \epsilon) = \frac{1}{4\pi r^2} \int_0^\infty dE \frac{dN(\tau)}{dE} \epsilon A_{\mathrm{eff}}(E|\Delta\hat{E}, \mathrm{Zd}) \,. \tag{7.8}$$

where $\frac{dN(\tau)}{dE}$ is the PBH photon emission energy spectrum integrated from a remaining lifetime of $t = \tau$ to $t = 0$ (see eq. (1.17)) and we assume that our time windows are chosen to last $\Delta t = \tau$ and end at $t = 0$. The rest of variables in the equation are the same as in eq. (7.4).

The maximum distance up to which a PBH can be detected by MAGIC is obtained by equating $\mu(r, \mathrm{Zd}, \tau)$ to the minimum number of expected signal counts, μ_0, required for a statistically significant detection given our background counts, B (see eq. (6.1)), and solving for r. The value of μ_0 depends on the duration of the time window, on the position of the cell in the FoV and on the number of trials incurred on during the analysis. Additionally, to correctly calculate μ_0, we need to take into account fluctuations in the background and the signal.

Let n_0 be the number of detected counts with a probability smaller than $p_0 = 2.87 \times 10^{-7}$ (equivalent to 5σ significance) under the background-only hypothesis, after adjusting for the number of trials and the systematic uncertainties of the background model. Applying eq. (6.4) into eq. (6.5) (substituting p_3, the p-value equivalent to 3σ with p_0), the probability of n_0 must actually be smaller than

$$p_c = 10^{\log(1-(1-p_0)^{1/N_{\rm eff}})/(2.233-0.009B)}\,, \tag{7.9}$$

for each trial, where B is the number of background counts given by the background estimation model (see chapter 5) for a time window and spatial cell.

Since the detector counts measured in a given spatial cell and time window follow a Poisson distribution of mean B, n_0 can be determined from

$$p_c = P(n \geq n_0; B)\,, \tag{7.10}$$

where $P(n \geq n_0; B)$ denotes the Poisson probability of obtaining n_0 or more counts in a time window and cell when the Poisson mean is B. We approximate μ_0 by the signal that will, on average, produce the significance given by p_c, i.e. $\mu_0 = n_0(p_c) - B$.

By setting μ_0 equal to $\mu(r, \mathrm{Zd}, \tau)$, we obtain the average maximum distance from which a PBH burst can be detected by the MAGIC telescopes with the selected significance (5σ post-trial in our case) at a certain time window and spatial cell,

$$r_{\rm max}(\mathrm{Zd}, \tau, \epsilon) = \sqrt{\frac{1}{4\pi\mu_0}\int_0^\infty dE \frac{dN(\tau)}{dE}\epsilon A_{\rm eff}(E|\Delta\hat{E}, \mathrm{Zd})}\,. \tag{7.11}$$

ϵ, and therefore $r_{\rm max}$, are different for each observed cell, due to the camera acceptance not being uniform. Furthermore, the radius for a given cell can vary from time window to time window, since the projected position of a cell in the camera can change in short timescales. In fig. 7.6 we show the distribution of the $r_{\rm max}$ for all the considered trials, that is, for all time windows and spatial cells, of the four timescales used in the search.

The variety of $r_{\rm max}$ means that we must calculate the effective volume probed for each FoV in an observation (we assume that each time time window corresponds to a slightly different FoV). This is done by summing over the

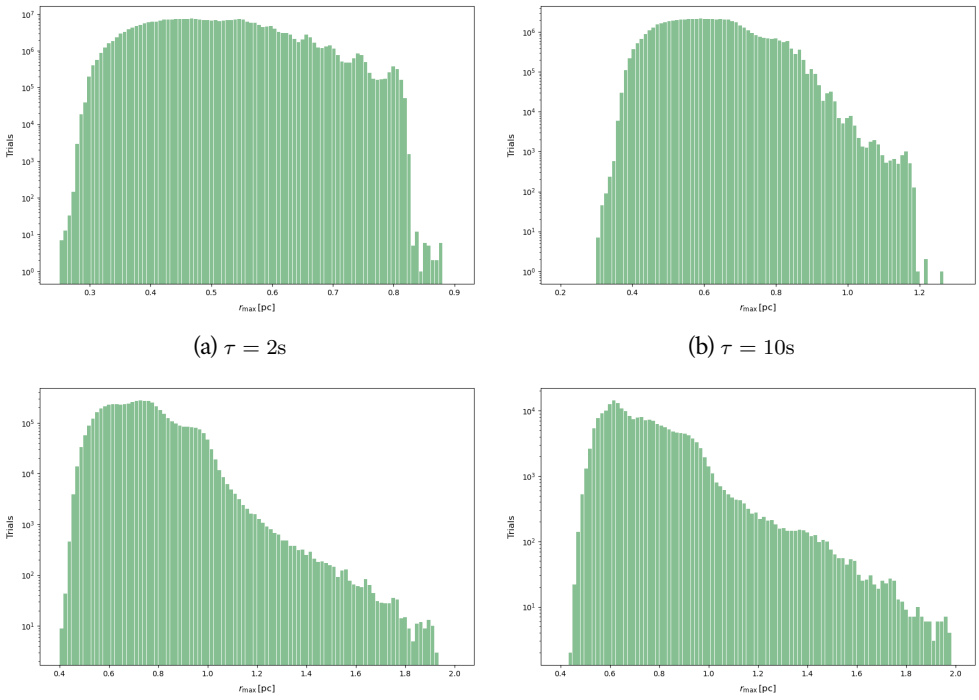

(a) $\tau = 2$s

(b) $\tau = 10$s

(c) $\tau = 100$s

(d) $\tau = 1000$s

Figure 7.6: Distribution of maximum PBH detection radius, $r_{\max}$, for all spatial cells and time windows. The different plots show the results for the search of a $\tau = 2$s PBH evaporation signal, *(a)*, a $\tau = 10$s signal, *(b)*, a $\tau = 100$s signal, *(c)*, and a $\tau = 1000$s signal, *(d)*.

volumes probed by each cell in the FoV,

$$V(\tau) = \frac{4\pi}{3} \sum_i r^3_{\max,i}(\tau) \frac{\Omega_c}{4\pi} \,, \tag{7.12}$$

where the index i goes over each cell visible within the RoI of an observation during the span of a time window, and Ω_c is the solid angle of the cell. The cells used in this work have a radius of $r_S = 0.15°$ and an overlap of $\sim 20\%$ in area, so we can provide a conservative estimation of the effective volume taking $\Omega_c = 2\pi(1 - \cos(2.34 \times 10^{-3}))$.

In fig. 7.7 we can see the distribution of volumes probed per FoV for the four timescales used in the search. In the volume distribution for the two longest time windows, some peaks can be clearly seen. The first peak in the distribution corresponds to low Zd observations, while the second peak corresponds

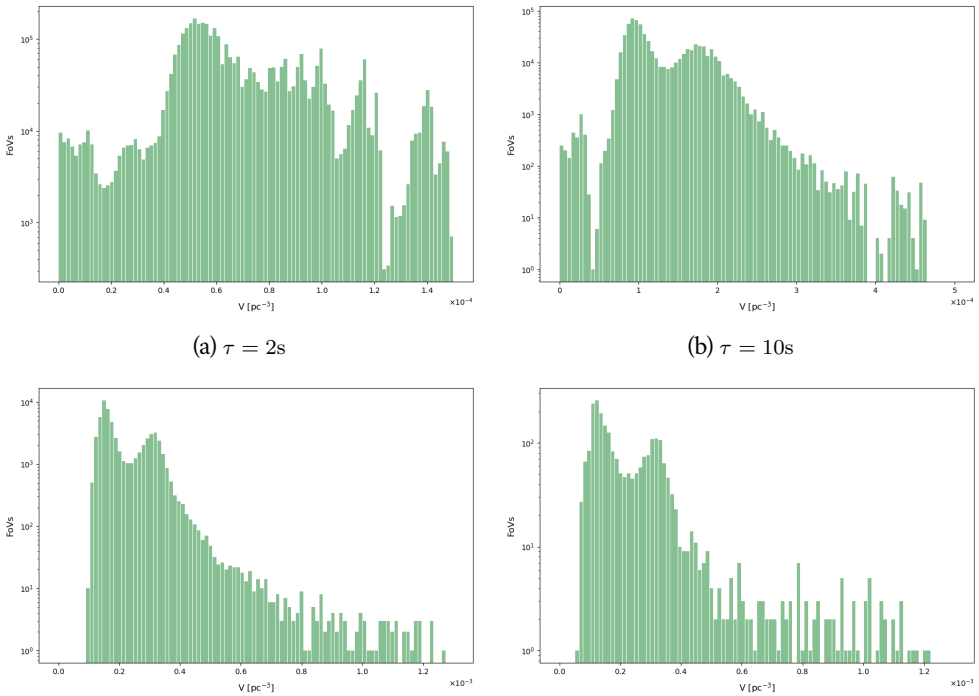

(a) $\tau = 2$s (b) $\tau = 10$s

(c) $\tau = 100$s (d) $\tau = 1000$s

Figure 7.7: Distribution of effective volumes obtained in the transient search analysis using time windows of 2 s, 10 s, 100 s and 1000 s. Each effective volume was calculated for the FoV observed during the span of a time window, for all the time windows probed during the period of observations.

to medium Zd observations. This is caused by the higher energy threshold imposed to medium Zd observations, which reduces the number of expected background events and increases the maximum detection radius of PBHs.

The volume distributions for the shortest time windows do not show a clear distinction between the results from low and medium Zd observations. This is due to the large amount of time windows and cells where no events where detected, $N = 0$, but for which the background expectation was small but not null, $0 < B < 1$.

We take the mean of each distribution in fig. 7.7 to calculate the upper limits on PBH evaporation rate. Using the mean of the effective volume distribution has the advantage of automatically taking into account the time spent on each of the Zd ranges.

Assuming a uniform distribution of PBHs in the solar neighbourhood, we can place an upper limit on the rate density of PBHs evaporations at a given CL X with

$$\dot{\rho}_{\mathrm{PBH}}^{\mathrm{UL}_X} = \frac{m}{\langle V \rangle T}\,, \tag{7.13}$$

where T is the total search duration in years, $\langle V \rangle$ is the mean effective volume of the search and m is the upper limit on the number of PBH bursts given that we have a null detection at the X CL. For Poisson fluctuations $P(0|m) = 1-X$ since we have seen 0 bursts, and so $m = \log(1/(1-X))$. Choosing a $X = 99\%$ CL, $m \approx 4.6$ and the upper limit on the PBH burst rate density is

$$\dot{\rho}_{\mathrm{PBH}}^{\mathrm{UL}_{99}} = \frac{4.6}{\langle V \rangle T}\,. \tag{7.14}$$

We applied the algorithm with time windows of 2 s, 10 s, 100 s and 1000 s to search for PBH evaporation signals. Some burst candidates were found in the data, but none of them had a significant excess of events (equal to or over 5σ after trial correction) over the expected background counts. Following the procedure laid out in section 7.3.2, we used this null detection to place 99% CL upper limits on the burst rate density of PBHs around the Earth.

We use the parametrization of the PBH emission spectrum by Petkov et al. (2008). We report these limits in table 7.3.

Burst duration (s)	UL_{99} ($10^5 \mathrm{pc}^{-3}\mathrm{yr}^{-1}$)
2	6.1
10	3.2
100	1.9
1000	2.1

Table 7.3: The 99% CL upper limits on the PBH rate density for the time windows searched.

7.3.3 Discussion

The results obtained are consistent with the upper limits reported by other gamma-ray experiments (see fig. 7.8) and add an upper limit to the evaporation density of PBHs in a timescale not investigated previously.

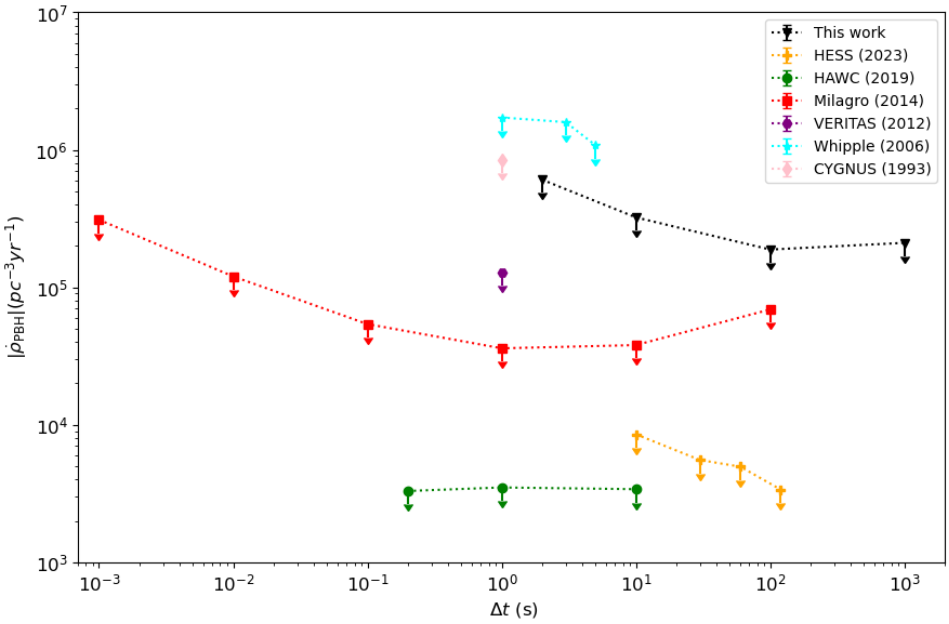

Figure 7.8: Upper limits on the PBH evaporation rate density measured with MAGIC data for burst timescales of 2 s, 10 s, 100 s and 1000 s. For comparison, the limits obtained by other experiments at the 99 % CL are also shown (Albert et al. 2020, Abdo et al. 2014, Tešić et al. 2012, Aharonian et al. 2023, Alexandreas et al. 1993 and Linton et al. 2006).

The current best limits are set by the water Cherenkov array HAWC, with three years of data investigated for PBH emission (Albert et al. 2020). The wide FoV and continuous operation of HAWC are advantageous for this search since the analysis depends on the total observation time and on the observable volume. However, the higher energy threshold of water Cherenkov arrays, when compared to IACTs, lowers the distance up to which they can detect PBH evaporation signals. For example, Albert et al. (2020) claim a $r_{\rm max} = 0.5{\rm pc}$, while the maximum radius obtained in this work is $r_{\rm max} \sim 2{\rm pc}$. Consequently, the parameter space probed in this work is different from that of other experiments with lower detection reach. Such is the case for H.E.S.S., which, within the IACT experiments, has the most constraining upper limits, resulting from the analysis of over 4816 h of observations (Aharonian et al. 2023), but where they claim to only be sensitive to PBH evaporation signals up to $r_{\rm max} = 0.1{\rm pc}$.

We have assumed, like the other experiments shown in fig. 7.8, the SEM of BH radiation with no photosphere or chromosphere present, since their ex-

istence is highly contended (MacGibbon et al. 2008) and would result in a suppression of the VHE component of the detected PBH spectrum (Heckler 1997).

As mentioned in section 1.1.1, there are various models for the PBH emission spectrum, with no single one being widely regarded as the best model over the rest. However, the measured signal from PBHs and, therefore, the upper limits set on their evaporation density, depends on what PBH photon spectrum prediction or parametrization is assumed.

To better compare our upper limits with the published results of other experiments, we chose to use the parametrization of Petkov et al. (2008), like they do in Albert et al. (2020), Tešić et al. (2012) or Aharonian et al. (2023). However, if we calculate the upper limits on the density of PBH evaporations with the new parametrization from Ukwatta et al. (2016), we obtain slightly less constraining upper limits. These upper limits can be seen in table 7.4. This is consistent with

Burst duration (s)	UL_{99} ($10^5 \mathrm{pc}^{-3}\mathrm{yr}^{-1}$)
2	11.9
10	6.5
100	4.0
1000	4.9

Table 7.4: 99% CL upper limits on the PBH rate density for the time windows searched using the predicted energy spectrum from Ukwatta et al. (2016).

the new parametrization including the contribution from directly emitted photons as well as the contribution from pion fragmentation. The main source of differences between the results obtained in this work and the ones reported by other experiments is, however, the type of search being done by each of them.

Even though a plot such as fig. 7.8 is the tool used by most gamma-ray experiments to portray their results, it can be misleading to the reader, as the methods used and the quantities measured by some of the experiments differ among each other. While the limits reported by MILAGRO (Abdo et al. 2014), CYGNUS (Alexandreas et al. 1993) and this work were obtained by a direct, unbiased search of individual high-significance (5σ) PBH evaporation signals, the limits reported by HAWC (Albert et al. 2020), Whipple (Linton et al. 2006), VERITAS (Tešić et al. 2012) and H.E.S.S (Aharonian et al. 2023) do not require the detection of individual bursts.

Generally, in the analysis conducted by these experiments, gamma-like events are grouped into clusters according to their arrival time and direction. These clusters are categorized by their size according to the number of gamma-like events they contain. A likelihood ratio analysis is then used to calculate the density of PBH evaporations by comparing the distribution of cluster sizes in the data with the one expected for the background. The sensitivity of this kind of study is dominated by the more abundant number of low-significance burst-like signals that should be produced by the evaporation of PBHs in the vicinity of the Earth.

This method is statistically robust and more sensitive by principle for producing upper limits than a direct search of individual PBHs, like the one our analysis is based on. However, the difference in the distribution of low-significance bursts is prone to be affected by the systematic uncertainties on the predictions for the null hypothesis (there are no PBH evaporations). Meanwhile, the high-significance positive detection of one or more bursts with the temporal and spectral characteristics expected from a PBH evaporation would constitute a powerful smoking gun for establishing PBHs as the origin of the detected emission. This would not be the case if we just statistically establish the presence of more low-significance burst-like signals than our expectations from pure background. In this sense, our analysis is optimized for a positive discovery rather than for establishing the most constraining upper limits by ignoring possible systematic uncertainties.

Performing a similar analysis with our data is not possible without heavily modifying the particular search algorithm and background estimation model developed in this work. As seen in section 6.3, we see deviations of the significance distribution of observed events from the significance distribution of background generated events, but these are conservatively attributed to the systematic uncertainties of the background model and corrected. This is necessary to accurately estimate the significance of an individual burst, but prevents us from basing our limit computation on the distribution of observed p-values.

The upper limits on the local evaporation rate obtained in this work can be used to constrain the current average density of PBHs in the Universe. That result allows us to estimate the fraction of Universe mass that collapsed into the PBHs at their time of formation.

Assuming that PBHs formed from scale-invariant initial density perturbations with a Gaussian distribution, the density of PBHs that would be created

with an initial mass M_i is (Halzen et al. 1991)

$$\frac{dn}{dM_i} = \frac{\mathcal{N}}{M_*}\left(\frac{M_i}{M_*}\right)^{-\beta}, \tag{7.15}$$

where $M_* \simeq (0.5-1)\times 10^{15}\mathrm{g}$ is the mass of a PBH with a lifetime equal to the age of the Universe ($t_0 = 13.772\times 10^9\mathrm{yr}$ from Bennett et al. (2013)), $\beta = 2.5$ for PBHs that formed in the radiation-dominated era (Halzen et al. 1991) and $\mathcal{N}$ is the initial number density of PBHs with mass M_*.

$\mathcal{N}$ is related to the present local mass density of PBHs, $\Omega^{\mathrm{loc}}_{\mathrm{PBH}}$, as

$$\mathcal{N} = (\beta-2)\Omega^{\mathrm{loc}}_{\mathrm{PBH}}\rho_{\mathrm{c}}/M_*\,, \tag{7.16}$$

where ρ_{c} is the critical cosmological density. From eq. (1.6) in section 1.1.1 we can relate the current rate of expiring PBHs, $\dot{\rho}_{\mathrm{PBH}}$, measured in this work to their initial number density as

$$\dot{\rho}_{\mathrm{PBH}} \simeq \frac{\alpha(M_*)}{M_*^3}\mathcal{N} \sim \frac{\mathcal{N}}{t_0}\,. \tag{7.17}$$

and obtain a constraint on the local mass density of PBHs. Using the best upper limits of $\dot{\rho}_{\mathrm{PBH}}$ from table 7.3 and the value of the Hubble constant measured by Bennett et al. (2013), $H_0 = 69.32\,\mathrm{km\,s^{-1}Mpc^{-1}}$, we have

$$\Omega^{\mathrm{loc}}_{\mathrm{PBH}} \leq 9.8\times 10^3\,. \tag{7.18}$$

PBHs are expected to have the gravitational properties of cold Dark Matter (DM) (Carr et al. 2020) and as such they should cluster in the Galaxy causing an enhanced local density compared to the average PBH density in the Universe.

Using the ratio between the known enhancement factor for DM near the Sun (Bovy et al. 2012) and the average DM density (Hinshaw et al. 2013), $k \sim 2.2\times 10^5$, we can obtain the limit on the average PBH density in the universe, Ω_{PBH}, as a product of k and the local density of PBHs:

$$\Omega_{\mathrm{PBH}} \leq 4.45\times 10^{-2}\,. \tag{7.19}$$

This limit is less constraining than those obtained from measurements of

the extragalactic and galactic gamma-ray backgrounds, $\Omega_{\mathrm{PBH}} \leq 7.0 \times 10^{-11}$ and $\Omega_{\mathrm{PBH}} \leq 2.6 \times 10^{-9}$ respectively (Carr et al. (2021) and the references therein), which are calculated by integrating the PBH evaporations inside the visible universe or inside our Galaxy halo and comparing them to the observed diffuse backgrounds. However, the scope of their analysis is on gigaparsec and kiloparsec scales, respectively, while our results are local and sensitive to individual PBH evaporation signals on less than a parsec.

7.4 Conclusions

In the work laid out in this thesis, we aimed to implement an innovative algorithm designed to search for transient VHE sources within archival data from the MAGIC telescopes. This investigation did not result in the identification of signals attributable to either PBH evaporation or other notable VHE transient events. In the absence of such detections we have obtained upper limits on the number of transient flares per year as a function of their integral flux. These general limits can be used to obtain the specific limits for a particular transient phenomenon when its energy spectrum is known. Additionally, we have established upper limits in previously unexplored parameter space on the local evaporation rate density of PBHs. These limits are consistent with the current literature and can be used to constrain the existing models of early Universe density fluctuations and PBH contributions to DM.

The novel background estimation model developed herein represents an addition to the methodological toolkit available for the analysis of IACT data and for the detection of VHE sources from any direction in the FoV of the telescopes. While direct detection of transient events remained elusive, the methodology developed was able to detect VHE sources such as the Crab Nebula and Mrk421 with over 5σ significance in time windows of $1000\,\mathrm{s}$ or less. Therefore, the techniques established here can be applied to future searches, potentially discovering new phenomena.

The comparative analysis with data from other experiments underscores the necessity for integrated, multi-wavelength approaches to astrophysical phenomena, highlighting both the challenges and potential strategies for future transient detection efforts. Furthermore, this research has discussed theoretical implications regarding the PBH evaporation mechanisms and their observable signatures in the VHE range. By providing upper limits on the rate density of

local PBH evaporations, this work constrains several key parameters of cosmological models concerning the early Universe and the nature of DM. These findings underscore the importance of continuous, methodical searches for transient phenomena and the refinement of detection algorithms to improve sensitivity and specificity.

In conclusion, while the specific phenomena of interest were not detected during this work, the methodologies developed and the limits established have implications for both the theoretical understanding and empirical investigation of the VHE Universe. This study contributes to a more efficient use of the observational data of IACTs and sets the stage for future research that may reveal elusive signals hidden within archival data.

Appendix A

Gamma-ray acceptance of the MAGIC telescopes with Montecarlo simulations

A.1 Validation of the use of Monte Carlo events

We wanted to use simulated gamma-ray events from the standard MC productions of MAGIC instead of OFF data to build the background estimation model used in the transient search algorithm. This way we would be able to investigate most of the observation hours corresponding to a MC production period, instead of using a fraction of them on the model. We consider OFF data the observations of sources (OFF sources) where no significant gamma-ray signal was seen by standard analysis, plus the dedicated observations of dark regions of the sky. To make sure we could use MC simulations, we reproduced the rotation analysis from Prandini et al. 2016 and the instrument acceptance study of Da Vela et al. 2018 with the standard MC *diffuse* simulations of MAGIC for period ST.03.03.

First of all, we checked that the acceptance maps obtained with simulated events had an ellipsoidal shape and that the ellipse would rotate as a function of the azimuth pointing of the telescopes, like the acceptance maps created from OFF data. Following the procedure used in Da Vela et al. 2018, we collected data from three OFF sources to generate acceptance maps in different azimuth ranges, and from the Crab Nebula to apply them to. The used samples are listed in table A.1 with their coverage in Zd and azimuth. We generated acceptance maps in the low Zd range ($Zd < 35°$) for four azimuth ranges from $100°$ to $240°$

Source	Time period	Zenith [deg]	Azimuth [deg]
3c454.3	September-October 2013	10-35	100-250
RBS0723	December 2013-March 2014	17-35	115-235
B22319+31	August-September 2013	5-26	70-300
Crab Nebula	September-November 2013	7-54	80-270

Table A.1: Data samples from MAGIC observations used in the study of the angular acceptance of the telescopes. The three top rows correspond to data from OFF sources.

using the data from the three OFF sources after applying the analysis cuts (for reference see chapter 5). The same was done to the simulated data from the MC files after being corrected for the energy spectrum difference (process detailed in chapter 5). The comparison between the two approaches can be seen in fig. A.1, where the smaller number of events from the MC files prevents us from seeing a clearly rotating ellipse in the acceptance maps of the bottom row of plots as it is seen in the plots above. We performed a principal component analysis in the unbinned maps from OFF data and from simulations to check that they were consistent with an ellipse. From them, we could obtain the parameters of each ellipse and check the angle between their main axis and the X axis of the plot, what we call their rotation angle. In fig. A.2 we plot the unbinned acceptance maps obtained from OFF data and from MC simulations with their resulting ellipses superposed. The size of the ellipses were chosen to contain all the events of the plots with a 3σ confidence level. The rotation angles of the different acceptance maps analysed are reported in table A.2. After correcting

Az range [deg]	OFF angle [deg]	MC angle [deg]
100 - 135	-89	-87
135 - 170	-60	-53
170 - 205	-25	-10
205 - 240	10	43

Table A.2: Rotation angles of acceptance maps created with OFF data and acceptance maps created with simulated gamma-ray events, both of them generated in bins of 35° azimuth.

for the azimuth rotation of the acceptance maps (both OFF and MC) as seen in chapter 5 and normalizing them so that their most populated bin has a content of 1, we can use them to correct the angular dependence of a standard MAGIC θ^2 plot (see chapter 3). For this test we used data from $\sim$17 h of Crab Nebula

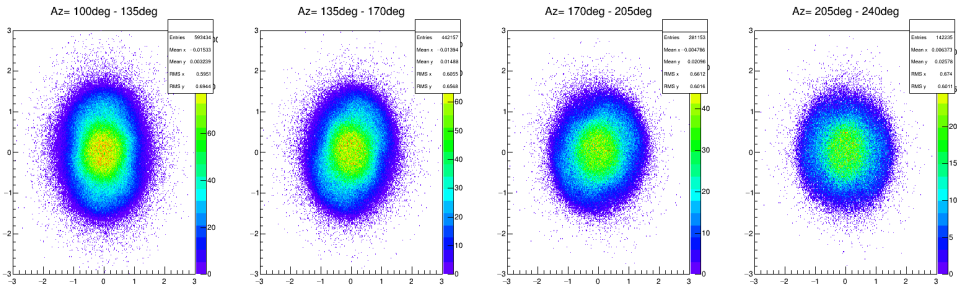

(a) OFF rotation example.

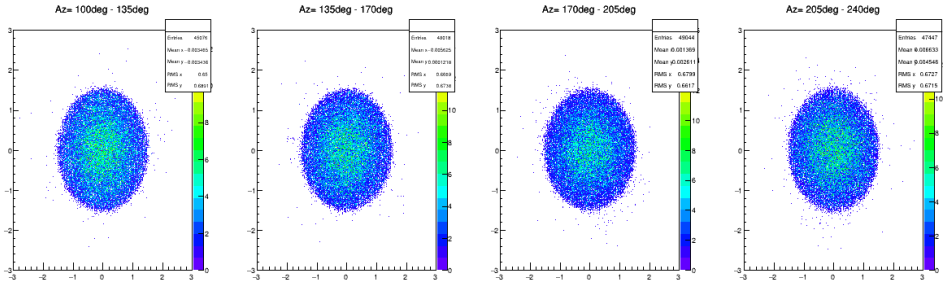

(b) MC rotation example.

Figure A.1: Two-dimensional histograms containing the gamma-ray acceptance maps of the MAGIC telescopes in different 35° azimuth bins, in camera coordinates. Row (a) corresponds to those obtained from the three selected OFF sources and row (b) corresponds to those obtained from simulated gamma-rays. No normalization is included. Bin size is $0.01^\circ \times 0.01^\circ$.

observations (table A.1). We applied the same selection cuts as in the previous results and obtained the distribution of gamma-like events with respect to the centre of the camera. As we can see in fig. A.3, the number of events decreases as we get further away from the center, with a peak at $0.16^{\circ 2}$ due to the presence of the Crab Nebula. This is caused by the lower acceptance of the instrument in the borders of its FoV, as we have seen (chapter 3 and chapter 5), and can be corrected by applying weights to the events that conform the θ^2 plot obtained from the de-rotated acceptance map. Basically, the reconstructed direction of an observed event is transformed to camera coordinates and compared to the chosen acceptance map. The inverse of the content of the bin in the map that corresponds to those coordinates is used as a weight of the observed event when filling the θ^2 histogram. This way, an event in the border of the FoV will have a higher weight than one with a reconstructed direction in the center of the FoV. We have performed this correction on the Crab Nebula results shown in fig. A.3

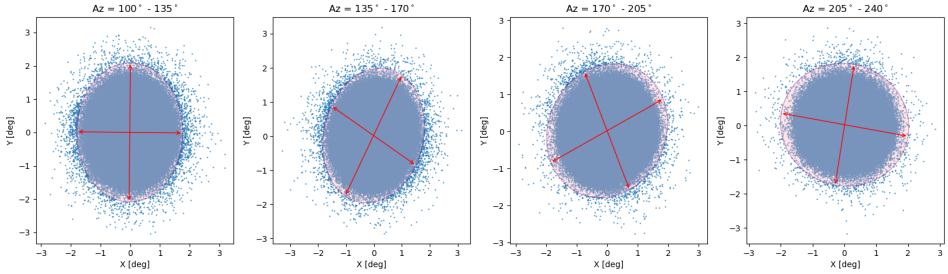

(a) OFF acceptance maps.

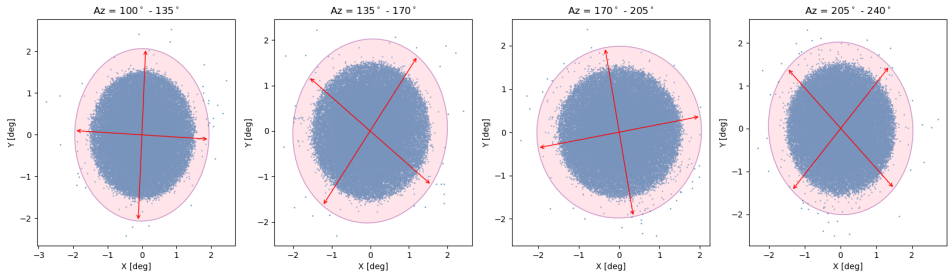

(b) MC acceptance maps.

Figure A.2: Unbinned acceptance maps in 35° bins of azimuth, from 100° to 240°. The pink shadow shows a 3σ confidence level containment ellipse. The red arrows show the big and small ellipse axes obtained by principal component analysis.

with de-rotated acceptance maps from OFF data in fig. A.4 and from simulated data in fig. A.5. The right tail of the corrected distributions was fitted to a zero degree polynomial to confirm its flat shape.

We can also apply the weights from either acceptance map to an OFF observation. This should result in a flat θ^2 distribution, confirming the validity of the use of MC simulated events in the estimation of background for the transient signal search. To see that the method works, we create an acceptance map with only the two bottom OFF sources from table A.1 and apply it to the remaining OFF source data, shown in fig. A.6. We apply a fit to this distribution and calculate the studentized residuals from the fit and the distribution (see fig. A.7). The results are compatible with a constant, a zero degree polynomial. We repeat the process using our acceptance map from simulated events to correct the same OFF source data, confirming again the flatness of the resulting distribution (see fig. A.8).

As complementary material we provide the different acceptance map his-

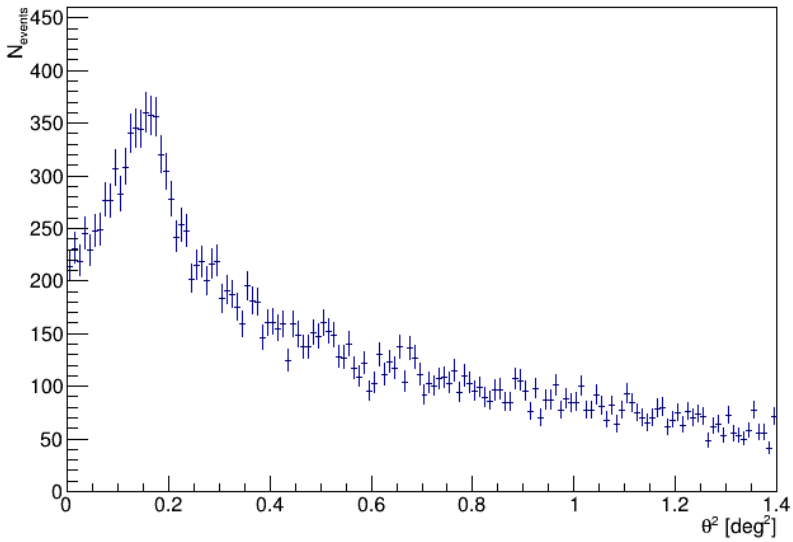

Figure A.3: θ^2 distribution of gamma-ray events with respect to the center of the camera from Crab Nebula observations during October 4th, 2013.

tograms used in these tests in fig. A.9, fig. A.10 and fig. A.11. All of them have been corrected for azimuth rotation following eq. (5.3) and have a cut on events corresponding to pointing directions with $Zd > 50°$. The rest of the cuts applied correspond to those of the transient search analysis (see chapter 5). They have been scaled so that the largest bin in the histogram has a content of 1, providing a relative acceptance to the center of the camera, where the largest bin is located.

A.2 Acceptance map binning

The use of the binning in the previous section was restricted to the one used in Da Vela et al. 2018, but it does not correspond to the binning size employed in the actual acceptance maps that provided the results shown in this work. Here we show the tests performed to choose a binning size that provided a balance between precision and computational time in the search algorithm.

For the estimation of the background events in every time window we need to know the acceptance of the instrument for the reconstructed direction of each event. Actually, we need the acceptance corresponding to the cell that

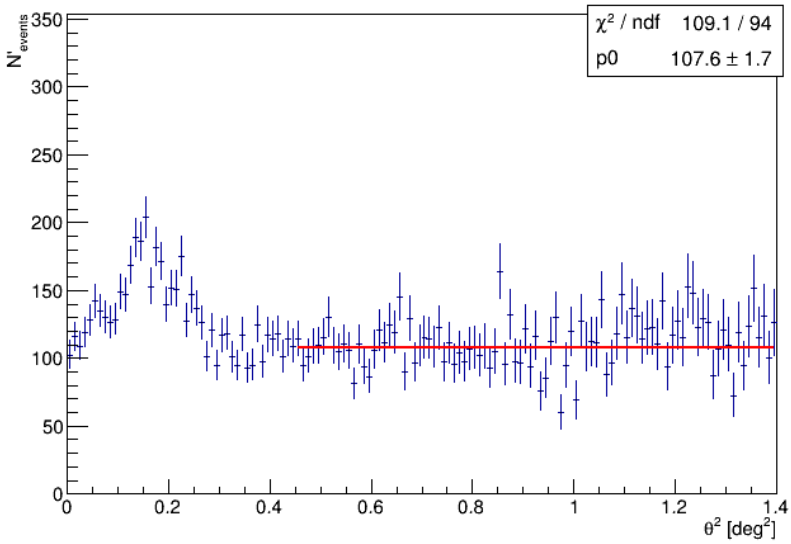

Figure A.4: θ^2 distribution of Crab Nebula corrected for the azimuthal rotation and the instruments acceptance obtained from OFF data. The red line corresponds to the fit to a constant between $0.45 deg^2$ and $1.4 deg^2$.

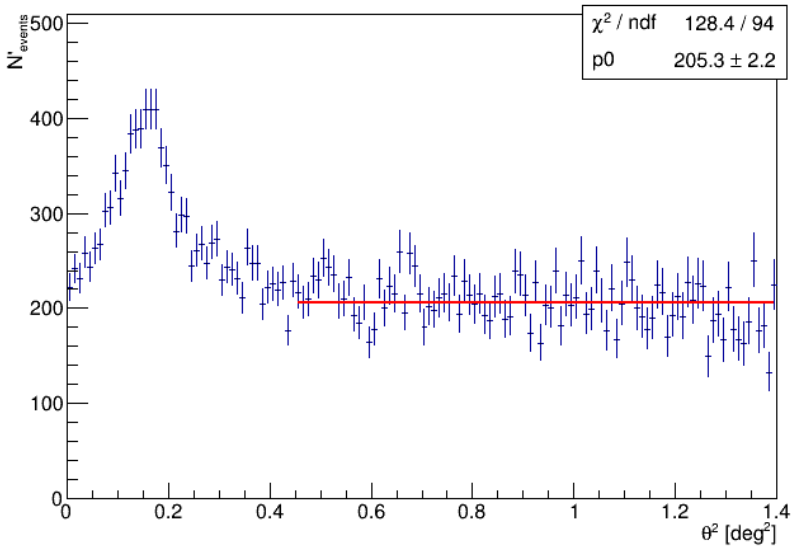

Figure A.5: θ^2 distribution of Crab Nebula corrected for the azimuthal rotation and the instruments acceptance obtained from simulated data. The red line corresponds to the fit to a constant between $0.45 deg^2$ and $1.4 deg^2$.

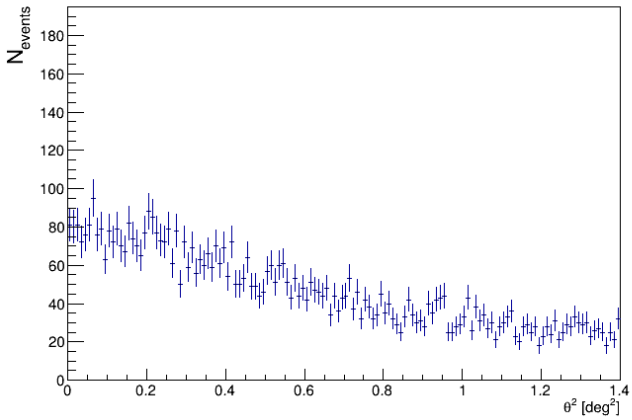

Figure A.6: Original θ^2 distribution of 3c454.3 during October 27th, 2013.

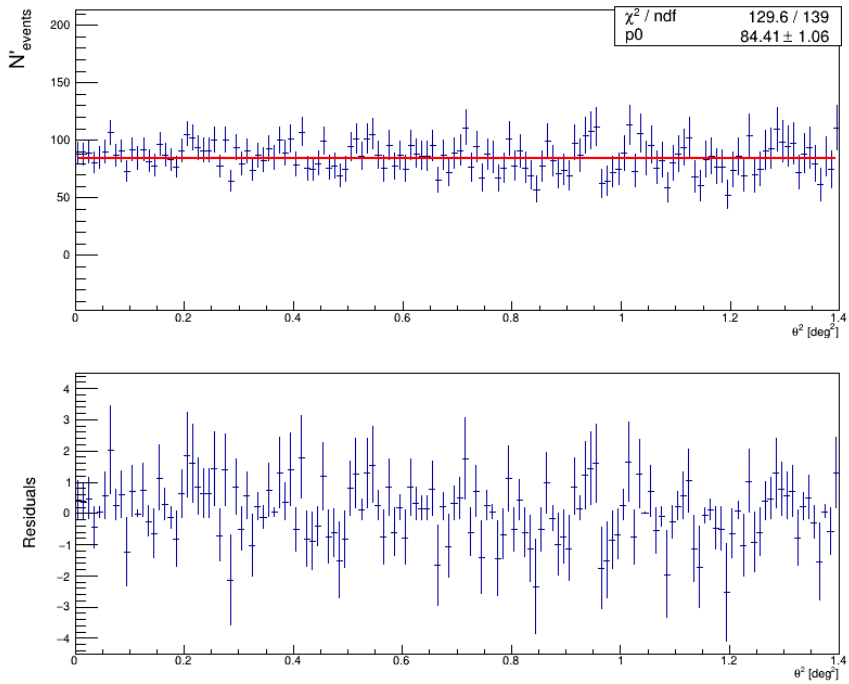

Figure A.7: **Top:** Corrected θ^2 distribution of 3c454.3 during October 27th, 2013. The acceptance map used for the correcting weights was created with OFF data from the sources RBS0723 and B22319+31 as listed in table A.1. The red line corresponds to the fit to a zero degree polynomial. **Bottom:** Plot of the studentized residuals from the corrected θ^2 distribution and the fit curve.

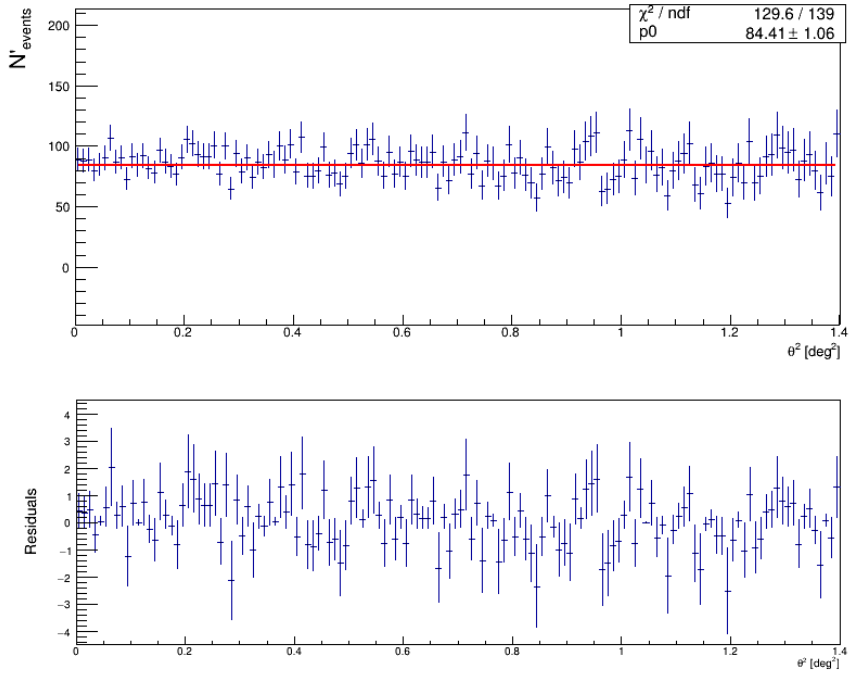

Figure A.8: **Top:** Corrected θ^2 distribution of 3c454.3 during October 27th, 2013. The acceptance map used for the correcting weights was created with simulated gamma-rays from the standard MC production of MAGIC. The red line corresponds to the fit to a zero degree polynomial. **Bottom:** Plot of the studentized residuals from the corrected θ^2 distribution and the fit curve.

the event belongs to. The position of a cell in the FoV of the telescopes can change from second to second, corresponding to a different set of coordinates in the acceptance map. The way to obtain the most precise acceptance estimation for every cell would be to have an unbinned acceptance map and sum the simulated events close to the coordinates of the cell centre up to the search radius r_S. Alternatively, we can have a fixed binned acceptance map with a given bin width, which will be less precise but computationally faster. If we take the results from the first option as the correct acceptance probability of a given position and area in the FoV we can compare them with the results from the binned two-dimensional histogram and use them to choose a bin width.

In the following tests we will refer to the unbinned acceptance map results as the "tree" results and to the binned acceptance map results as the "histogram" or "hist" results. For the first tests we calculated the acceptance of a cell

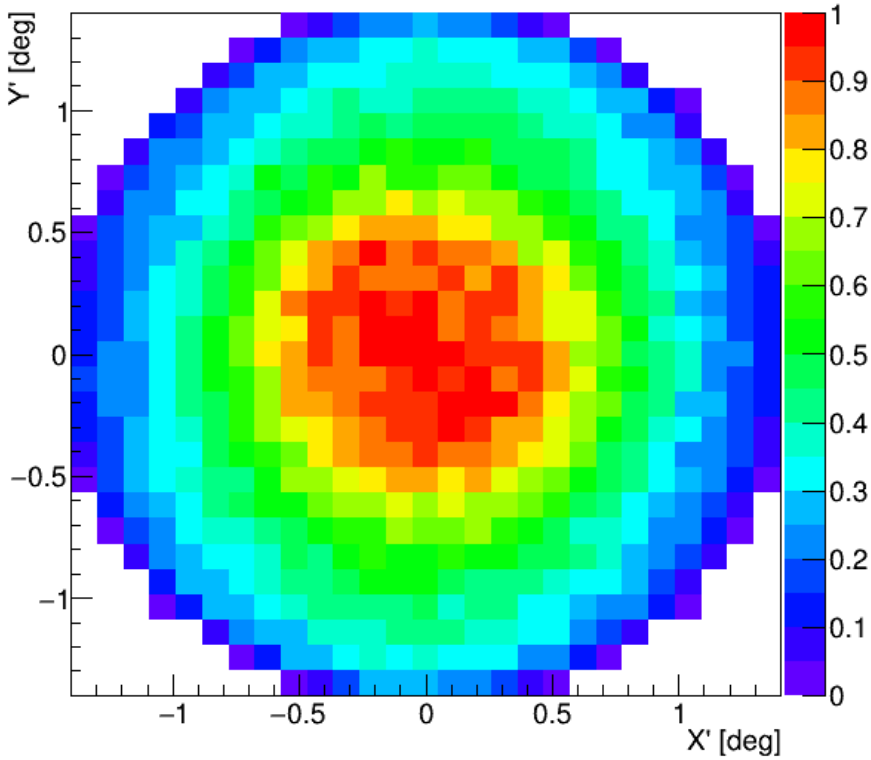

Figure A.9: Acceptance map of the MAGIC telescopes created with MC simulated gamma-ray events, in camera coordinates after the azimuth rotation correction. The binning used is $0.1° \times 0.1°$.

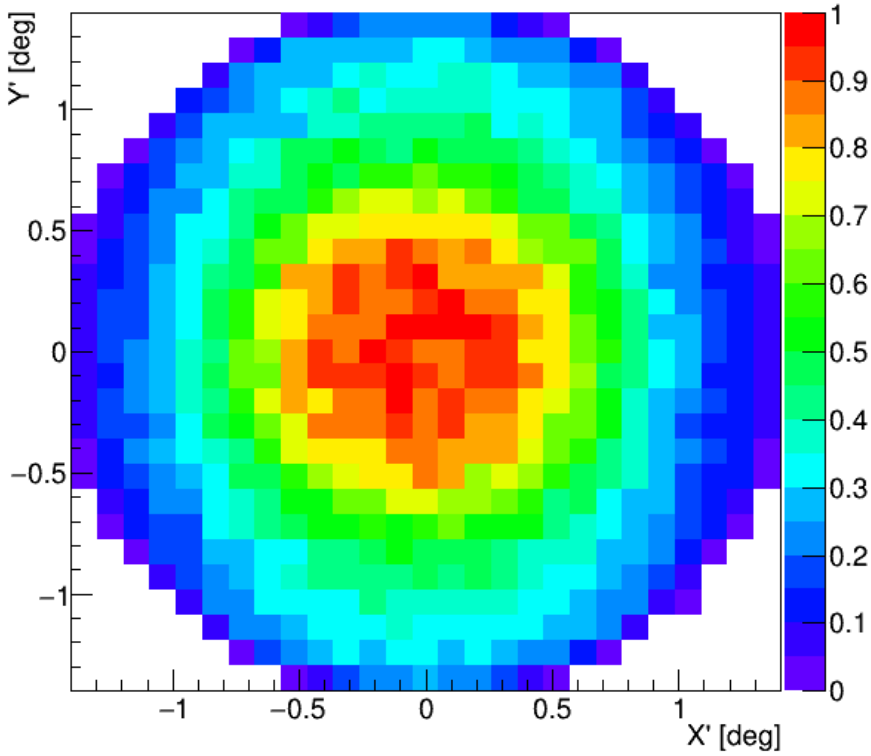

Figure A.10: Acceptance map of the MAGIC telescopes created with OFF data from the observations of 3c454.3, in camera coordinates after the azimuth rotation correction. The binning used is $0.1^\circ \times 0.1^\circ$. This is the one used in the correction of the Crab Nebula θ^2 plot.

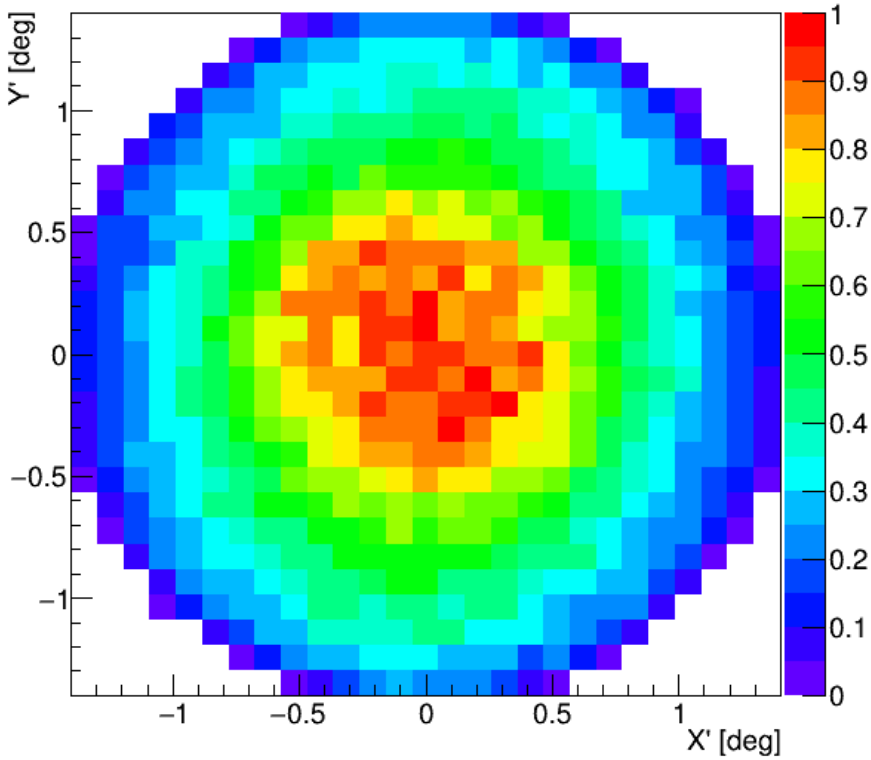

Figure A.11: Acceptance map of the MAGIC telescopes created with OFF data from the observations of RBS0723 and B22319+31, in camera coordinates after the azimuth rotation correction. The binning used is $0.1° \times 0.1°$. This is the one used in the correction of the 3c454.3 θ^2 plot.

with centre in coordinates $(0, 0)$ of the acceptance map. The radius of the cells is constant among the tests and equal to the one used in the search algorithm, $r_S = 0.15°$. From there we obtained the time it took the code to run with the "tree" option and with the "hist" option. We show the ratio of the run time for different bin widths of the 2D histogram in fig. A.12, where we can see that the run time for the binned acceptance map increases rapidly with smaller bin widths. This is inversely proportional to the difference between the acceptance

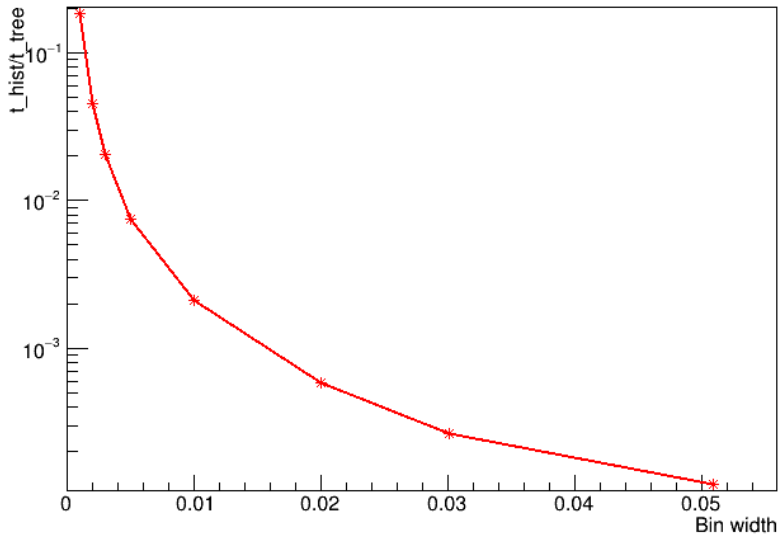

Figure A.12: Ratio of the run time needed to obtain the acceptance for one cell with the unbinned method and with the binned method, for different bin widths.

value provided by the unbinned method and the acceptance value provided by the binned method, which increases with the bin width, as shown in fig. A.13.

The position of the cell within the acceptance map has an effect on the result difference between methods, having a stronger impact on larger bin widths. For this reason we obtained the run time ratio and the acceptance result difference for many different coordinates in the FoV/acceptance map, to see if any bin width would appear as consistently low in both parameters. Here are the first tests for bin widths between $0.0002°$ and $0.05°$, fig. A.14.

Seeing the large variability in the precision obtained with the binned acceptance map ("hist" method), we decided to repeat the tests with smaller bin widths, this time between $0.002°$ and $0.035°$ in $0.0005°$ steps, which are shown

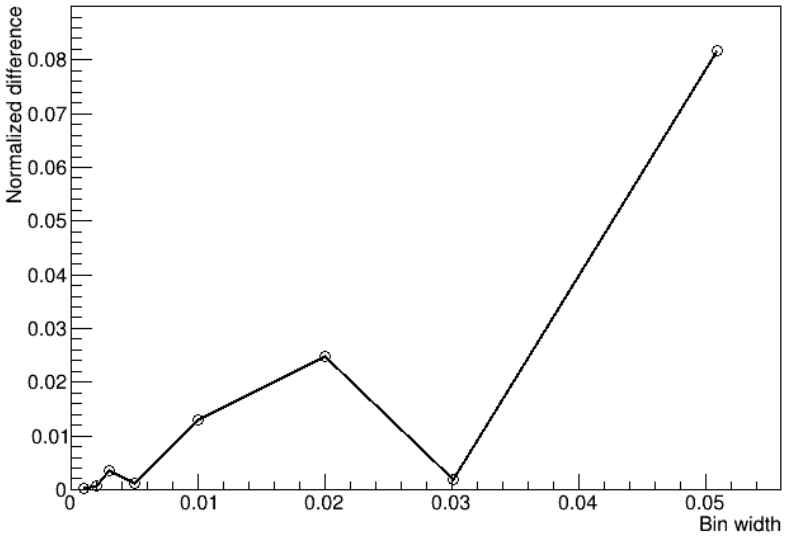

Figure A.13: Difference between the "tree" method acceptance value and the "hist" method acceptance value, divided by the "tree" value, as a function of the bin width selected for the "hist" method.

in fig. A.15. In the end, the bin width used in the search algorithm for the binned acceptance map was chosen to be $0.005°$, since it showed a consistently high precision among the different tests (the normalized different between the results from both methods always remained below 0.006).

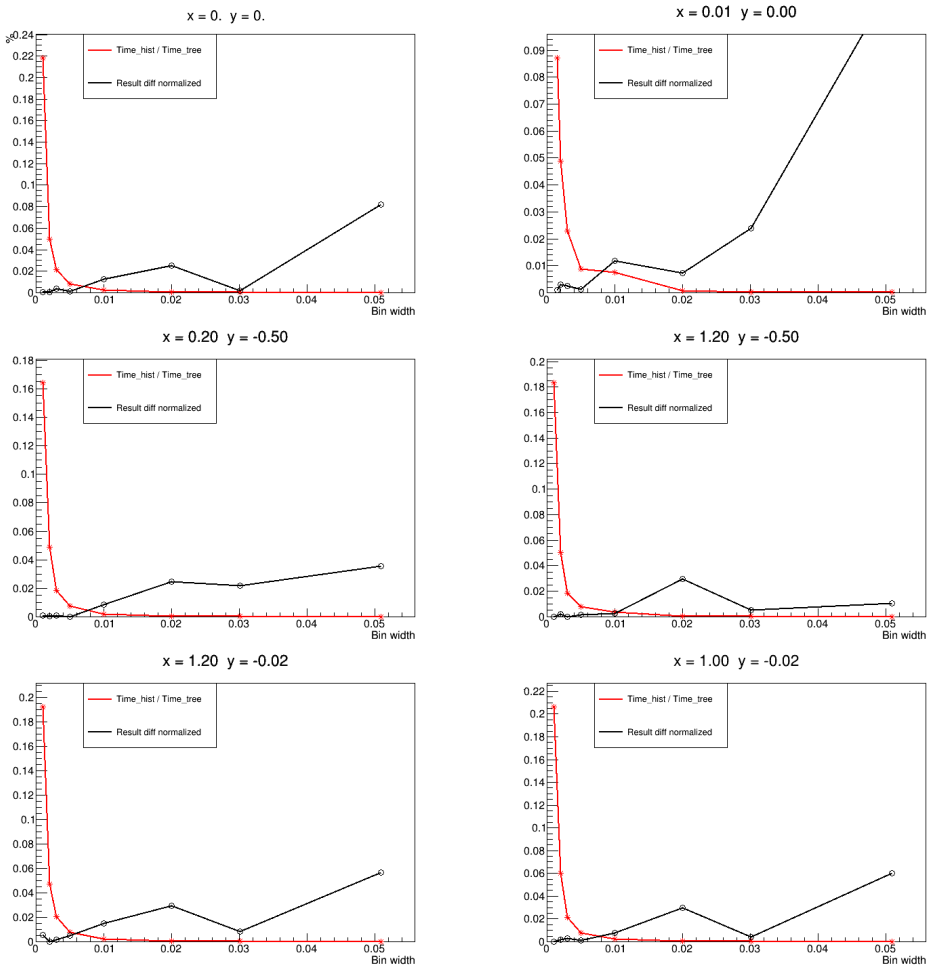

Figure A.14: Difference in computational run time and acceptance value precision in various regions of the FoV of the instrument. The red line shows the ratio between the run time of the "hist" method and the "tree" method in the calculation of the acceptance corresponding to a cell. The black line shows the difference between the acceptance result of the "tree" method and the "hist" method, divided by the result of the "tree" method. The X axis shows the bin width chosen for the "hist" method, in degrees, and the Y axis shows the dimensionless ratios.

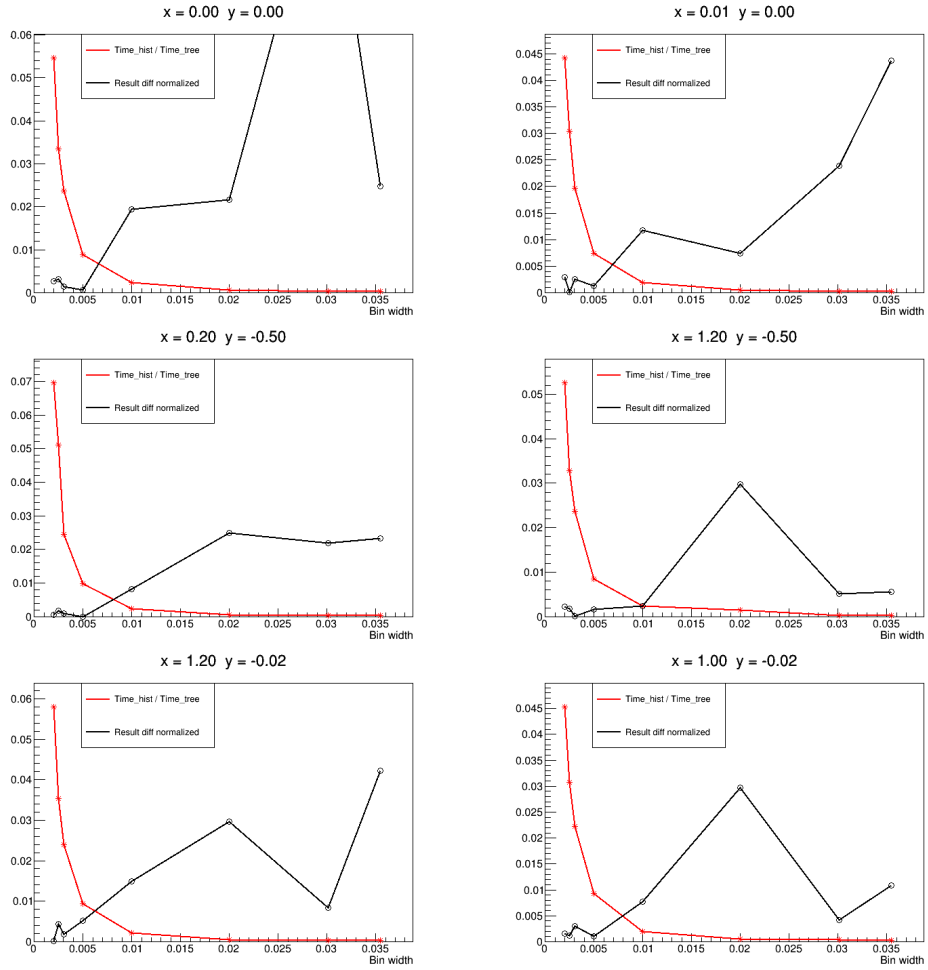

Figure A.15: Difference in computational run time and acceptance value precision in various regions of the FoV of the instrument. The red line shows the ratio between the run time of the "hist" method and the "tree" method in the calculation of the acceptance corresponding to a cell. The black line shows the difference between the acceptance result of the "tree" method and the "hist" method, divided by the result of the "tree" method. The X axis shows the bin width chosen for the "hist" method, in degrees, and the Y axis shows the dimensionless ratios.

Appendix B

Systematic uncertainties tests

Compilation of tests performed to find the actual distribution of the number of expected background events variable given by our model. First we checked that the significance distribution from observed and simulated events from the four first observation samples listed in table 6.1 followed a Gaussian function.

Assuming that the real number of expected events in a cell i and time window j follows a Gaussian distribution around the number predicted by our background model, $B_{i,j}$, we modified the method to generate simulated events to reproduce the observed significance distribution.

In order to do that, in the simulation process described in section 6.2.1 we add another level of iteration. For each $B_{i,j}$ we generate 100 numbers following a Gaussian distribution with mean $B_{i,j}$ and standard deviation $kB_{i,j}$, where $0 < k < 1$ is the factor we modify to minimize the difference between the distribution of significance from observed events and the distribution of significance from simulated events. The 100 generated numbers are used as the mean value of a Poisson distribution to generate another number each, the final simulated number of background events. The p-value of the resulting number of events is calculated following eq. (6.2) with $\mu = B_{i,j}$.

This way, for an observation with $N_{\text{windows}} \cdot N_{\text{cells}}$ trials, we have $100 \cdot N_{\text{windows}} \cdot N_{\text{cells}}$ simulated numbers of events. In the following pages, a selection of the plots obtained to calculate the value of k is shown. In them, the characterization of the significance distributions from observed and simulated events is done through the fitting of a Gaussian function to the two histograms and

the direct calculation of the mean and RMS of the histograms. The most relevant parameters are the standard deviation, σ_{obs}, from the Gaussian fit to the observed events significance distribution and the equivalent σ_{sims} from the fit to the simulated events significance distribution.

During the testing process we found that the selection of *seed* number for the random number generator affected the measured difference between significance distributions, so every k test was repeated for 19 different *seed* numbers. The difference between the fit results for the standard deviation of the observed distribution and the simulated distribution was gathered for each test and is shown in fig. B.13, fig. B.14, fig. B.15 and fig. B.16. The mean k (among the tests with different *seed* number) value that minimizes the difference between distributions was selected for each FoV and time period. In fig. B.17, the selected k values are shown with error bars that stretch to the minimum and maximum k values obtained in the 19 simulations realized for each of the selected k. The weighted average of the four FoVs/period k, 0.076, was applied to a new sample of observations to validate[1] its applicability to other FoVs. In order to do that, the difference between distributions is calculated by a chi^2 test.

The simulated events are again generated with varying *seed* numbers, so we have multiple χ^2/ndf results for each FoV. These results are listed in table B.1.

The characterization of the significance distributions of the validation sample is shown, for a single *seed* value test of each FoV, in fig. B.18, fig. B.19 and fig. B.20.

[1] The average of the k and the average of their minimum and maximum values in fig. B.17 were also used in the validation process, obtaining worse χ^2/ndf values in general than $k = 0.076$.

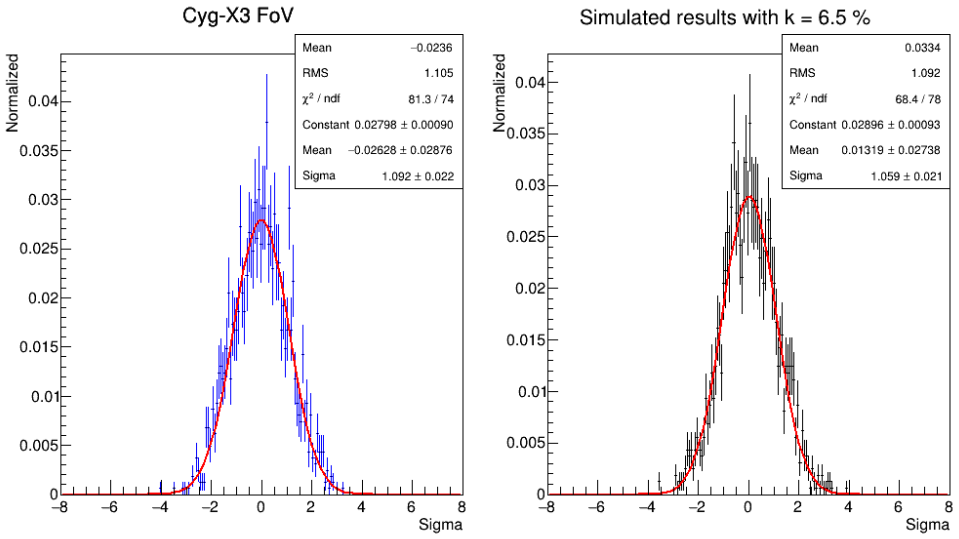

Figure B.1: Gaussian simulations test with observations from the Fov around Cyg-X3 during May 2014. The left panel contains the significance distribution of observed events, while the right panel contains the significance distribution of simulated events. Those events were generated with a Gaussian function with $\mu = B_{i,j}$ and $\sigma = kB_{i,j} = 0.065B_{i,j}$.

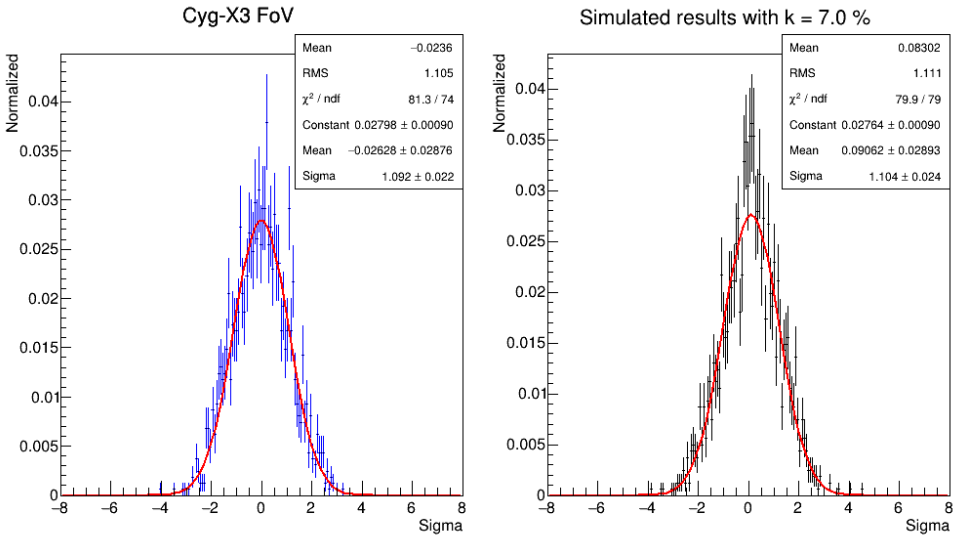

Figure B.2: Refer to the caption in fig. B.1. $k = 0.07$.

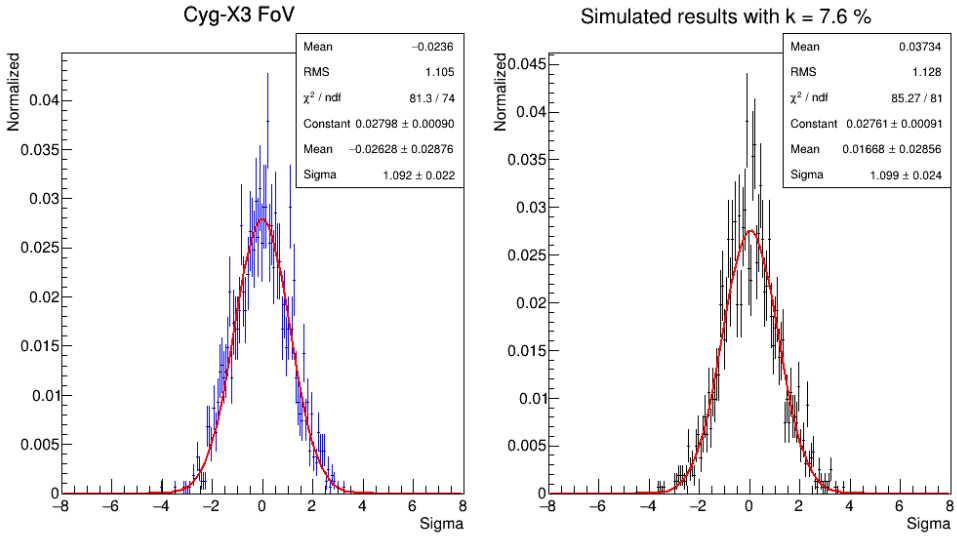

Figure B.3: Refer to the caption in fig. B.1. $k = 0.076$.

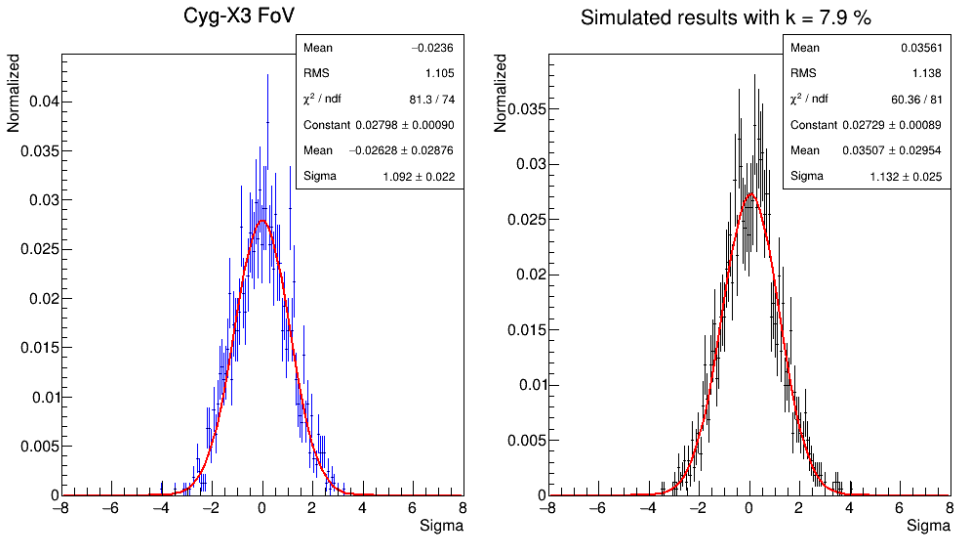

Figure B.4: Refer to the caption in fig. B.1. $k = 0.079$.

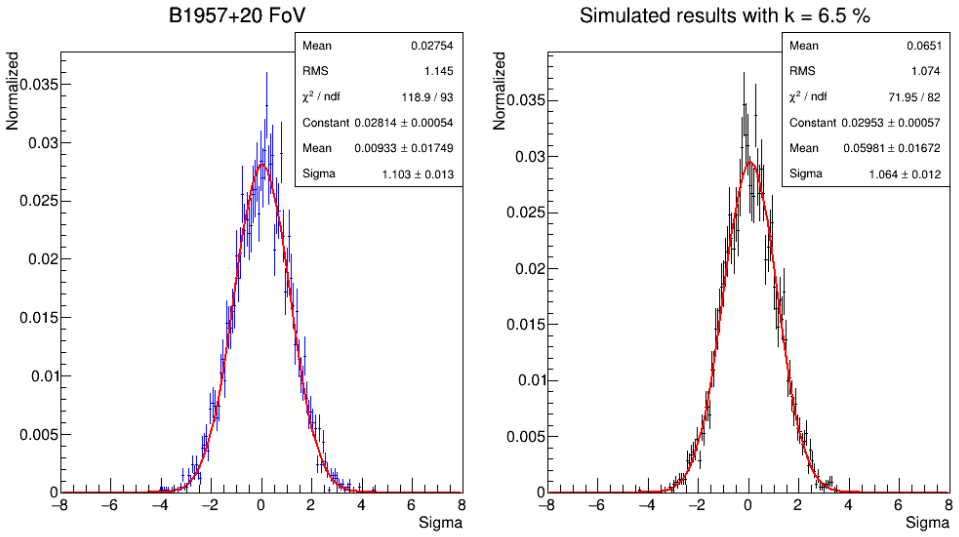

Figure B.5: Gaussian simulations test with observations from the Fov around B1957+20 during September 2013. The left panel contains the significance distribution of observed events, while the right panel contains the significance distribution of simulated events. Those events were generated with a Gaussian function with $\mu = B_{i,j}$ and $\sigma = kB_{i,j} = 0.065B_{i,j}$.

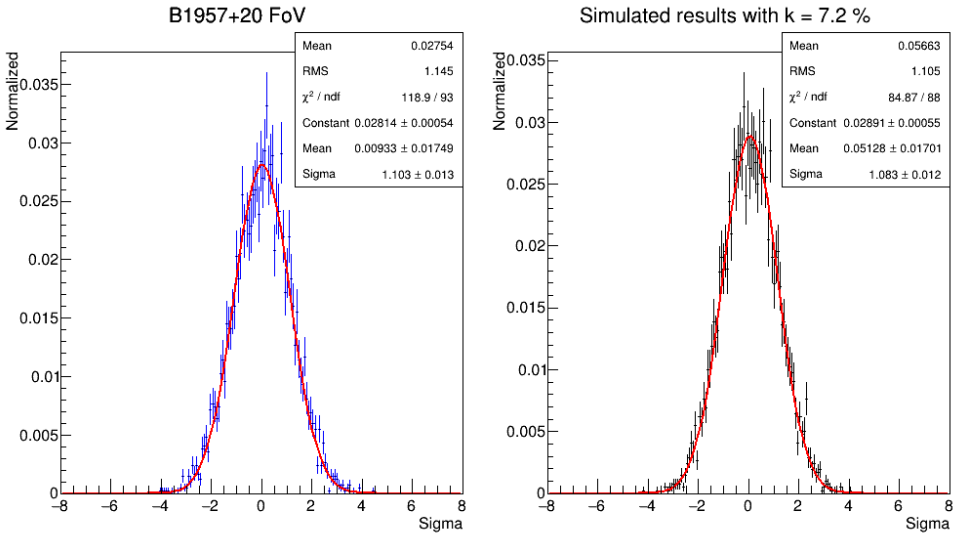

Figure B.6: Refer to the caption in fig. B.5. $k = 0.072$.

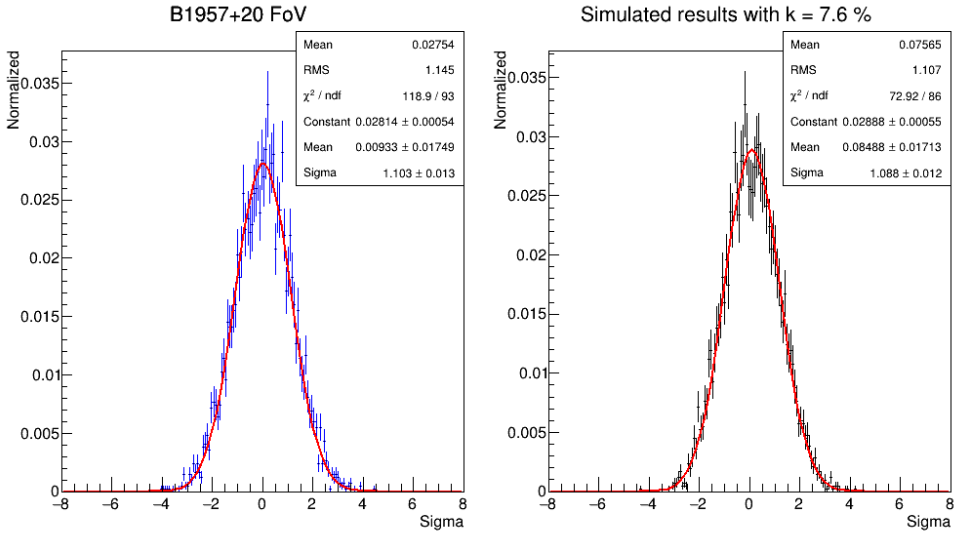

Figure B.7: Refer to the caption in fig. B.5. $k = 0.076$.

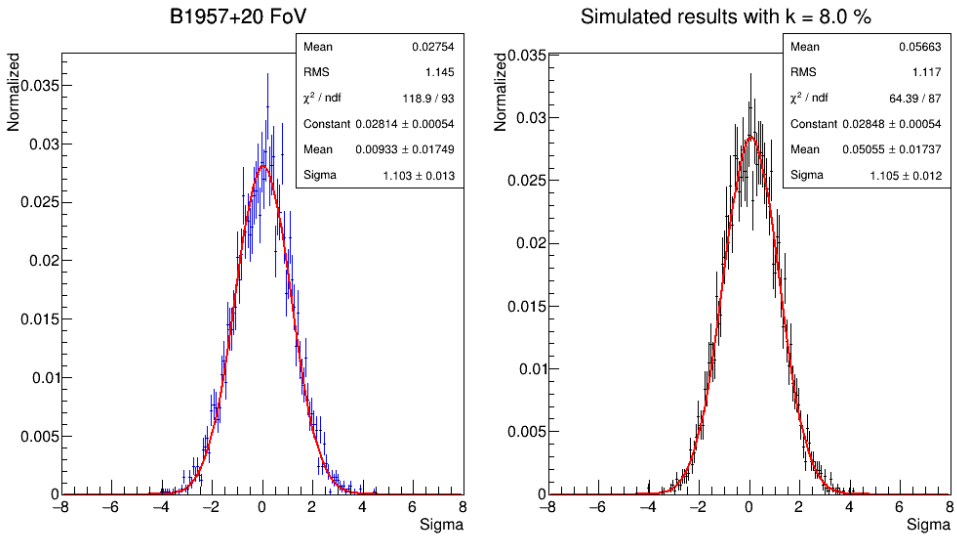

Figure B.8: Refer to the caption in fig. B.5. $k = 0.08$.

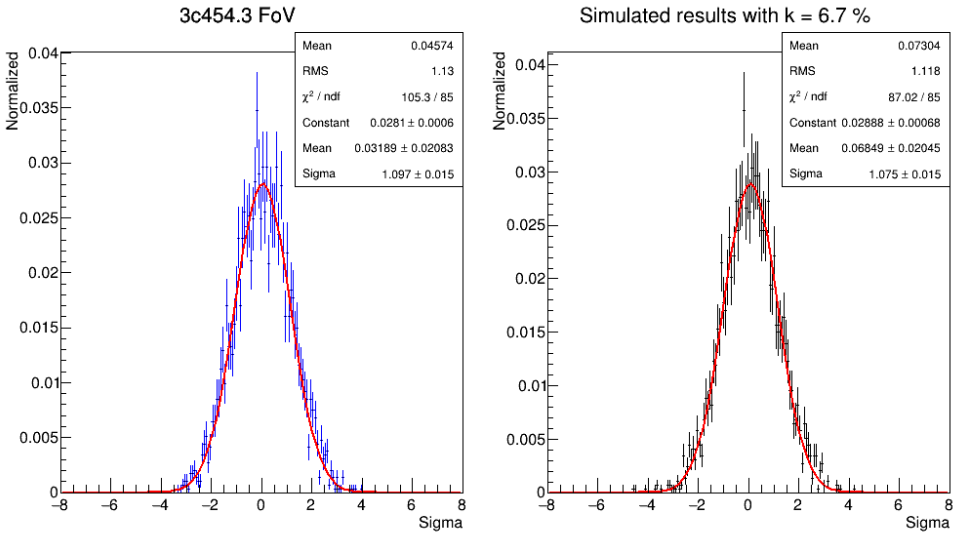

Figure B.9: Gaussian simulations test with observations from the Fov around 3c454.3 during September 2013. The left panel contains the significance distribution of observed events, while the right panel contains the significance distribution of simulated events. Those events were generated with a Gaussian function with $\mu = B_{i,j}$ and $\sigma = kB_{i,j} = 0.067B_{i,j}$.

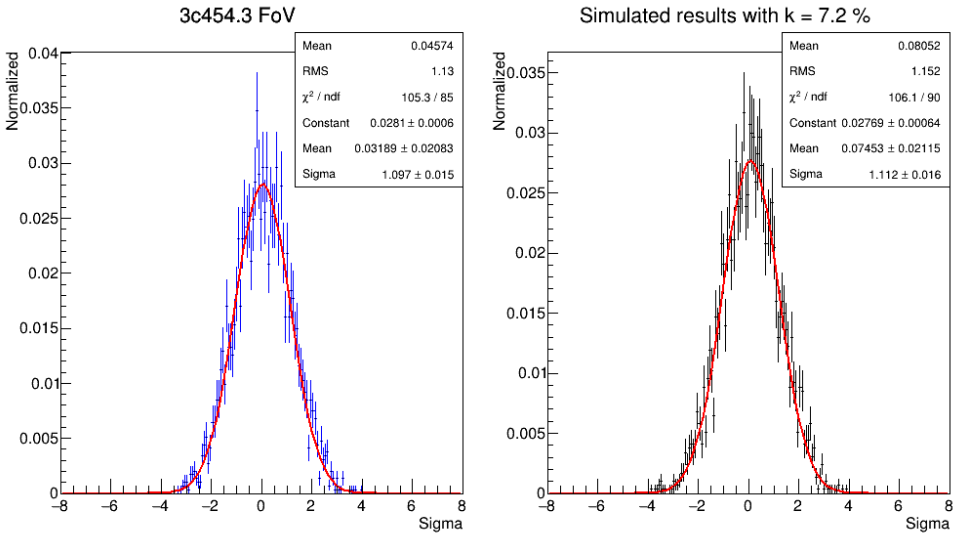

Figure B.10: Refer to the caption in fig. B.9. $k = 0.072$.

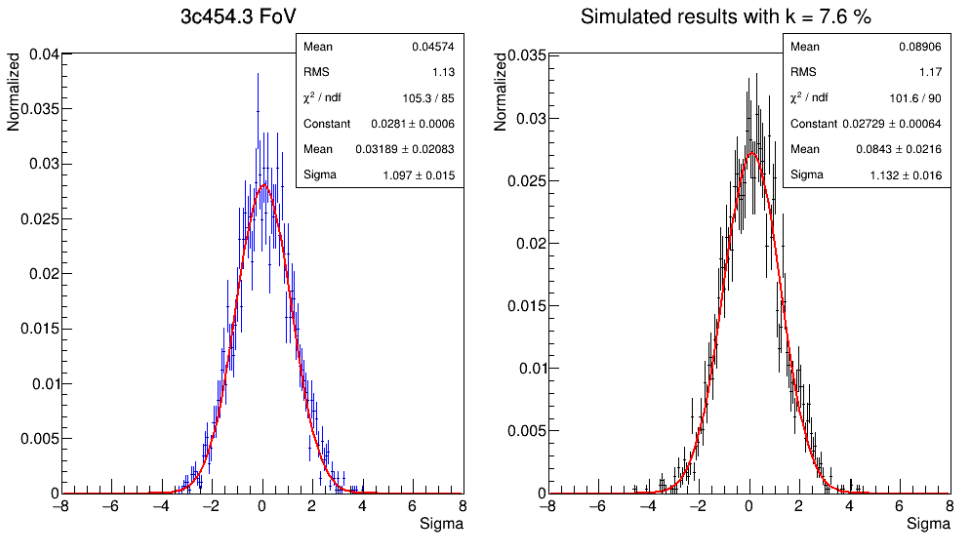

Figure B.11: Refer to the caption in fig. B.9. $k = 0.076$.

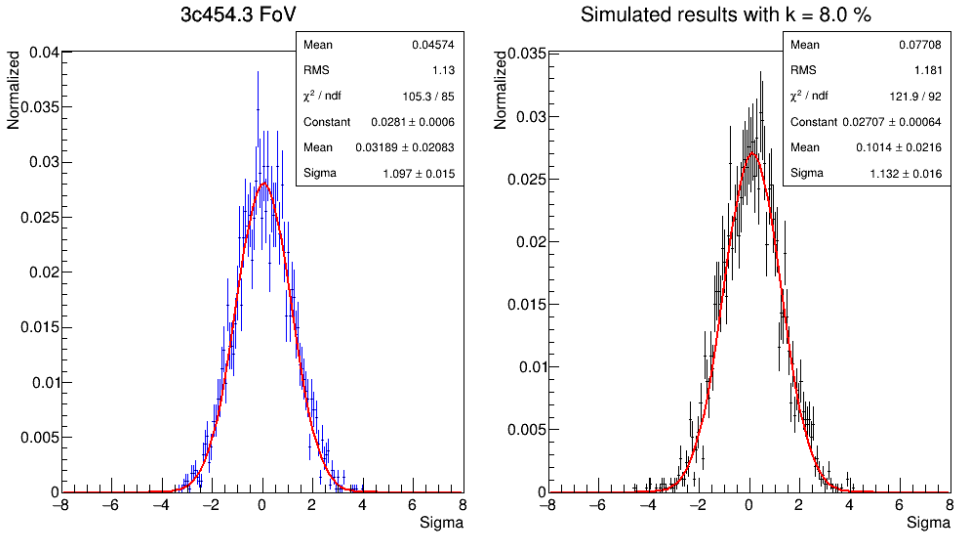

Figure B.12: Refer to the caption in fig. B.9. $k = 0.08$.

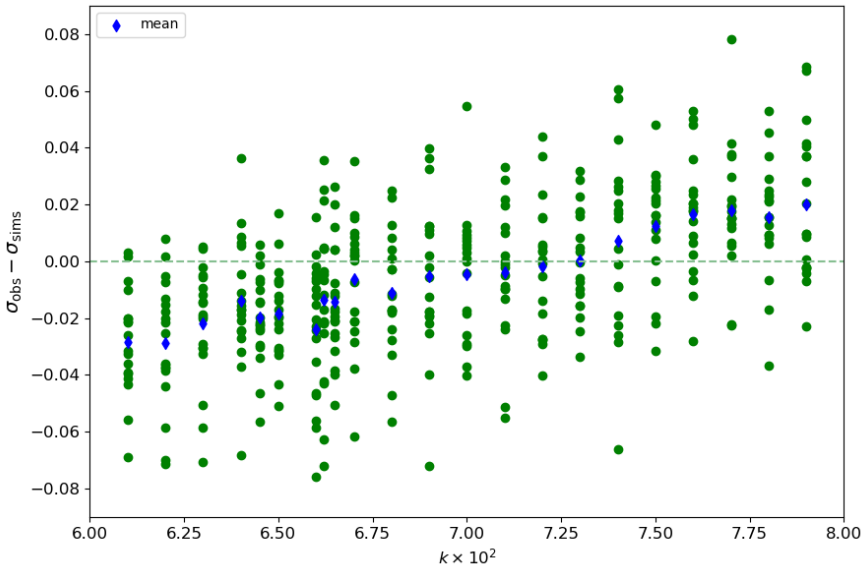

Figure B.13: Difference in distribution widths (observed events significance and simulated events significance) with respect to the factor k used to generate simulated events. Each column of green dots corresponds to a simulation with a different random generator seed, to see the variation of σ_{sims}. The blue diamonds correspond to the mean $\sigma_{\mathrm{obs}} - \sigma_{\mathrm{sims}}$ of each set of simulations with the same k. The data used corresponds to the observations of the FoV around Cyg-X3 during May 2014.

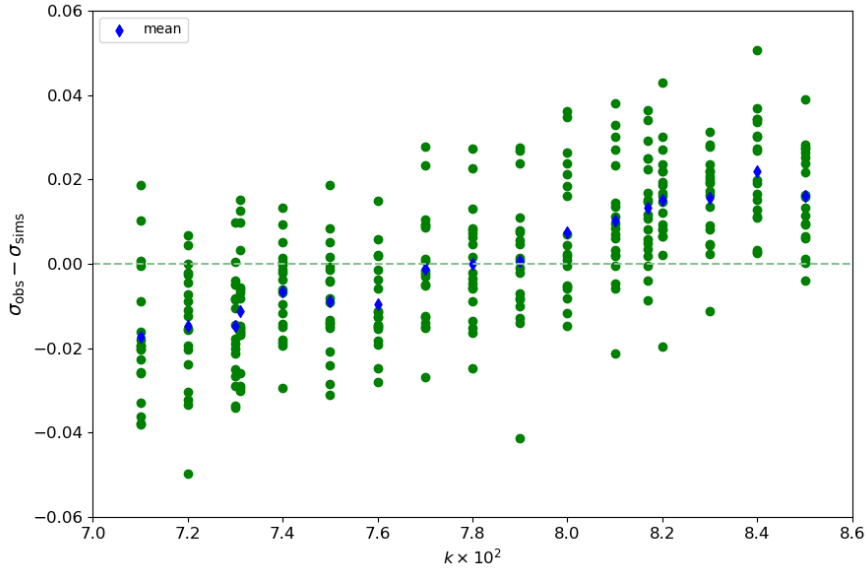

Figure B.14: Refer to the caption in fig. B.13. The data used corresponds to the observations of the FoV around B1957+20 during September 2013.

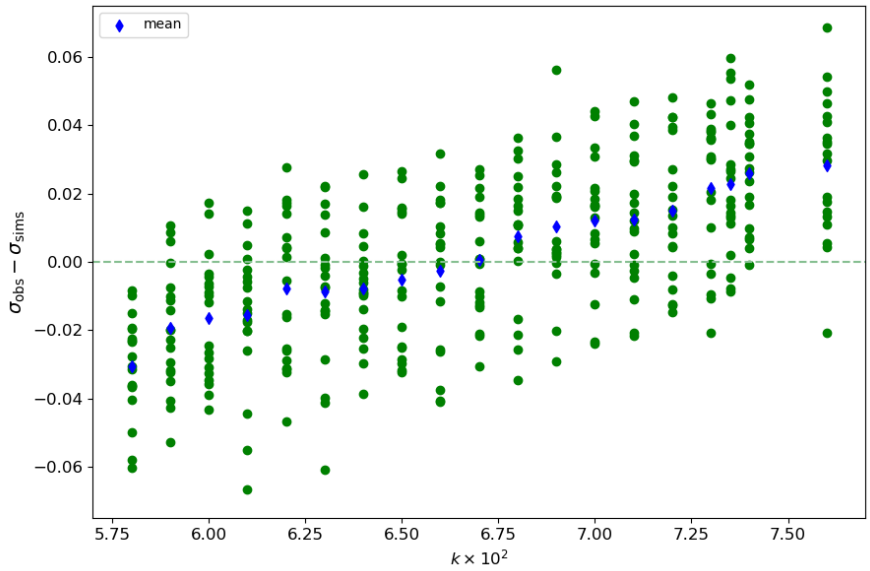

Figure B.15: Refer to the caption in fig. B.13. The data used corresponds to the observations of the FoV around 3c454.3 during September 2013.

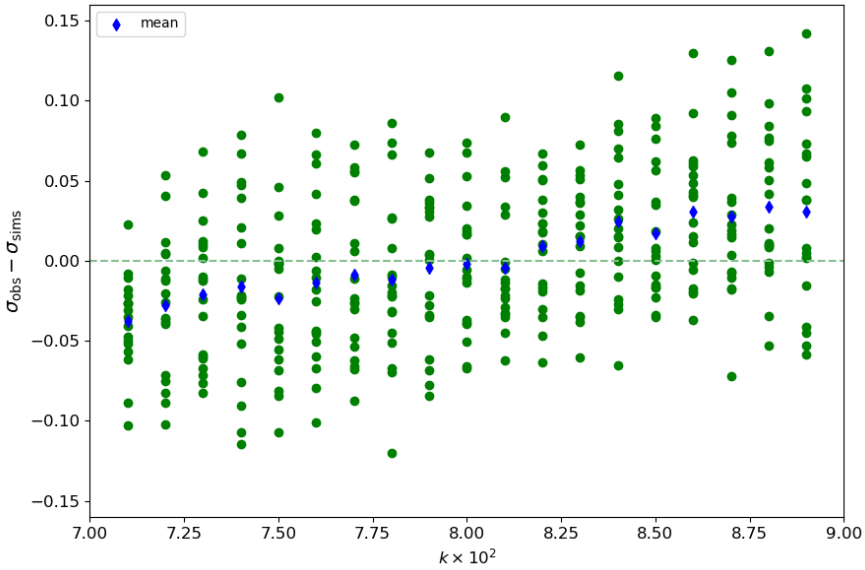

Figure B.16: Refer to the caption in fig. B.13. The data used corresponds to the observations of the FoV around 3c454.3 during June 2014.

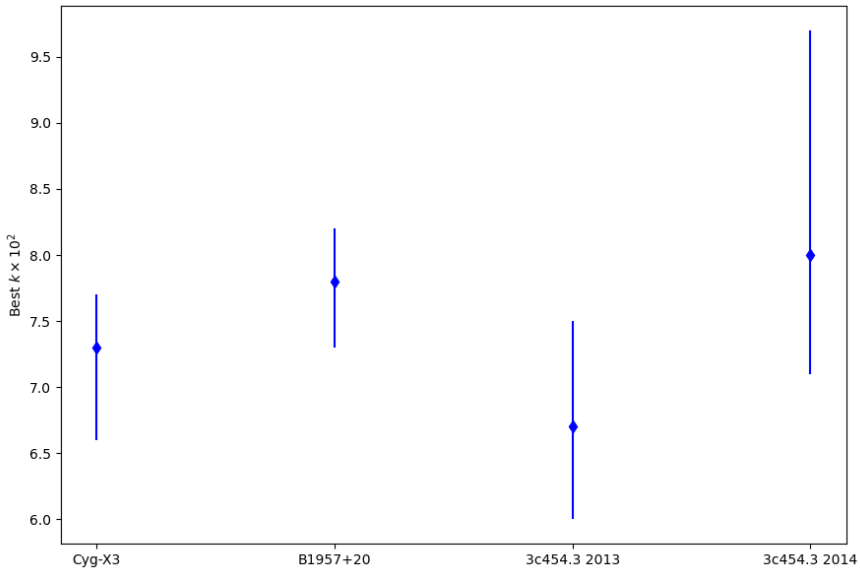

Figure B.17: Plot of the best k values for each observation sample, where error bars are calculated as the minimum and maximum $\sigma_{\rm obs} - \sigma_{\rm sims}$ obtained for that k.

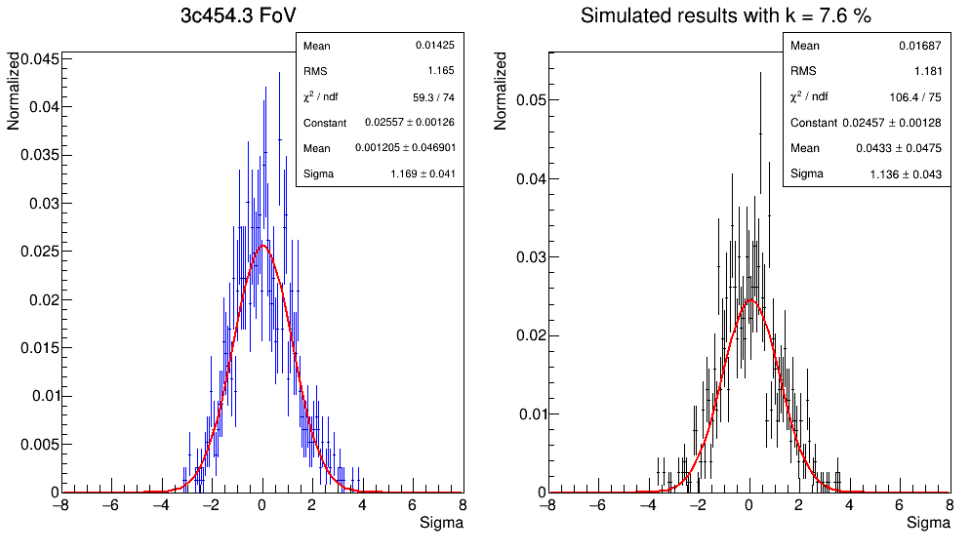

Figure B.18: Gaussian simulations test with observations from the Fov around 3c454.3 during October 2013. For more detail refer to the caption in fig. B.1.

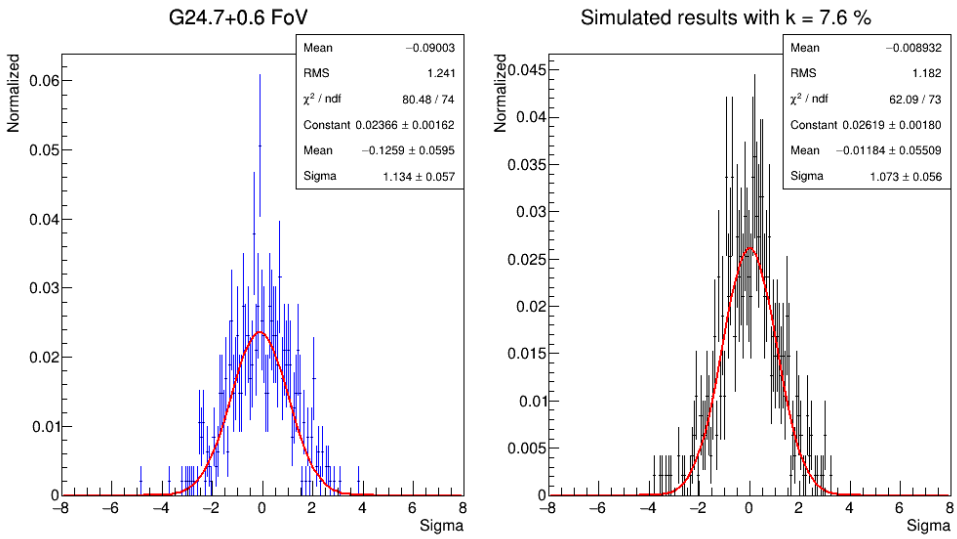

Figure B.19: Gaussian simulations test with observations from the Fov around G24.7+0.6 during April 2014. For more detail refer to the caption in fig. B.1.

Seed	χ^2/ndf		
	3c454 Oct13	G24.7+0.6	TXS2320+343
1	1.137	0.851	1.245
2	1.286	0.872	1.051
3	1.326	1.088	0.836
4	1.015	0.849	0.949
5	0.953	0.786	0.874
6	1.428	1.173	0.780
7	1.042	0.849	0.804
8	1.014	1.936	1.015
9	0.850	0.726	1.129
10	1.046	1.134	0.828
11	0.735	0.836	0.686
12	0.902	1.034	0.775
13	0.955	1.228	0.819
14	1.211	0.797	1.271
15	0.973	1.322	0.988
16	1.456	1.029	0.985
17	1.071	0.871	1.590
18	0.798	0.829	1.260
19	0.956	0.798	1.163
mean	1.020	0.966	0.965
std	0.268	0.312	0.275

Table B.1: Goodness of fit in each simulation test done for $k = 0.076$ in the validation sample observations.

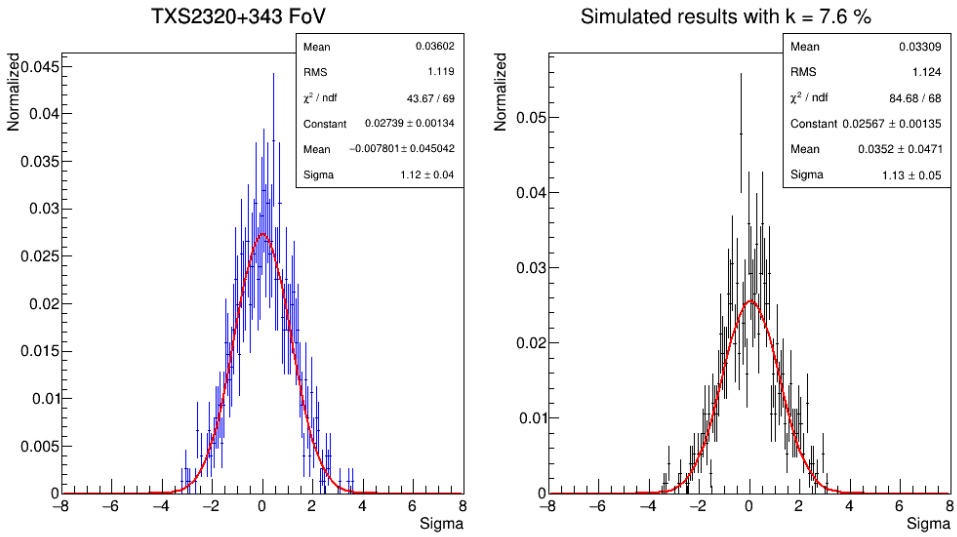

Figure B.20: Gaussian simulations test with observations from the Fov around TXS2320+343 during November 2013. For more detail refer to the caption in fig. B.1.

Appendix C

Flare candidates

This appendix is an extension of section 7.2, where we gather all the flare candidates found in the analysis of the data from MAGIC observations performed between 2013/07/27 and 2014/06/18 and between 2014/07/05 and 2014/08/05, with the selection cuts detailed in the main text.

Each of the following tables corresponds to the application of the transient search algorithm with one of the four used time windows, Δt. They contain the information of the spatial cells and time windows where the excess of observed events compared to the expected background is $\geq 3\sigma$ after correcting for the number of trials in that cell and for the systematic uncertainty of the background model.

Table C.1: Results from the $\Delta t = 1000$s search. The table contains the cell index and its equatorial coordinates, as well as the timing of the flare (centre value of the time window) in Modified Julian Date (MJD) and the number of observed and expected events in that time window. The cell index is provided to facilitate match searches.

Cell	Mjd	Obs	Exp	RA	Dec
438315	56669.257325	45	21.508	$12^{\mathrm{h}}59^{\mathrm{m}}45.938^{\mathrm{s}}$	$-6°34'46.535''$
459916	56825.928085	31	14.611	$15^{\mathrm{h}}15^{\mathrm{m}}28.125^{\mathrm{s}}$	$-9°44'43.535''$
460938	56825.912375	44	23.329	$15^{\mathrm{h}}13^{\mathrm{m}}21.563^{\mathrm{s}}$	$-9°53'48.672''$

Table C.2: Results from the $\Delta t = 100$s search. For more details, please refer to table C.1.

Cell	Mjd	Obs	Exp	RA	Dec
21600	56686.105915	4	0.525	$10^{h}07^{m}30.000^{s}$	$70°54'24.000''$
23286	56690.106912	9	1.667	$9^{h}38^{m}20.000^{s}$	$70°09'54.096''$
25530	56724.176816	1	0.012	$11^{h}32^{m}55.221^{s}$	$69°14'12.448''$
25530	56724.176237	1	0.012	$11^{h}32^{m}55.221^{s}$	$69°14'12.448''$
28795	56741.030700	15	3.208	$11^{h}43^{m}30.000^{s}$	$67°56'05.743''$
33583	56545.175904	10	1.143	$1^{h}57^{m}41.538^{s}$	$66°04'12.232''$
41886	56549.227947	9	2.070	$5^{h}11^{m}35.172^{s}$	$63°15'37.757''$
50956	56656.947091	8	0.901	$2^{h}49^{m}52.500^{s}$	$60°26'03.980''$
59474	56874.146541	16	3.843	$22^{h}39^{m}25.116^{s}$	$58°09'37.327''$
100285	56698.235843	11	2.123	$10^{h}11^{m}31.071^{s}$	$48°08'28.348''$
154587	56776.995060	14	3.030	$11^{h}06^{m}33.750^{s}$	$37°21'22.960''$
165221	56872.036597	12	2.135	$20^{h}20^{m}37.500^{s}$	$35°30'06.641''$
197648	56697.245082	20	5.430	$12^{h}21^{m}05.625^{s}$	$29°49'40.292''$
231438	56693.168433	13	3.031	$12^{h}18^{m}59.063^{s}$	$24°17'47.321''$
240744	56772.059365	20	5.418	$14^{h}24^{m}50.625^{s}$	$22°49'53.061''$
250895	56664.156434	8	0.948	$12^{h}19^{m}41.250^{s}$	$21°13'18.456''$
259411	56515.101062	8	0.855	$19^{h}55^{m}18.750^{s}$	$19°56'48.119''$
262483	56512.051168	4	0.320	$19^{h}56^{m}00.938^{s}$	$19°28'16.394''$
316439	56714.190742	16	3.591	$12^{h}30^{m}56.250^{s}$	$11°15'46.726''$
319654	56728.215432	27	9.696	$15^{h}52^{m}44.063^{s}$	$10°48'24.922''$
321706	56728.203520	22	7.240	$15^{h}58^{m}21.562^{s}$	$10°30'11.777''$
356059	56548.163658	10	2.188	$5^{h}07^{m}15.938^{s}$	$5°22'45.764''$
368935	56774.158125	11	0.842	$18^{h}54^{m}08.438^{s}$	$3°34'59.958''$
390441	56868.985906	18	4.494	$18^{h}56^{m}15.000^{s}$	$0°26'51.460''$
425427	56595.947511	3	0.147	$22^{h}55^{m}18.750^{s}$	$-4°37'49.726''$
434642	56595.948090	2	0.061	$22^{h}54^{m}36.563^{s}$	$-5°58'44.964''$
439338	56719.060830	14	2.548	$12^{h}57^{m}39.375^{s}$	$-6°43'47.326''$

Table C.3: Results from the $\Delta t = 10$s search. For more details, please refer to table C.1.

Cell	Mjd	Obs	Exp	RA	Dec
18744	56691.999470	5	0.200	$7^{h}23^{m}30.309^{s}$	$72°12'09.419''$
22394	56693.010176	5	0.257	$7^{h}33^{m}23.774^{s}$	$70°32'09.418''$
25047	56686.091876	5	0.229	$9^{h}46^{m}36.429^{s}$	$69°25'21.167''$
25530	56724.176410	1	0.012	$11^{h}32^{m}55.221^{s}$	$69°14'12.448''$
34108	56630.889676	4	0.084	$2^{h}10^{m}32.061^{s}$	$65°52'59.637''$
35154	56551.207229	5	0.121	$1^{h}52^{m}19.850^{s}$	$65°30'33.740''$
35687	56551.205204	6	0.210	$1^{h}54^{m}10.746^{s}$	$65°19'20.436''$
39525	56572.192405	5	0.131	$1^{h}53^{m}37.021^{s}$	$64°00'40.454''$
44170	56661.020185	6	0.323	$2^{h}38^{m}15.302^{s}$	$62°30'30.846''$
46040	56549.197090	6	0.455	$5^{h}20^{m}55.263^{s}$	$61°56'37.813''$
50319	56657.933698	7	0.488	$2^{h}48^{m}40.755^{s}$	$60°37'24.222''$
66182	56771.971640	4	0.089	$9^{h}48^{m}27.692^{s}$	$56°15'19.683''$
93612	56847.196320	5	0.407	$20^{h}19^{m}10.000^{s}$	$49°42'08.605''$
95863	56696.181924	8	0.795	$10^{h}22^{m}11.507^{s}$	$49°07'04.363''$
108931	56620.872664	5	0.220	$21^{h}04^{m}38.112^{s}$	$46°22'30.292''$
108931	56620.872607	5	0.229	$21^{h}04^{m}38.112^{s}$	$46°22'30.292''$
113658	56845.081675	5	0.288	$21^{h}18^{m}54.454^{s}$	$45°23'21.131''$
125414	56622.883602	5	0.304	$21^{h}55^{m}26.400^{s}$	$43°00'31.082''$
126427	56621.928276	5	0.217	$22^{h}08^{m}50.677^{s}$	$42°48'33.467''$
127434	56622.888483	6	0.501	$22^{h}07^{m}51.429^{s}$	$42°36'35.305''$
141272	56772.945138	3	0.164	$11^{h}03^{m}02.812^{s}$	$39°50'18.384''$
147662	56507.902042	2	0.005	$16^{h}48^{m}59.063^{s}$	$38°40'55.875''$
151518	56774.885676	6	0.392	$11^{h}11^{m}29.062^{s}$	$37°55'17.943''$
160355	56864.190821	4	0.095	$2^{h}17^{m}48.750^{s}$	$36°14'18.104''$
163175	56873.092428	6	0.268	$20^{h}23^{m}26.250^{s}$	$35°52'09.292''$
163432	56868.202351	7	0.504	$2^{h}25^{m}32.813^{s}$	$35°41'07.205''$
191977	56519.128695	5	0.233	$23^{h}26^{m}15.000^{s}$	$30°51'54.923''$
196623	56699.276413	9	0.830	$12^{h}20^{m}23.438^{s}$	$30°00'00.000''$
197644	56697.235451	9	1.117	$12^{h}15^{m}28.125^{s}$	$29°49'40.292''$
197702	56770.985312	6	0.349	$13^{h}37^{m}01.875^{s}$	$29°49'40.292''$
201791	56771.022782	8	0.892	$13^{h}27^{m}11.250^{s}$	$29°08'32.005''$
228369	56693.177882	6	0.401	$12^{h}22^{m}30.000^{s}$	$24°47'18.819''$

Continued on next page

Cell	Mjd	Obs	Exp	RA	Dec
244841	56797.005617	5	0.169	$14^{h}26^{m}15.000^{s}$	$22°11'07.289''$
247524	56581.244455	9	0.657	$5^{h}19^{m}55.312^{s}$	$21°42'09.970''$
255725	56651.992010	6	0.370	$5^{h}32^{m}34.688^{s}$	$20°25'25.015''$
307871	56678.875759	8	0.781	$3^{h}42^{m}11.250^{s}$	$12°28'57.934''$
317307	56663.048796	6	0.320	$8^{h}52^{m}15.938^{s}$	$11°06'39.174''$
351963	56548.170919	4	0.140	$5^{h}07^{m}15.938^{s}$	$5°58'44.964''$
385320	56775.167137	6	0.233	$18^{h}55^{m}32.812^{s}$	$1°11'37.494''$
422174	56500.949463	4	0.095	$18^{h}41^{m}29.062^{s}$	$-4°10'53.502''$
437530	56861.938239	7	0.368	$18^{h}35^{m}09.375^{s}$	$-6°25'45.906''$
437536	56504.955016	5	0.216	$18^{h}43^{m}35.625^{s}$	$-6°25'45.906''$
438313	56773.983007	9	0.878	$12^{h}56^{m}57.188^{s}$	$-6°34'46.535''$
439340	56661.262430	4	0.098	$13^{h}00^{m}28.125^{s}$	$-6°43'47.326''$
439585	56504.963792	7	0.497	$18^{h}45^{m}00.000^{s}$	$-6°43'47.326''$
454797	56824.934069	4	0.163	$15^{h}17^{m}34.688^{s}$	$-8°59'21.478''$

Table C.4: Results from the $\Delta t = 2$s search. For more details, please refer to table C.1.

Cell	Mjd	Obs	Exp	RA	Dec
18744	56691.999482	4	0.059	$7^{h}23^{m}30.309^{s}$	$72°12'09.419''$
22435	56690.132035	3	0.020	$9^{h}52^{m}38.491^{s}$	$70°32'09.418''$
24157	56685.085462	3	0.041	$9^{h}37^{m}38.182^{s}$	$69°47'38.017''$
25530	56724.176410	1	0.012	$11^{h}32^{m}55.221^{s}$	$69°14'12.448''$
33794	56750.044624	1	0.013	$11^{h}42^{m}00.000^{s}$	$66°04'12.232''$
38966	56575.134489	5	0.105	$1^{h}57^{m}00.000^{s}$	$64°11'55.485''$
41885	56549.230135	3	0.051	$5^{h}09^{m}06.207^{s}$	$63°15'37.757''$
41885	56549.230146	3	0.071	$5^{h}09^{m}06.207^{s}$	$63°15'37.757''$
49681	56657.928133	4	0.059	$2^{h}36^{m}04.557^{s}$	$60°48'44.171''$
49688	56578.162942	4	0.061	$2^{h}52^{m}01.519^{s}$	$60°48'44.171''$
50845	56870.087157	3	0.040	$22^{h}39^{m}37.358^{s}$	$60°37'24.222''$
51486	56870.137525	3	0.041	$22^{h}42^{m}22.500^{s}$	$60°26'03.980''$
54079	56871.143959	5	0.125	$22^{h}28^{m}54.146^{s}$	$59°40'40.027''$
73659	56721.015841	1	0.005	$9^{h}49^{m}41.250^{s}$	$54°20'27.284''$
73660	56741.001081	3	0.025	$9^{h}51^{m}33.750^{s}$	$54°20'27.284''$
87646	56847.156576	4	0.100	$20^{h}08^{m}19.522^{s}$	$51°03'43.347''$

Continued on next page

Cell	Mjd	Obs	Exp	RA	Dec
87656	56847.152173	3	0.046	$20^{\mathrm{h}}25^{\mathrm{m}}33.014^{\mathrm{s}}$	$51°03'43.347''$
88810	56653.053913	4	0.091	$5^{\mathrm{h}}23^{\mathrm{m}}19.052^{\mathrm{s}}$	$50°40'26.977''$
89825	56696.163029	3	0.029	$10^{\mathrm{h}}12^{\mathrm{m}}10.189^{\mathrm{s}}$	$50°28'48.159''$
92393	56696.129827	4	0.082	$10^{\mathrm{h}}23^{\mathrm{m}}43.256^{\mathrm{s}}$	$49°53'49.142''$
94979	56695.034372	3	0.037	$10^{\mathrm{h}}05^{\mathrm{m}}13.761^{\mathrm{s}}$	$49°18'46.219''$
95855	56723.047432	4	0.070	$10^{\mathrm{h}}09^{\mathrm{m}}02.466^{\mathrm{s}}$	$49°07'04.363''$
127654	56601.135058	4	0.071	$3^{\mathrm{h}}21^{\mathrm{m}}20.632^{\mathrm{s}}$	$42°24'36.595''$
131502	56624.839217	5	0.159	$22^{\mathrm{h}}03^{\mathrm{m}}59.062^{\mathrm{s}}$	$41°48'37.134''$
137425	56803.985526	4	0.065	$16^{\mathrm{h}}53^{\mathrm{m}}12.188^{\mathrm{s}}$	$40°37'12.667''$
149461	56777.005810	4	0.048	$10^{\mathrm{h}}58^{\mathrm{m}}49.688^{\mathrm{s}}$	$38°18'03.321''$
153563	56693.118774	3	0.009	$11^{\mathrm{h}}07^{\mathrm{m}}15.938^{\mathrm{s}}$	$37°32'39.570''$
166375	56514.140782	3	0.019	$23^{\mathrm{h}}24^{\mathrm{m}}08.438^{\mathrm{s}}$	$35°19'07.582''$
166460	56573.929044	4	0.072	$1^{\mathrm{h}}22^{\mathrm{m}}58.125^{\mathrm{s}}$	$35°08'10.013''$
167402	56570.940489	4	0.065	$23^{\mathrm{h}}27^{\mathrm{m}}39.375^{\mathrm{s}}$	$35°08'10.013''$
167513	56594.930958	2	0.006	$2^{\mathrm{h}}04^{\mathrm{m}}27.188^{\mathrm{s}}$	$34°57'13.915''$
171665	56538.138636	4	0.047	$3^{\mathrm{h}}23^{\mathrm{m}}12.188^{\mathrm{s}}$	$34°13'43.919''$
173709	56538.231250	3	0.035	$3^{\mathrm{h}}17^{\mathrm{m}}34.688^{\mathrm{s}}$	$33°52'07.337''$
173709	56538.231262	3	0.035	$3^{\mathrm{h}}17^{\mathrm{m}}34.688^{\mathrm{s}}$	$33°52'07.337''$
176791	56539.176799	3	0.050	$3^{\mathrm{h}}30^{\mathrm{m}}56.250^{\mathrm{s}}$	$33°19'52.640''$
176791	56539.176811	3	0.050	$3^{\mathrm{h}}30^{\mathrm{m}}56.250^{\mathrm{s}}$	$33°19'52.640''$
177640	56571.938019	5	0.122	$23^{\mathrm{h}}24^{\mathrm{m}}50.625^{\mathrm{s}}$	$33°19'52.640''$
177640	56571.938030	5	0.100	$23^{\mathrm{h}}24^{\mathrm{m}}50.625^{\mathrm{s}}$	$33°19'52.640''$
193545	56697.241608	4	0.116	$12^{\mathrm{h}}11^{\mathrm{m}}15.000^{\mathrm{s}}$	$30°31'05.632''$
194023	56519.123949	2	0.007	$23^{\mathrm{h}}23^{\mathrm{m}}26.250^{\mathrm{s}}$	$30°31'05.632''$
197701	56770.976574	4	0.104	$13^{\mathrm{h}}35^{\mathrm{m}}37.500^{\mathrm{s}}$	$29°49'40.292''$
199743	56770.999823	4	0.090	$13^{\mathrm{h}}27^{\mathrm{m}}11.250^{\mathrm{s}}$	$29°29'04.061''$
241388	56631.046921	3	0.009	$5^{\mathrm{h}}31^{\mathrm{m}}10.313^{\mathrm{s}}$	$22°40'10.596''$
243731	56718.987151	4	0.067	$12^{\mathrm{h}}26^{\mathrm{m}}00.938^{\mathrm{s}}$	$22°20'47.716''$
244841	56797.005640	3	0.029	$14^{\mathrm{h}}26^{\mathrm{m}}15.000^{\mathrm{s}}$	$22°11'07.289''$
252522	56649.841057	3	0.023	$2^{\mathrm{h}}27^{\mathrm{m}}39.375^{\mathrm{s}}$	$20°54'07.250''$
253270	56543.014037	3	0.021	$19^{\mathrm{h}}59^{\mathrm{m}}31.875^{\mathrm{s}}$	$20°54'07.250''$
254293	56543.014037	4	0.022	$19^{\mathrm{h}}58^{\mathrm{m}}49.688^{\mathrm{s}}$	$20°44'32.568''$
259818	56651.005060	2	0.006	$5^{\mathrm{h}}28^{\mathrm{m}}21.563^{\mathrm{s}}$	$19°47'16.978''$
260114	56717.006203	3	0.036	$12^{\mathrm{h}}24^{\mathrm{m}}36.562^{\mathrm{s}}$	$19°47'16.978''$

Continued on next page

Cell	Mjd	Obs	Exp	RA	Dec
260837	56580.250164	3	0.051	$5^{\mathrm{h}}20^{\mathrm{m}}37.500^{\mathrm{s}}$	$19°37'46.405''$
266861	56657.835856	4	0.069	$2^{\mathrm{h}}31^{\mathrm{m}}52.500^{\mathrm{s}}$	$18°40'54.569''$
281040	56561.956215	4	0.057	$22^{\mathrm{h}}51^{\mathrm{m}}47.813^{\mathrm{s}}$	$16°38'45.744''$
283093	56591.878871	4	0.066	$22^{\mathrm{h}}58^{\mathrm{m}}49.688^{\mathrm{s}}$	$16°20'05.362''$
314394	56714.241519	2	0.009	$12^{\mathrm{h}}35^{\mathrm{m}}09.375^{\mathrm{s}}$	$11°34'02.703''$
320377	56662.082035	3	0.019	$8^{\mathrm{h}}48^{\mathrm{m}}45.000^{\mathrm{s}}$	$10°39'18.214''$
356059	56548.163461	2	0.012	$5^{\mathrm{h}}07^{\mathrm{m}}15.938^{\mathrm{s}}$	$5°22'45.764''$
357082	56548.169449	3	0.035	$5^{\mathrm{h}}05^{\mathrm{m}}09.375^{\mathrm{s}}$	$5°13'46.306''$
381227	56786.170356	5	0.120	$18^{\mathrm{h}}59^{\mathrm{m}}45.938^{\mathrm{s}}$	$1°47'26.825''$
395745	56543.949829	2	0.013	$23^{\mathrm{h}}15^{\mathrm{m}}42.188^{\mathrm{s}}$	$-0°17'54.301''$
408031	56543.956310	2	0.012	$23^{\mathrm{h}}12^{\mathrm{m}}53.438^{\mathrm{s}}$	$-2°05'21.738''$
431149	56771.925010	3	0.028	$13^{\mathrm{h}}01^{\mathrm{m}}52.500^{\mathrm{s}}$	$-5°31'45.356''$
434216	56658.233770	3	0.018	$12^{\mathrm{h}}55^{\mathrm{m}}32.812^{\mathrm{s}}$	$-5°58'44.964''$
437721	56595.928025	3	0.031	$23^{\mathrm{h}}03^{\mathrm{m}}45.000^{\mathrm{s}}$	$-6°25'45.906''$
439586	56513.941770	3	0.026	$18^{\mathrm{h}}46^{\mathrm{m}}24.375^{\mathrm{s}}$	$-6°43'47.326''$
439768	56595.928268	2	0.037	$23^{\mathrm{h}}02^{\mathrm{m}}20.625^{\mathrm{s}}$	$-6°43'47.326''$
440606	56508.957279	3	0.022	$18^{\mathrm{h}}41^{\mathrm{m}}29.062^{\mathrm{s}}$	$-6°52'48.285''$
448796	56858.995887	3	0.025	$18^{\mathrm{h}}38^{\mathrm{m}}40.313^{\mathrm{s}}$	$-8°05'02.450''$

Bibliography

Abdo, A. A. et al. (July 2014). "Milagro Limits and HAWC Sensitivity for the Rate-Density of Evaporating Primordial Black Holes". In: DOI: 10.1016/j.astropartphys.2014.10.007.

Ackermann, M. et al. (Apr. 2018). "Search for Gamma-Ray Emission from Local Primordial Black Holes with the Fermi Large Area Telescope". In: *The Astrophysical Journal* 857.1, p. 49. DOI: 10.3847/1538-4357/aaac7b.

Aharonian, F. et al. (Apr. 2023). "Search for the evaporation of primordial black holes with H.E.S.S". In: *Journal of Cosmology and Astroparticle Physics* 2023.04, p. 040. DOI: 10.1088/1475-7516/2023/04/040.

Ahnen, M. L. et al. (2017a). "Performance of the MAGIC telescopes under moonlight". In: *Astropart. Phys.* 94, pp. 29–41. DOI: 10.1016/j.astropartphys.2017.08.001.

Ahnen, M. L. et al. (Sept. 2017b). "Performance of the MAGIC telescopes under moonlight". In: *Astroparticle Physics* 94, pp. 29–41. DOI: 10.1016/j.astropartphys.2017.08.001.

Albert, A. et al. (Apr. 2020). "Constraining the local burst rate density of primordial black holes with HAWC". In: *Journal of Cosmology and Astroparticle Physics* 2020.4. DOI: 10.1088/1475-7516/2020/04/026.

Albert, J. et al. (2008a). "Implementation of the Random Forest Method for the Imaging Atmospheric Cherenkov Telescope MAGIC". In: *Nucl. Instrum. Meth. A* 588, pp. 424–432. DOI: 10.1016/j.nima.2007.11.068. arXiv: 0709.3719 [astro-ph].

Albert, J. et al. (Apr. 2008b). "Implementation of the Random Forest method for the Imaging Atmospheric Cherenkov Telescope MAGIC". In: *Nuclear Instruments and Methods in Physics Research Section A: Accelerators, Spectrometers, Detectors and Associated Equipment* 588.3, pp. 424–432. DOI: 10.1016/j.nima.2007.11.068.

Albert, J. et al. (Feb. 2008c). "VHE Gamma-Ray Observation of the Crab Nebula and its Pulsar with the MAGIC Telescope". In: *The Astrophysical Journal* 674.2, p. 1037. DOI: 10.1086/525270.

Aleksic, J. et al. (2012). "Performance of the MAGIC stereo system obtained with Crab Nebula data". In: *Astropart. Phys.* 35, pp. 435–448. DOI: 10.1016/j.astropartphys.2011.11.007.

Aleksić, J. et al. (2015a). "The major upgrade of the MAGIC telescopes, Part I: The hardware improvements and the commissioning of the system". In: *Astropart. Phys.* 72, pp. 61–75. DOI: 10.1016/j.astropartphys.2015.04.004. arXiv: 1409.6073 [astro-ph.IM].

— (2015b). "The major upgrade of the MAGIC telescopes, Part II: A performance study using observations of the Crab Nebula". In: *Astropart. Phys.* 72, pp. 76–94. DOI: 10.1016/j.astropartphys.2015.02.005.

Aleksić, Jelena (2013). "Optimized Dark Matter Searches in Deep Observations of Segue 1 with MAGIC". PhD thesis. Barcelona, Autonoma U. DOI: 10.1007/978-3-319-23123-5.

Alexandreas, D. E. et al. (Oct. 1993). "New limit on the rate-density of evaporating black holes". In: *Physical Review Letters* 71.16, pp. 2524–2527. DOI: 10.1103/PhysRevLett.71.2524.

Anderson, Carl D. (1932). "The Apparent Existence of Easily Deflectable Positives". In: *Science* 76.1967, pp. 238–239. DOI: 10.1126/science.76.1967.238.

Anderson, Carl D. and Seth H. Neddermeyer (Aug. 1936). "Cloud Chamber Observations of Cosmic Rays at 4300 Meters Elevation and Near Sea-Level". In: *Phys. Rev.* 50 (4), pp. 263–271. DOI: 10.1103/PhysRev.50.263.

Auger, P. et al. (July 1939). "Extensive Cosmic-Ray Showers". In: *Reviews of Modern Physics* 11.3-4, pp. 288–291. DOI: 10.1103/RevModPhys.11.288.

Ayala Solares, Hugo A. et al. (Jan. 2020). "The Astrophysical Multimessenger Observatory Network (AMON): Performance and science program". In: *Astroparticle Physics* 114, pp. 68–76. DOI: 10.1016/j.astropartphys.2019.06.007.

Bennett, C. L. et al. (Sept. 2013). "NINE-YEAR WILKINSON MICROWAVE ANISOTROPY PROBE (WMAP) OBSERVATIONS: FINAL MAPS AND RESULTS". In: *The Astrophysical Journal Supplement Series* 208.2, p. 20. DOI: 10.1088/0067-0049/208/2/20.

Bernlohr, K. (2000). "Impact of atmospheric parameters on the atmospheric Cherenkov technique". In: *Astropart. Phys.* 12, pp. 255–268. DOI: 10.1016/S0927-6505(99)00093-6. arXiv: astro-ph/9908093.

Bitossi, Massimiliano, Riccardo Paoletti, and Diego Tescaro (2016). "Ultra-Fast Sampling and Data Acquisition Using the DRS4 Waveform Digitizer". In: *IEEE Trans. Nucl. Sci.* 63.4, pp. 2309–2316. DOI: 10.1109/TNS.2016.2578963.

Bothe, W. and W. Kolhorster (1929). "Das Wesen der Hohenstrahlung". In: *Phys. Z.* 56, pp. 751–777.

Bovy, Jo and Scott Tremaine (Aug. 2012). "ON THE LOCAL DARK MATTER DENSITY". In: *The Astrophysical Journal* 756.1, p. 89. DOI: 10.1088/0004-637X/756/1/89.

Braibant, Sylvie and Giorgio Giacomelli (2012). *Particles and fundamental interactions: An introduction to particle physics*. Undergraduate lecture notes in physics. Springer. ISBN: 978-94-007-2463-1. DOI: 10.1007/978-94-007-2464-8.

Brun, R. and F. Rademakers (1997). "ROOT: An object oriented data analysis framework". In: *Nucl. Instrum. Meth. A* 389. Ed. by M. Werlen and D. Perret-Gallix, pp. 81–86. DOI: 10.1016/S0168-9002(97)00048-X.

Carr, B. J. et al. (May 2010). "New cosmological constraints on primordial black holes". In: *Physical Review D* 81.10, p. 104019. DOI: 10.1103/PhysRevD.81.104019.

Carr, Bernard and Florian Kuhnel (2020). "Primordial Black Holes as Dark Matter: Recent Developments". In: *Annual Review of Nuclear and Particle Science* 70, pp. 355–394. DOI: 10.1146/annurev-nucl-050520.

Carr, Bernard et al. (Dec. 2021). "Constraints on primordial black holes". In: *Reports on Progress in Physics* 84.11, p. 116902. DOI: 10.1088/1361-6633/ac1e31.

Carr, Bernard J. (2003). "Primordial black holes as a probe of cosmology and high energy physics". In: *Lect. Notes Phys.* 631, pp. 301–321. DOI: 10.1007/978-3-540-45230-0_7.

Cerenkov, P. A. (1937). "Visible radiation produced by electrons moving in a medium with velocities exceeding that of light". In: *Phys. Rev.* 52, pp. 378–379. DOI: 10.1103/PhysRev.52.378.

Chapline, George F. (Jan. 1975). "Cosmological effects of primordial black holes". In: *Nature* 253.5489, pp. 251–252. DOI: 10.1038/253251a0.

Da Vela, P. et al. (2018). "Study of the IACT angular acceptance and Point Spread Function". In: *Astropart. Phys.* 98, pp. 1–8. DOI: 10.1016/j.astropartphys.2018.01.002.

Dazzi, F. et al. (Aug. 2015). "Performance studies of the new stereoscopic Sum-Trigger-II of MAGIC after one year of operation". In: DOI: 10.48550/arXiv.1508.05255.

Dirac, Paul Adrien Maurice (1928). "The quantum theory of the electron". In: *Proceedings of the Royal Society of London. Series A, Containing Papers of a Mathematical and Physical Character* 117.778, pp. 610–624. DOI: 10.1098/rspa.1928.0023.

Engel, Ralph, Dieter Heck, and Tanguy Pierog (2011). "Extensive air showers and hadronic interactions at high energy". In: *Ann. Rev. Nucl. Part. Sci.* 61, pp. 467–489. DOI: 10.1146/annurev.nucl.012809.104544.

Feldman, Gary J. and Robert D. Cousins (Apr. 1998). "Unified approach to the classical statistical analysis of small signals". In: *Physical Review D* 57.7, pp. 3873–3889. DOI: 10.1103/PhysRevD.57.3873.

Fernandez Barral, Alba (2018). "Extreme Particle Acceleration in Microquasar Jets and Pulsar Wind Nebulae with the MAGIC Telescopes". DOI: 10.1007/978-3-319-97538-2.

Fomin, V. P. et al. (1994). "New methods of atmospheric Cherenkov imaging for gamma-ray astronomy. 1: The False source method". In: *Astropart. Phys.* 2, pp. 137–150. DOI: 10.1016/0927-6505(94)90036-1.

Frank, I. M. and I. E. Tamm (1937). "Coherent visible radiation of fast electrons passing through matter". In: *Compt. Rend. Acad. Sci. URSS* 14.3, pp. 109–114. DOI: 10.3367/UFNr.0093.196710o.0388.

Gaisser, Thomas K., Ralph Engel, and Elisa Resconi (June 2016). *Cosmic Rays and Particle Physics*. DOI: 10.1017/CBO9781139192194.

Gaisser, Thomas K., Ralph Engel, and Elisa Resconi (2016). *Cosmic Rays and Particle Physics*.

Gini, Corrado (1921). "Measurement of Inequality of Incomes". In: *The Economic Journal* 31.121, pp. 124–126. ISSN: 00130133, 14680297.

Górski, K. M. et al. (Apr. 2005). "HEALPix: A Framework for High-Resolution Discretization and Fast Analysis of Data Distributed on the Sphere". In: *Astrophys. J.* 622.2, pp. 759–771. DOI: 10.1086/427976. eprint: astro-ph/0409513.

Grieder, Peter K. F. (2010). *Extensive Air Showers and High Energy Phenomena*. Berlin, Heidelberg: Springer. DOI: 10.1007/978-3-540-76941-5.

Górski, K. M. et al. (Apr. 2005). "HEALPix: A Framework for High-Resolution Discretization and Fast Analysis of Data Distributed on the Sphere". en. In: *The Astrophysical Journal* 622.2, p. 759. DOI: 10.1086/427976.

Halzen, F. et al. (Oct. 1991). "Gamma rays and energetic particles from primordial black holes". In: *Nature* 353.6347, pp. 807–815. DOI: 10.1038/353807a0.

Hawking, S. W. (Mar. 1974). "Black hole explosions?" In: *Nature* 248.5443, pp. 30–31. DOI: 10.1038/248030a0.

— (1975). "Particle Creation by Black Holes". In: *Commun. Math. Phys.* 43. Ed. by G. W. Gibbons and S. W. Hawking, pp. 199–220. DOI: 10.1007/BF02345020.

Hawking, Stephen (1971). "GRAVITATIONALLY COLLAPSED OBJECTS OF VERY LOW MASS". In: *Monthly Notices of the Royal Astronomical Society* 152.1, pp. 75–78.

Heckler, Andrew F. (Jan. 1997). "Formation of a Hawking-radiation photosphere around microscopic black holes". In: *Physical Review D* 55.2, pp. 480–488. DOI: 10.1103/PhysRevD.55.480.

Heitler, W. (1936). *The quantum theory of radiation*. Vol. 5. International Series of Monographs on Physics. Oxford University Press.

Hess, Victor F. (1912). "Über Beobachtungen der durchdringenden Strahlung bei sieben Freiballonfahrten". In: *Phys. Z.* 13, pp. 1084–1091.

Hillas, A. M. (Aug. 1985). "Cerenkov Light Images of EAS Produced by Primary Gamma Rays and by Nuclei". In: *19th International Cosmic Ray Conference (ICRC19), Volume 3*. Vol. 3. International Cosmic Ray Conference, p. 445.

Hinshaw, G. et al. (Sept. 2013). "NINE-YEAR WILKINSON MICROWAVE ANISOTROPY PROBE (WMAP) OBSERVATIONS: COSMOLOGICAL PARAMETER RESULTS". In: *The Astrophysical Journal Supplement Series* 208.2, p. 19. DOI: 10.1088/0067-0049/208/2/19.

Hofmann, W. et al. (1999). "Comparison of techniques to reconstruct VHE gamma-ray showers from multiple stereoscopic Cherenkov images". In: *Astroparticle Physics* 12.3, pp. 135–143. ISSN: 0927-6505. DOI: 10.1016/S0927-6505(99)00084-5.

Hubbell, J. H., H. A. Gimm, and I. O/verbo/ (1980). "Pair, Triplet, and Total Atomic Cross Sections (and Mass Attenuation Coefficients) for 1 MeV-100 GeV Photons in Elements Z=1 to 100". In: *Journal of Physical and Chemical Reference Data* 9.4, pp. 1023–1148. DOI: 10.1063/1.555629.

Ishio, Kazuma (2020). "Improvement in the γ-ray energy reconstruction of MAGIC and impact on the spectral analysis of the first Gamma Ray Burst detected at TeV energies". PhD thesis. Munich U. DOI: 10.5282/edoc.27600.

Klebesadel, Ray W., Ian B. Strong, and Roy A. Olson (June 1973). "Observations of Gamma-Ray Bursts of Cosmic Origin". In: *The Astrophysical Journal* 182, p. L85. DOI: 10.1086/181225.

Leo, William R (1994). *Techniques for nuclear and particle physics experiments: a how-to approach; 2nd ed.* Berlin: Springer. DOI: 10.1007/978-3-642-57920-2.

Lessard, R. W. et al. (2001). "A New analysis method for reconstructing the arrival direction of TeV gamma-rays using a single imaging atmospheric Cherenkov telescope". In: *Astropart. Phys.* 15, pp. 1–18. DOI: 10.1016/S0927-6505(00)00133-X. arXiv: astro-ph/0005468.

Letessier-Selvon, Antoine and Todor Stanev (2011). "Ultrahigh Energy Cosmic Rays". In: *Rev. Mod. Phys.* 83, pp. 907–942. DOI: 10.1103/RevModPhys.83.907. arXiv: 1103.0031 [astro-ph.HE].

Li, T. P. and Y. Q. Ma (1983). "Analysis methods for results in gamma-ray astronomy". In: *Astrophys. J.* 272, pp. 317–324. DOI: 10.1086/161295.

Linton, E. T. et al. (Jan. 2006). "A new search for primordial black hole evaporations using the Whipple gamma-ray telescope". In: *Journal of Cosmology and Astroparticle Physics* 2006.01, p. 013. DOI: 10.1088/1475-7516/2006/01/013.

López-Coto, Rubén (2015). "Very-high-energy γ-ray observations of pulsar wind nebulae and cataclysmic variable stars with MAGIC and development of trigger systems for IACTs". PhD thesis. Barcelona, Autonoma U. DOI: 10.1007/978-3-319-44751-3.

López-Coto, R. et al. (Apr. 2016). "The Topo-trigger: a new concept of stereo trigger system for imaging atmospheric Cherenkov telescopes". In: *Journal of Instrumentation* 11.04, P04005. DOI: 10.1088/1748-0221/11/04/P04005.

MacGibbon, Jane H. (July 1991). "Quark- and gluon-jet emission from primordial black holes. II. The emission over the black-hole lifetime". In: *Physical Review D* 44.2, pp. 376–392. DOI: 10.1103/PhysRevD.44.376.

MacGibbon, Jane H., B. J. Carr, and Don N. Page (Sept. 2008). "Do evaporating black holes form photospheres?" In: *Physical Review D* 78.6, p. 064043. DOI: 10.1103/PhysRevD.78.064043.

MacGibbon, Jane H. and B. R. Webber (May 1990). "Quark- and gluon-jet emission from primordial black holes: The instantaneous spectra". In: *Physical Review D* 41.10, pp. 3052–3079. DOI: 10.1103/PhysRevD.41.3052.

MAGIC Collaboration (Nov. 2019). "Teraelectronvolt emission from the γ-ray burst GRB 190114C". In: *Nature* 575.7783, pp. 455–458. DOI: 10.1038/s41586-019-1750-x.

Majumdar, P. et al. (Aug. 2005). "Monte Carlo simulation for the MAGIC telescope". In: *29th International Cosmic Ray Conference*.

Matthews, J. (Jan. 2005). "A Heitler model of extensive air showers". In: *Astroparticle Physics* 22, pp. 387–397. DOI: 10.1016/j.astropartphys.2004.09.003.

Mirzoyan, R. (Aug. 1997). "On the Calibration Accuracy of Light Sensors in Atmospheric Cherenkov Fluorescence and Neutrino Experiments". In: *25th International Cosmic Ray Conference*. Vol. 1-8. Conference Name: International Cosmic Ray Conference ADS Bibcode: 1997ICRC....7..265M, p. 265.

Mirzoyan, Razmik (Jan. 2019). "First time detection of a GRB at sub-TeV energies; MAGIC detects the GRB 190114C". In: *The Astronomer's Telegram* 12390. ADS Bibcode: 2019ATel12390....1M, p. 1.

Naurois, Mathieu de and Daniel Mazin (2015). "Ground-based detectors in very-high-energy gamma-ray astronomy". In: *Comptes Rendus Physique* 16, pp. 610–627. DOI: 10.1016/j.crhy.2015.08.011. arXiv: 1511.00463 [astro-ph.IM].

Nigro, Cosimo (Oct. 2019). "Study of Persistent and Flaring Gamma-Ray Emission from Active Galactic Nuclei with the MAGIC Telescopes and Prospects for Future Open Data Formats in Gamma-Ray Astronomy". PhD thesis. Humboldt-Universität zu Berlin. DOI: 10.18452/20582.

Oser, S. et al. (Feb. 2001). "High-Energy Gamma-Ray Observations of the Crab Nebula and Pulsar with the Solar Tower Atmospheric Cerenkov Effect Experiment". In: *The Astrophysical Journal* 547.2, p. 949. DOI: 10.1086/318415.

Page, Don N. (Jan. 1976). "Particle emission rates from a black hole: Massless particles from an uncharged, nonrotating hole". In: *Physical Review D* 13.2, pp. 198–206. DOI: 10.1103/PhysRevD.13.198.

Petkov, V. B. et al. (2008). "Searching for Very-High-Energy Gamma-Ray Bursts from Evaporating Primordial Black Holes". In: DOI: 10.48550/ARXIV.0808.3093.

Prandini, Elisa et al. (2016). "Study of hadron and gamma-ray acceptance of the MAGIC telescopes: towards an improved background estimation". In: *Proceedings of The 34th International Cosmic Ray Conference — PoS(ICRC2015)*. Vol. 236, p. 721. DOI: 10.22323/1.236.0721.

Rossi, Bruno (Feb. 1934). "Directional Measurements on the Cosmic Rays Near the Geomagnetic Equator". In: *Physical Review* 45.3, pp. 212–214. DOI: 10.1103/PhysRev.45.212.

Rossi, Bruno and Kenneth Greisen (Oct. 1941). "Cosmic-Ray Theory". In: *Reviews of Modern Physics* 13.4, pp. 240–309. DOI: 10.1103/RevModPhys.13.240.

Rowell, G. P. (Oct. 2003). "A new template background estimate for source searching in TeV gamma-ray astronomy". In: *Astronomy & Astrophysics* 410.1, pp. 389–396. DOI: 10.1051/0004-6361:20031194.

Rutherford, Ernest (1913). *Radioactive substances and their radiations*. Cambridge, Univ. Press.

Sitarek, Julian et al. (2013). "Analysis techniques and performance of the Domino Ring Sampler version 4 based readout for the MAGIC telescopes". In: *Nucl. Instrum. Meth. A* 723, pp. 109–120. DOI: 10.1016/j.nima.2013.05.014. arXiv: 1305.1007 [astro-ph.IM].

Strzys, Marcel Constantin (2020). "Deciphering the gamma-ray sky". PhD Thesis. Munich U. DOI: 10.5282/edoc.26997.

TevCat Online Catalog. http://tevcat2.uchicago.edu/.

Tešić, G. and the VERITAS Collaboration (July 2012). "Searching for primordial black holes with the VERITAS gamma-ray experiment". In: *Journal of Physics: Conference Series* 375.5, p. 052024. ISSN: 1742-6596. DOI: 10.1088/1742-6596/375/1/052024.

Thoudam, S. et al. (Nov. 2016). "Cosmic-ray energy spectrum and composition up to the ankle: the case for a second Galactic component". In: *Astronomy & Astrophysics* 595. Publisher: EDP Sciences, A33. DOI: 10.1051/0004-6361/201628894.

Ukwatta, T. N. et al. (July 2016). "Primordial Black Holes: Observational characteristics of the final evaporation". In: *Astroparticle Physics* 80, pp. 90–114. DOI: 10.1016/j.astropartphys.2016.03.007.

Wagner, Robert Marcus (2006). "Measurement of Very High Energy Gamma-Ray Emission from Four Blazars Using the MAGIC Telescope and a Comparative Blazar Study". PhD thesis. Munich, Tech. U.

Wakely, S. P. and D. Horan (Jan. 2008). "TeVCat: An online catalog for Very High Energy Gamma-Ray Astronomy". In: *International Cosmic Ray Conference*. Vol. 3. International Cosmic Ray Conference, pp. 1341–1344.

Wenger, M. et al. (Apr. 2000). "The SIMBAD astronomical database - The CDS reference database for astronomical objects". In: *Astronomy and Astrophysics Supplement Series* 143.1, pp. 9–22. DOI: 10.1051/aas:2000332.

Workman, R. L. and others (2022a). "Review of Particle Physics". In: *PTEP* 2022, p. 083C01. DOI: 10.1093/ptep/ptac097.

Workman, R. L. et al. (2022b). "Review of Particle Physics". In: *PTEP* 2022, p. 083C01. DOI: 10.1093/ptep/ptac097.

Zanin, Roberta (2013). "MARS, the MAGIC analysis and reconstruction software". In: *33rd International Cosmic Ray Conference*, p. 0773.

Zel'dovich, Ya. B. and I. D. Novikov (1966). "The Hypothesis of Cores Retarded during Expansion and the Hot Cosmological Model". In: *Astronomicheskii Zhurnal* 43.4, pp. 758–760.

Zonca, Andrea et al. (Mar. 2019). "healpy: equal area pixelization and spherical harmonics transforms for data on the sphere in Python". In: *Journal of Open Source Software* 4.35, p. 1298. DOI: 10.21105/joss.01298.

Šidák, Zbyněk (June 1967). "Rectangular Confidence Regions for the Means of Multivariate Normal Distributions". In: *Journal of the American Statistical Association* 62.318, pp. 626–633. DOI: 10.1080/01621459.1967.10482935.

Agradecimientos

Hace mucho que comenzó este viaje que por fin termina. No era la ruta más sencilla, parecía continuar infinitamente en la distancia…pero aquí está. La meta, la tesis. El doctorado es una experiencia formativa brutal en la que aprendes y evolucionas, no solo como científica, sino como individuo. Si me encontrase con la yo que acababa de empezar el doctorado, no creo que me reconociese en ella. Como el gato que bufa a su reflejo en el espejo sin reconocer que se trata de sí mismo. Lo que sí puedo reconocer es que esta tesis y todos los cambios y aprendizajes que he conseguido durante su desarrollo han sido gracias al apoyo de mucha gente (y animales). A vosotros os doy las gracias.

En primer lugar doy las gracias a mi familia, que me ha apoyado sin descanso y sin dudas durante todos estos años. A mi padre y a mi madre, por mantenerme en los momentos más difíciles y tener fe en mi. A mis hermanas, que me habéis escuchado y animado en incontables ocasiones, aunque no supieseis muy bien de qué estaba hablando. Todos los viajes y fiestas me han ayudado a desconectar y resetear. A Manolo, por su inmensa generosidad que ha permitido que acabe el doctorado. Ya van dos tesis escritas en esta casa. A Maria José, por su optimismo y palabras de aliento.

A Xabi. Gracias por aguantarme cuando yo no aguantaba. Gracias por esas carreras con lluvia, viento o tormenta, aunque yo me enfadase si mencionabas la palabra "maratón". Verdaderamente estaba corriendo una maratón, aunque intentase rematarlo todo con el último último último sprint. Gracias por las discusiones de física y por ser mi patito de goma de software development. Ya ni recuerdo cuántos breakthroughs he tenido gracias a esas conversaciones. Gracias por las noches de pizza.

A mi director Javier Rico, por todo el esfuerzo y tiempo que me ha dedicado durante estos años y por introducirme al campo de los agujeros negros primordiales, que me resulta tan fascinante. A Juan Cortina, mi co-director durante los primeros años del doctorado, por abrirme la puerta al mundo de la astronomía de rayos gamma y de la instrumentación con multitud de ideas nuevas. Al resto de seniors de IFAE, Manel,

Abelardo y Óscar por compartir su sabiduría conmigo al sumergirme en los entresijos de MAGIC y MARS para desarrollar este software de búsqueda y por sus comentarios y recomendaciones durante las reuniones del grupo, que han ayudado a mejorar esta tesis. Thank you Daniel, for guiding me through the final, and toughest part, of the PhD and making me believe in my project. Your help was invaluable.

A la gente de IFAE, por alegrarme los días a la hora de comer y por compartir logros e infortunios conmigo. I've had so much fun with you, 10/10 would recommend as colleagues and friends.

A mis amigos de Barcelona, Santiago y Vigo. Laura, gracias por acogerme y estar siempre dispuesta a escuchar o responder mis preguntas. Berta, gracias por ser tan buena amiga (y acogerme también), ojalá estuviese ahí y saliésemos a patinar :P. Sara, gracias por seguir intentando, año tras año, que nos juntemos los amigos y por ser tan buena anfitriona que no haya excusas. Lucía, gracias por darlo todo siempre y de forma tan intensa, me motiva a intentar sacar más de la vida. También, sin tu empujón a descubrir más de mi no habría podido escribir esta tesis. Olga, gracias por ser una persona radiante, que te alegra el día con unos minutos de conversación. Gracias también por acompañarme en los momentos duros y por ayudarme a ser más egoísta, lo necesitaba y aún lo necesito. Pepe, gracias por aportar la combinación exacta de realidad y diversión, cosas que a mi me suelen faltar.

A special mention goes to Chiara Righi, for a great MAGIC shift and even greater photographs. The cover of this thesis is one of them. Otra mención especial va para Ami. Aunque ella no lo pueda leer, yo lo quiero escribir. Su llegada a mi vida marcó un antes y un después. Nuestros paseos y pequeños momentos han sido una fuente de fuerza y determinación que necesitaba cuando no me quedaba nada. De no ser por ella y por todos vosotros, esta tesis no existiría.

I thank the MAGIC collaboration for allowing me to use its proprietary observational data. The results presented in this thesis have not undergone the internal review procedure of MAGIC publications.